RAMAN-SCATTERING STUDIES OF THE STRUCTURE OF ION-IMPLANTED GaAs

by

Mark W. Holtz

Dissertation submitted to the faculty of the
Virginia Polytechnic Institute and State University
in partial fulfillment of the requirements
for the degree of

DOCTOR OF PHILOSOPHY

in

Physics

APPROVED:

Richard Zallen, Chairman

S.P. Almeida

J.G. Dillard

G.J.M. Indebetouw

C.D. Williams

August, 1987

Blacksburg, Virginia

RAMAN-SCATTERING STUDIES OF THE STRUCTURE OF ION-IMPLANTED GaAs

by Mark W. Holtz

Committee Chairman: Richard Zallen
Department of Physics

(ABSTRACT)

Extensive Raman-scattering studies have been performed in order to study the structure of ion-implanted GaAs, prior to any anneal. The spectroscopic evidence is consistent with a fine-scale mixture of amorphous and microcrystalline GaAs. Excessive bombardment with 120-keV SiF_3^+ ions results in a 500-A thick surface layer which is completely amorphous (a-GaAs).

A detailed chemical-etch damage depth profile has been completed for 45-keV Be^+-implanted GaAs, which is not completely amorphized. The damage is characterized using the microcrystalline longitudinal-optical (LO) phonon frequency, line width, and intensity, and the intensity of the a-GaAs component of the Raman spectrum. The damage layer possesses a 1500-A thick surface layer of constant, high damage. This high-damage plateau is followed by a transition region in which the damage level smoothly decreases until the undisturbed crystal is reached near 4000 A. LO intensities were analyzed, within the amorphous/crystalline mixed-phase model, to obtain the volume fractions of the two components. Consistent estimates of

the optical absorption in the high-damage plateau were obtained via two independent means.

Resonance-Raman experiments were carried out, using laser lines between 1.5 and 2.71 eV. The intensity of the a-GaAs spectral component was found to depend on scattering volume (optical penetration), thus providing an internal intensity standard allowing the effects of scattering volume and scattering efficiencies to be separated. The LO phonon was found to resonate approaching the E_1 electronic transition at 2.9 eV. The strength of the resonance decreases with smaller crystallite size.

A new Raman band was observed near 47 cm^{-1} for photon energies below 2 eV. It resonates at 1.7 eV, near E_0 and not near E_1. I propose that this new feature arises from GaAs acoustic modes made Raman active by defect-assisted scattering involving the crystalline/amorphous interface regions. A quantitative analysis is developed, with some success.

Intensities of silicon local are observed to remain constant upon annealing, although conductivity increases by several orders of magnitude. The anneal primarily restores the mobility to that of crystalline GaAs.

Acknowledgments

It has been my pleasure and good fortune to have worked with many fine people during my stay at Virginia Tech. I would like to thank my advisor, Dick Zallen, for guiding this project. His kindness, consideration, and continued support have made this research possible. I am also happy to have enjoyed a fruitful collaboration with Oren Brafman, whose enthusiasm and good humor made this experiment even more exciting.

I am also indebted to A.Geissberger and R.Sadler of ITT, and to S.Matteson of TI, each for sharing his knowledge in GaAs implantation research, and for their expertise in preparing the implanted GaAs. I would also like to thank W.Paul of Harvard University for providing the sputtered amorphous GaAs films, M-L.Theye of the Université Pierre et Marie Curie (Paris) for providing the evaporated film, and A.Pinczuk of AT&T Bell Labs for providing the AlGaAs alloy and the CaF_2 crystal.

I would also like to acknowledge the willing help of the Virginia Tech Physics Department Machine and Electronics Shops. I am especially grateful to Bob Ross and Roger Link for providing their excellent services.

I thank D.N.Bose, Eric Cole, Steve Conder, June Epp, and Jeff Feng for many helpful and interesting discussions. I would also like to thank Jeff Feng for

sharing many reflectance results and for his expert help in aquiring the reflectance spectra in Chapter 6. I am very fortunate to have had associations with fellow students John Dennison, Gao Chao, Terry Harter, and Kuryan Thomas during my graduate career at Virginia Tech. I am also appreciative of Scott Allen, Dave Foos, Rosemary Foos, Chris Pirie, Hein Tran, Todd Turner, and Bob Zellmann for their personal support, and Peter Gabriel for perspective.

I would like to thank my parents, Vernon and Stella Holtz, and all my family for all their encouragement and patience. To my wife's family for their patient understanding and hospitality.

Finally, I want to thank my loving wife Susan, without whom none of this would have happened. It is to her that I dedicate this work.

For Susan

Table of Contents

Chapter 1: INTRODUCTION 1

Chapter 2: EXPERIMENTAL ASPECTS 31

Chapter 3: RAMAN-SCATTERING CHARACTERIZATION OF IMPLANTATION-INDUCED DAMAGE IN GaAs 55

Chapter 4: RAMAN-SCATTERING DEPTH PROFILE OF THE STRUCTURE OF Be^+-IMPLANTED GaAs 79

Chapter 5: RAMAN SCATTERING USED FOR NON-DESTRUCTIVE DEPTH PROFILING 109

Chapter 6: PHOTON-ENERGY DEPENDENCE OF THE SCATTERING INTENSITIES OF a-GaAs, THE LO PHONON, AND A NEW FEATURE OBSERVED IN THE CRYSTALLINE/ AMORPHOUS MIXED PHASE 128

Chapter 7: SILICON LOCAL MODES IN GaAs: THE ROLE OF AMORPHICITY 175

Chapter 8: SUMMARY 194

Chapter 9: SUGGESTIONS FOR FUTURE RESEARCH 202

Literature Cited 207

Vita 214

CHAPTER 1: INTRODUCTION

1.1 INTRODUCTORY REMARKS

Gallium arsenide is a semiconductor which is recently undergoing intense scientific study. Because GaAs has a direct bandgap, making it an efficient light emitter, and because of its high carrier mobility, GaAs is a scientifically interesting semiconductor.

A controlled means by which GaAs single crystals can be doped is ion implantation [Duncan & Westphal]. Energetic ions of the dopant species are directed into the host substrate lattice. The doping process is completed by annealing, which aids in bringing high concentrations of the impurities to substitutional lattice sites, and which crystallizes the "damage layer" [Gibbons (1968)].

The ion-bombardment induced damage in the host lattice is a result of nuclear collisions between the impinging ions and the substrate atoms [Gibbons (1972), Carter & Grant]. The ions lose energy in these collisions, eventually bringing them to rest in the near-surface region. When the energy transfer is sufficient to break the host molecular bonds, damage results.

The ion energy is therefore a function of depth into the substrate. The nuclear scattering cross-section is also a function of energy [Schiff, p.105]. Therefore,

the ion damage (before any anneal) will have a depth distribution.

In this dissertation I shall describe an in-depth investigation into the structural characteristics of GaAs which has been implanted with various dopant-ion species. Particular emphasis is given to the depth distribution of the ion damage. The study is carried out using chemical-etch removal of surface layers and non-destructively using the photon-energy dependence of the optical absorption coefficient.

The use of ion implantation as a novel means by which amorphous semiconductor layers can be produced [Zallen, p.273] is a uniquely interesting (and convenient) process. Before "complete" amorphization of a single crystal occurs, the starting crystal passes through various intermediate phases. Consequences of ion damage to crystalline GaAs (c-GaAs) have previously been studied in detail [e.g. Tiong et al., Aspnes et al.]. The crystalline structure is broken up into a distribution of fine micro-crystallites at high ion fluence. In addition, these micro-crystals are mixed together with GaAs in the amorphous phase (a-GaAs). The mixed amorphous/microcrystalline model is supported on the basis of spectroscopic evidence [Aspnes et al., Theeten & Erman, Abels et al.]. With higher ion doses, the c-GaAs host may eventually be

rendered amorphous. These two subjects (mixed amorphous/microcrystalline phases and amorphization) shall be central themes in this dissertation.

GaAs is opaque to visible light. 5145-A (2.41-eV) green light has an optical penetration depth (d_{OPT} = $1/2\alpha$ here, where α is the absroption coefficient) of 550 A in c-GaAs [Aspnes & Studna] and 140 A in a-GaAs [Theeten & Erman]. This makes Raman scattering, using visible light as excitation, an excellent means by which to study the shallow damage layers produced by ion implantation.

1.2 c-GaAs PROPERTIES

GaAs is a direct-bandgap semiconductor which crystallizes in the cubic zincblende structure. The zincblende lattice (Fig. 1.1) consists of two inter-penetrating face-centered cubic (FCC) sublattices, each consisting solely of one type of constituent (Ga or As) [Kittel, p.26]. These sublattices are connected by Ga-As (primarily covalent) bonds: each Ga atom is tetrahedrally bonded to four As atoms, and vice versa.

The lattice is thereby described by a FCC with one atom of each type in the unit cell. The basic cube of either sublattice is chosen to define the <100> set of coordinate axes: (100), (010), and (001). The conventional cell is a cube with edges (a_o,0,0), (0,a_o,0), and (0,0,a_o),

see Table 1.1. Each conventional cell contains four GaAs molecules. A given atom is therefore bonded to four of its countertypes at $(111)a_0/4$, $(\bar{1}\bar{1}1)a_0/4$, $(1\bar{1}\bar{1})a_0/4$, and $(\bar{1}1\bar{1})a_0/4$.

For convenience, a symmetric basis is chosen: $\mathbf{a}_1 = (011)a_0/2$, $\mathbf{a}_2 = (101)a_0/2$, and $\mathbf{a}_3 = (110)a_0/2$. The reciprocal lattice of the FCC structure is the body-centered cubic (BCC) lattice with basis $\mathbf{b}_1 = (\bar{1}11)2\pi/a_0$, $\mathbf{b}_2 = (1\bar{1}1)2\pi/a_0$, and $\mathbf{b}_3 = (11\bar{1})2\pi/a_0$. The Brillouin zone is shown in Fig. 1.2 with important symmetry directions indicated. Within the Brillouin zone $\mathbf{k}$ wavevectors may span $|\mathbf{k}| \leq 2\pi/a_0$ in the <100> directions, $|\mathbf{k}| \leq 2\sqrt{2}\pi/a_0$ in <110>, $|\mathbf{k}| \leq \sqrt{3}\pi/a_0$ in the <111> symmetry directions.

1.3 RAMAN SCATTERING

The fundamentals of Raman scattering in crystalline semiconductors have been reviewed by several authors [Hayes & Loudon, Pinczuk & Burstein, Cardona, Pollak]. The first-order Raman-scattering processes are shown schematically in Fig. 1.3. Here, "first order" refers to the fact that only one phonon is created of annihilated. The entire first-order Stokes processes, illustrated in Fig. 1.3(c), involves <u>three</u> interaction vertices: two electron-photon interactions in which an electron-hole pair is created of

destroyed, and one electron-phonon (or hole-phonon) interaction in which an electron (or hole) inelastically scatters with the lattice to create a phonon. Following the development of Hayes & Loudon, the macroscopic properties of light scattering begin by considering the polarization field induced within the scattering medium by a periodically varying incident radiation field E,

$$P = \epsilon_0 \chi \cdot E \tag{1.1}$$

where the second-rank tensor χ represents the linear susceptibility of the medium and ϵ_0 is the static dielectric constant of the medium. The excitation modulates state functions (in the same frequency regime) of the medium, manifested here as changes in χ through small displacements $\mathbf{x}$. For small-amplitude normal-mode vibrations

$$P = \epsilon_0 (\chi_0 + \chi'_0 \cdot \mathbf{x}) \cdot E = P_0 + P' \tag{1.2}$$

where χ' are susceptibility derivatives with respect to the normal mode coordinates; the zero subscript denotes that the derivative is evaluated at the vibrational equilibrium position. The first term in Eq.(1.2) represents Rayleigh scattering, which is elastic (no change in photon energy). The second term (P') gives rise to Raman scattering, which

is inelastic (the scattered photon is shifted in energy from the incident photon).

The vibrational displacements possess temporal variations

$$e^{i\omega t} \quad , \quad e^{-i\omega t}$$

where ω is the phonon frequency. The second term in Eq.(1.2) will thereby result in an electric-field polarization with shifted frequency $\omega_2 = \omega_1 \mp \omega$. The - (+) sign is for Stokes (anti-Stokes) scattering in which the scattered light is shifted down (up) in energy from the incident photon frequency via creation (annihilation) of a phonon vibration. Consider here the Stokes component.

Defining the Raman tensor of a particular vibration (that part of the volume which contributes to the scattering at that frequency per unit length) as

$$\mathbf{R} = \chi'_0 \cdot \frac{\mathbf{x}}{|\mathbf{x}|} \tag{1.3}$$

we have the scattered light intensity

$$I_2 \sim I_1 \, |\mathbf{e}_2 \cdot \mathbf{P}'|^2 \sim I_1 \, |\mathbf{e}_2 \cdot \mathbf{R} \cdot \mathbf{e}_1|^2 \, \langle \mathbf{x}^* \cdot \mathbf{x} \rangle \tag{1.4}$$

where I_1 is the incident light intensity. $\mathbf{e}_1$ denotes the light polarization vector, and $\langle \mathbf{x}^* \cdot \mathbf{x} \rangle$ represents the

thermal average of the normal-mode displacements. For (thermal equilibrium) Stokes scattering $\langle \mathbf{x}^* \cdot \mathbf{x} \rangle \sim \{n(\omega,T) + 1\}/\omega$ and for anti-Stokes it is $\sim n(\omega,T)/\omega$, where n is the Fermi function at frequency ω and temperature T. Because the medium radiates energy at a different rate than it absorbs it, a factor of $n_2\omega_2/n_1\omega_1$ (n_i are the frequency-dependent refractive indices) also enters [Hayes & Loudon] resulting in an overall spectral differential cross-section

$$\frac{d^2\sigma}{d\Omega\, d\omega_2} \sim V\, \omega_1^3\, \omega_2\, \frac{n_2}{n_1}\, |\mathbf{e}_2 \cdot \mathbf{R}(\xi) \cdot \mathbf{e}_1|^2\, \langle \mathbf{x}^* \cdot \mathbf{x} \rangle \qquad (1.5)$$

where the phonon polarization direction ξ has been included, pertinent for lattices with non-centrosymmetric unit cells (like GaAs). By studying the scattering using various polarizations relative to the crystalline axes, the nature of the Raman tensor may be deduced via the term $|\ \ldots\ |^2$. Conversely, by knowing the Raman tensor, one may predict the scattering selection rules from this same term.

The Raman tensor in Eq.(1.3) has dimensions of 1/length. The scattering cross-section has dimensions of length-squared. The magnitude of the Raman tensor components is usually reported in length-squared units. The conversion factors required for relating these quantities are necessary only when obtaining actual matrix elements.

In this dissertation, no attempt is made to do so. Thus, cross-section, Raman-tensor element, and scattering efficiency are volume-independent, intrinsic properties; all these terms are used interchangeably. From Eq.(1.5) the measured scattering intensity is proportional to the scattering volume. The actual scattering <u>efficiency</u> (or, equivalently, the components of $\mathbf{R}$) cannot be obtained without knowledge of the effective sample "size." For opaque materials the optical penetration depth gives a measure of the scattering volume.

In infinite crystalline systems long-range order, i.e. translational periodicity, ensures that quasi-momentum is conserved in a scattering process. Equivalently, $\mathbf{k}$ is a quantum number for excitations within the crystal. Along with the conservation of energy (which holds in non-crystalline systems as well)

$$\hbar\omega_2 = \hbar\omega_1 \pm \hbar\omega \tag{1.6}$$

we have

$$\mathbf{k}_2 = \mathbf{k}_1 \pm \mathbf{q} + \mathbf{K} \tag{1.7}$$

(using the notation in Fig. 1.3) where K is any reciprocal lattice vector. Because $\mathbf{k}_1$ and $\mathbf{k}_2$ are small ($|\mathbf{k}_2 - \mathbf{k}_1| <$

10^6 cm^{-1}), and because the shortest reciprocal lattice vector is comparatively large ($|K_{MIN}| \cong 10^8$ cm^{-1}), first order Raman scattering requires (q within Brillouin zone) that $K = 0$. Consequently, $|q| < 10^6$ cm^{-1} ≈ 0 (relative to size of the Brillouin zone) for light scattering in crystals. Acoustic vibrations have linear dispersion for small q: $\hbar\omega = \hbar vq$, where v is the speed of sound in the scattering medium. Photons also have linear dispersion $\hbar\omega = \hbar ck/n$, with c the <u>in vacuo</u> speed of light and n the refractive index of the medium. The fact that $c/n >> v$ thus limits first-order crystalline Raman scattering to zone-center optical phonons.

The two atoms in the unit cell of GaAs have six degrees of freedom. Three of these are taken up by acoustic vibrations, leaving three for the optical modes. Since the optical modes in GaAs possess a dynamic charge, i.e. a vibration-induced electric dipole moment which does not cancel in the unit cell (no inversion center) [Zallen (1968)], the longitudinal-optical (LO) oscillations possess an additional restoring force that the transverse-optical (TO) phonons do not have [Huang]. This splits the LO vibrational bands from the (degenerate) TO bands. The phonon dispersion for c-GaAs is shown in Fig. 1.4 [Dorner & Strauch]. The c-GaAs Raman spectrum consists of a TO phonon line and a LO phonon line.

The translational symmetries of the full space group of a crystal account for the momentum conservation expressed in Eq.(I.7). Further selection rules for the light scattering may be obtained from the constituent molecular point group corresponding to the unit-cell factor group [Lax]. Point-group symmetry may require the scattering cross-section to vanish for certain light polarizations with respect to the crystal axes [Hayes & Loudon, p.43].

The spatial properties of excitations in the medium (phonon normal modes) may be described in terms of irreducible representations of the symmetry point group. Because they preserve the crystalline long-range order, Group theory is convenient for analyzing the $\mathbf{k} = 0$ excitations. Denoting the excitation irreducible representation Γ_x, from Eq.(I.2) for P' it is clear that P' and $(\chi'_0 \cdot \mathbf{x}) \cdot \mathbf{E}$ must have the same transformation properties in order to have scattering. Since P' and E are both polar vectors (Γ_{PV}), then $\Gamma_x \times \Gamma_{PV}$ (right hand side) must contain Γ_{PV} (left hand side). Equivalently, those Γ_x which transform like $\Gamma_{PV}^* \times \Gamma_{PV}$ are allowed. Thus the irreducible representation corresponding to a particular normal mode must correspond to a representation contained in the direct product $\Gamma_{PV}^* \times \Gamma_{PV}$ in order for Raman scattering from that particular vibration to be allowed. Nye has

computed Raman tensors for the 32 point-group symmetries.

The point group for the zincblende tetrahedral structure is T_d. The T_d group irreducible representations are listed in Table 1.2 [Cotton, p.362]. For the zincblende two-atom primitive-cell factor group, vibrations transform like $2\Gamma_{15}$. According to Table 1.2 these vibrational modes are Raman and infrared active. Raman tensors for the zincblende structure are listed in Table 1.3 [Cardona (1982), p.49]. When time reversal applies the antisymmetric components c are zero [Cardona (1982),p.50]. Since optical and acoustic phonons in zincblende possess Γ_{15} symmetry at $\mathbf{k} = 0$ [Hayes & Loudon, p.98], the bottom row of Table 1.3 is relevant here.

For backscattering along a $\langle 100 \rangle$ direction, Eq.(I.5) and the appropriate Γ_{15} tensors in Table 1.3 result in the selection rules summarized in Table 1.4. The standard Porto notation is used. For example $z(x,y)\bar{z}$ represents backscattering along the z axis with incident light polarized in the x direction and scattered light analyzed in the y direction. From $\{100\}$ surfaces, scattering from LO phonons is allowed and TO scattering is forbidden.

1.4 MICROSCOPIC RAMAN SCATTERING AND RESONANCE RAMAN

A microscopic treatment for processes such as those

indicated schematically in Fig. 1.3 involves absorption and emission of light via the interaction with electrons in the medium. The radiation part of the Hamiltonian may be written

$$H_{e\text{-}R} = \frac{e^2}{2m} \sum_i \hat{A}(r_i)\cdot\hat{A}(r_i) + \frac{e}{m} \sum_i \{\hat{A}(r_i)\cdot\hat{p}_i + \hat{p}_i\cdot\hat{A}(r_i)\} \tag{1.8}$$

where $\hat{A}$ represents the second-quantized radiation vector potential within the medium and p_i is the electron momentum operator. The sum runs over all electronic coordinates r_i. Between absorption and emission the electron (hole) in the conduction (valence) band inelastically scatters with a phonon. The electron-lattice interaction may be via the deformation potential or, for polar semiconductors such as GaAs, via the Fröhlich Hamiltonian.

The process depicted in Fig. 1.3(b-c) may be described by transition probabilities of the form

$$W_{2\,1} = \sum_{\alpha,\beta} \left| \frac{\langle 2|H_{e\text{-}R}|\beta\rangle\langle\beta|H_{e\text{-}L}|\alpha\rangle\langle\alpha|H_{e\text{-}R}|1\rangle}{(E_\beta - \hbar\omega_2)(E_\alpha - \hbar\omega_1)} + \ldots \right|^2, \tag{1.9}$$

where $|\alpha\rangle$ and $|\beta\rangle$ represent virtual intermediate states. For Fig. 1.3 all time orders (...) must be accounted for when considering the actual cross-section.

Raman scattering in resonance with various electronic processes has been reviewed by Cardona (1982). Resonance-Raman scattering effects occur when the photon absorption/emission matrix elements in Eq.(1.9) become large. This happens when the electronic (joint) density of states (DOS) is at a maximum, as with parallel bands. From the denominator of Eq.(1.9) it is clear that by tuning the incident (or scattered) photon energy to one of the interband transition energies where the DOS is large, resonance effects will be observed in $W_{2\,1}$. Resonance-Raman scattering thereby provides a probe of the electronic structure of a semiconductor, complementary in some sense to other optical techniques (absorption, reflectance, ellipsometry).

In Fig. 1.5 the electronic energy band structure is shown [Cohen & Chelikowsky]. For the photon-energy range studied here (1.55 to 2.71 eV), the optical properties are primarily governed by the upper-most valence (including the spin-orbit split-off band) and lowest conduction bands. Maxima in the joint electronic DOS occur at the direct transition energies 1.42 eV ($E_0 = E_{g\,a,}$), 1.77 eV ($E_0 + \Delta_0$), 2.9 eV (E_1), and 3.1 eV ($E_1 + \Delta_1$). Effective masses near the Γ point are listed in Table 1.1.

1.5 RAMAN SCATTERING IN SOLIDS DIFFERENT FROM BULK CRYSTALS

The Raman spectrum of microcrystalline silicon has been analyzed by Richter et al.. Their results were then extended to ion-implanted GaAs by Tiong et al.. In microcrystalline systems the Bloch wave functions of the infinite crystal are no longer applicable. The wave functions are (roughly speaking) restricted to the crystallite. Richter et al. imposed this spatial confinement by requiring

$$\Psi(q_0, r) \rightarrow C(r, r_0)\, \Psi(q_0, r) \tag{1.10}$$

where Ψ is the (Bloch) wave function of the infinite crystal with wave vector q_0 at position r. The confinement function C accounts for a crystallite size distribution about center r_0 with mean diameter ℓ via

$$C(r, r_0) \sim e^{-2|r - r_0|^2/\ell^2} \tag{1.11}.$$

Upon Fourier transformation this leads to

$$C(q_0, q) \sim \frac{\ell}{(2\pi)^{3/2}}\, e^{-|q - q_0|^2 \ell^2/8} \tag{1.12}$$

for a wave function with wave vector q_0 in the single crystal.

A physical interpretation comes from noting that when the crystallite size is very small, the long-

wavelength vibrations will interfere with the crystallite boundaries. Vibrations with short wavelengths will not be affected. As the crystallite decreases in size shorter wavelength phonons will interact with the confinement, which serves to break the crystal symmetry via elastic scattering. The symmetry breaking results in destruction of the $k = 0$ selection rule.

The essential feature for microcrystalline systems is that phonons with $k \neq 0$ may now participate in first-order Raman scattering. The longer wavelength vibrations are affected the most, with a weighting described by Eq.(1.12). Since the LO phonon dispersion in Fig. 1.2 has a maximum at $k = 0$, all of the new frequencies mixed in by the finite crystallite size are lower than $\omega(k = 0)$. Thus, the spatial confinement results in a frequency downshift as well as an asymmetric broadening extending toward lower frequencies. The shifting and broadening are therefore indications of the average crystallite size present in the microcrystalline system [Richter et al., Tiong et al.].

The Raman spectra of amorphous systems are also distinctly different from their crystalline counterparts. In amorphous materials the constituent molecular bonds (short range) are nearly identical to those in the crystal [Zallen (1983)]. Thus, the vibrational <u>energies</u> are similar. However, the long-range order, which is respon-

sible for the sharp spectral features and selection rules in the crystal, is no longer present. Although short-range order exists (e.g. nearly tetrahedral bonding environment, with small angle distortion of the bond angles) only, there is no translational periodicity and each vibrational excitation can no longer be characterized by a plane-wave eigenvector k.

Shuker and Gammon showed that in the small correlation length limit (i.e. $\ell \to 0$ in Eq.(1.12)) all vibrational modes of the amorphous system may participate in first-order Raman scattering. The Stokes spectrum will be given by

$$I(\omega) \sim C(\omega)\frac{n(\omega,T) + 1}{\omega} g(\omega) \qquad (1.13)$$

where C is the coupling coefficient and g is the vibrational density of states of the amorphous system. Thus, the Raman spectrum of an amorphous system is a reflection of the full density of vibrational states, modulated by the relatively mild frequency dependence of the coupling (or matrix element) factor $C(\omega)$. A similar situation exists for the infrared spectrum [Zallen, p.269 (see Fig. 6.8)].

From Fig. 1.2 for the crystalline phonon dispersion, transverse acoustic vibrations span 0 to 120

cm^{-1}, while the longitudinal acoustic vibrations go from 0 to 210 cm^{-1}. Optical modes have frequencies between 200 and 300 cm^{-1}. Thus, no gap exists in the vibrational DOS of the crystal. From this and the above comments, it is evident that the amorphous Raman spectrum (DOS) should span (roughly) 0 to 300 cm^{-1}, with no gap, and indeed this is found to be the case.

1.6 LOCAL MODES IN GaAs

When atoms, which are light compared to the host atoms, are substituted into the host, they will vibrate at a frequency higher than the lattice fundamental frequencies ($\bar{\nu}$ > 300 cm^{-1} for GaAs). Since host atoms can not vibrate at this high frequency, the oscillation of the impurity will not transmit through the lattice. Only nearest-neighbor atoms will be affected, resulting in a vibrational mode which is localized on the impurity site.

The point group for the zincblende tetrahedral structure is T_d. The T_d group irreducible representations are listed in Table 1.2 [Cotton, p.362]. The fifteen cartesian vectors transform like $\Gamma = \Gamma_1 + \Gamma_{12} + \Gamma_{25} + 3\Gamma_{15}$. Rotations transform like Γ_{25} and translations like Γ_{15}. The vibrations then transform like the remaining Γ_1, Γ_{12}, and $2\Gamma_{15}$ irreducible representations. From the right hand column of Table 1.2 labeled PV (polar vector), we can see

that the remaining Γ_{15} vibrations transforms in this manner (x,y,z), and are therefore infra-red active. The remaining vibrations are Raman active (Γ_1, Γ_{12}, and Γ_{15}), as indicated by the second-rank tensorial transformation properties of the Table 1.2 column labeled PV x PV.

Silicon tetrahedral substitution in GaAs may result in Si on either an As site (Si_{As}), an acceptor state, or a Ga site (Si_{Ga}), a donor state. The point group in either case is T_d, so that the vibrational modes have the same irreducible representations as the zincblende lattice (see Table 1.2). The impurity has a vibrational amplitude only in the triply degenerate Γ_{15} mode [Singh & Mitra]. At 77 K the frequencies are 384.0 cm^{-1} for $^{28}Si_{Ga}$ and 398.6 cm^{-1} for $^{28}Si_{As}$ [Talwar et al.].

Since silicon can substitute for either As or Ga, the possibility of Si_{As}—Si_{Ga} dimers exists. Such pairs have C_{3v} symmetry. Normal modes in which the impurities move are: two longitudinal ← → and → → , and two transverse ↑ ↓ and ↑ ↑ [Talwar et al.]. These modes are arranged in order of descending frequency. The axial stretching mode (← →) has a frequency of 463.7 cm^{-1} (77 K) and the transverse stretching mode (↑ ↓) is at 393.1 cm^{-1} [Theis & Spitzer]. At room temperature the frequencies of all these modes will be slightly reduced.

1.7 OUTLINE OF THIS DISSERTATION

In Chapter 2 the principal experimental apparati used for these experiments are described. Emphasis is given to procedures developed or modified particularly for this work.

In Chapter 3 an overview is given of the effect ion implantation has on the Raman spectrum of (100)-oriented GaAs. Ion species, energies, and fluences are varied; similarities and differences are discussed.

Chapter 4 is a presentation of a chemical-etch damage depth profile of 45-keV Be^+-implanted GaAs, obtained using Raman scattering. Photon-energy dependence of the Raman spectrum is introduced in some detail. The contents of Chapter 4 have been submitted to Physical Review B for publication by M.Holtz, R.Zallen, O.Brafman, and S.Matteson.

Chapter 5 is an outline of non-destructive damage depth profiles, obtained by varying the excitation photon energy. Two separate investigations were carried out: a 120-keV SiF_3^+ implant which results in an a-GaAs surface layer, and various implants for which the near-surface damage is not completely amorphous.

Chapter 6 is a discussion of the photon energy dependence of the a-GaAs spectral component, the micro-crystalline LO phonon component, and the observation of a

new, strong feature in the Raman spectrum of implanted (but not amorphous) GaAs. The fundamental origin of this new feature is discussed.

Chapter 7 pertains to silicon local vibrational modes in GaAs, where the silicon atoms are introduced into the host by ion implantation of Si^+ and SiF_3^+. For high doses, local modes are discussed both before and after annealing. Much of the content of Chapter 7 have been published by M.Holtz, R.Zallen, A.Geissberger, and R.Sadler in the Journal of Applied Physics (59, 1946 (1986)).

Chapter 8 is a summary of the results.

TABLE 1.1 Room Temperature GaAs Constants

Lattice constant a_o = 5.64 A, Bond length = $a_o(\sqrt{3}/4)$

Molecular density = 2.2139×10^{22} cm^{-3}

M_{Ga} = 69.720 amu M_{As} = 74.922 amu

$m_c = 0.063\ m_o$ †

$m_{hh} = 0.50\ m_o$ $m_{lh} = 0.088\ m_o$ $m_{soh} = 0.15\ m_o$

E_g = 1.423 eV

Δ_o = 0.341 eV

ϵ_o = 12.85 ϵ_∞ = 10.88

Bulk modulus = 7.55×10^{11} dyne/cm^2

Linear expansion coefficient $\alpha = 5.73 \times 10^{-6}$ K^{-1}

Specific Heat C_v = 0.327 J/g-K

Debye Temperature = 360 K

Conductivity (intrinsic electrical) = 3.0×10^{-9} Ω^{-1}-cm^{-1}

† Effective masses are identified from the different electronic energy band curvatures near the Γ point in Fig. 1.5: c = conduction, hh = heavy hole, lh = light hole, soh=split off hole.

J.S.Blakemore, J. Appl. Phys. 53, R123 (1982).

TABLE 1.2 T_d Point Group Properties

T_d	E	$8C_3$	$3C_2$	$6S_4$	$6\sigma_d$	PV	PV x PV
Γ_1 (A_1)	1	1	1	1	1		$x^2+y^2+z^2$
Γ_2 (A_2)	1	1	1	-1	-1		
Γ_{12} (E)	2	-1	2	0	0		$2z^2-x^2-y^2$, x^2-y^2
Γ_{25} (T_1)	3	0	-1	1	-1		
Γ_{15} (T_2)	3	0	-1	-1	1	x,y,z	xy,xz,yz
Γ	15	0	-1	-1	1		
Γ_T	3	0	-1	-1	1		
Γ_R	3	0	-1	1	-1		
Γ_V	9	0	1	-1	3		

$$\Gamma = \Gamma_1 + \Gamma_{12} + \Gamma_{25} + 3\Gamma_{15}$$

$$\Gamma_T = \Gamma_{15} \quad , \quad \Gamma_R = \Gamma_{25}$$

$$\Gamma_V = \Gamma_1 + \Gamma_{12} + 2\Gamma_{15} \quad \text{(Local Mode Vibrations)}$$

$$\Gamma_V = 2\Gamma_{15} \quad \text{(Zincblende Structure Factor Group)}$$

Group irreducible rep. from Cotton, p.362.

Factor group Γ_V from Lax.

Point group analysis from this work.

TABLE 1.3 Raman Tensors for the Zincblende Structure

$$\Gamma_1 : \begin{bmatrix} a & & \\ & a & \\ & & a \end{bmatrix}$$

$$\Gamma_{12} : \begin{bmatrix} b & & \\ & b & \\ & & -2b \end{bmatrix}, \begin{bmatrix} -\sqrt{3}b & & \\ & \sqrt{3}b & \\ & & \end{bmatrix}$$

$$\Gamma_{25} : \begin{bmatrix} & & c \\ & & \\ -c & & \end{bmatrix}, \begin{bmatrix} & & c \\ & & \\ -c & & \end{bmatrix}, \begin{bmatrix} & c & \\ -c & & \\ & & \end{bmatrix}$$

$$\Gamma_{15} : \begin{bmatrix} & & d \\ & & \\ d & & \end{bmatrix}, \begin{bmatrix} & & d \\ & & \\ d & & \end{bmatrix}, \begin{bmatrix} & d & \\ d & & \\ & & \end{bmatrix}$$

M.Cardona in Light Scattering in Solids, Vol.II, M.Cardona and G.Güntherodt, editors, (Springer-Verlag, Berlin, 1982).

TABLE 1.4 Selection Rules for Backscattering Along (100) in Zincblende

Polarization	LO(z)	TO(x)	TO(y)
$z(x,x)\bar{z}$	0	0	0
$z(x,y)\bar{z}$	d^2	0	0
$z(y,y)\bar{z}$	0	0	0
$z(x',x')\bar{z}$	d^2	0	0
$z(x',y')\bar{z}$	0	0	0
$z(y',y')\bar{z}$	d^2	0	0

FIGURE CAPTIONS

Fig. 1.1 : Diagram of the cubic zincblende lattice.

Fig. 1.2 : Brillouin zone of the face-centered cubic lattice of GaAs.

Fig. 1.3 : Pictorial representations of the first-order Raman-scattering process: (a) Billiard ball diagram with $(\mathbf{k}_1, \omega_1)$, $(\mathbf{k}_2, \omega_2)$, and $(\mathbf{q}, \omega)$ the wavevectors and frequencies of the incident photon, scattered photon, and phonon, respectively. (b) Interband Raman scattering for electrons and holes. (c) Feynmann diagrams for the process in (b) using the notation of (a) with the inter-action vertices H_A and H_{EL} for electron-radiation and electron-phonon, respectively.

Fig. 1.4 : GaAs phonon dispersion from Dorner & Strauch.

Fig. 1.5 : Partial GaAs electronic energy band structure after Cohen & Chelikowsky.

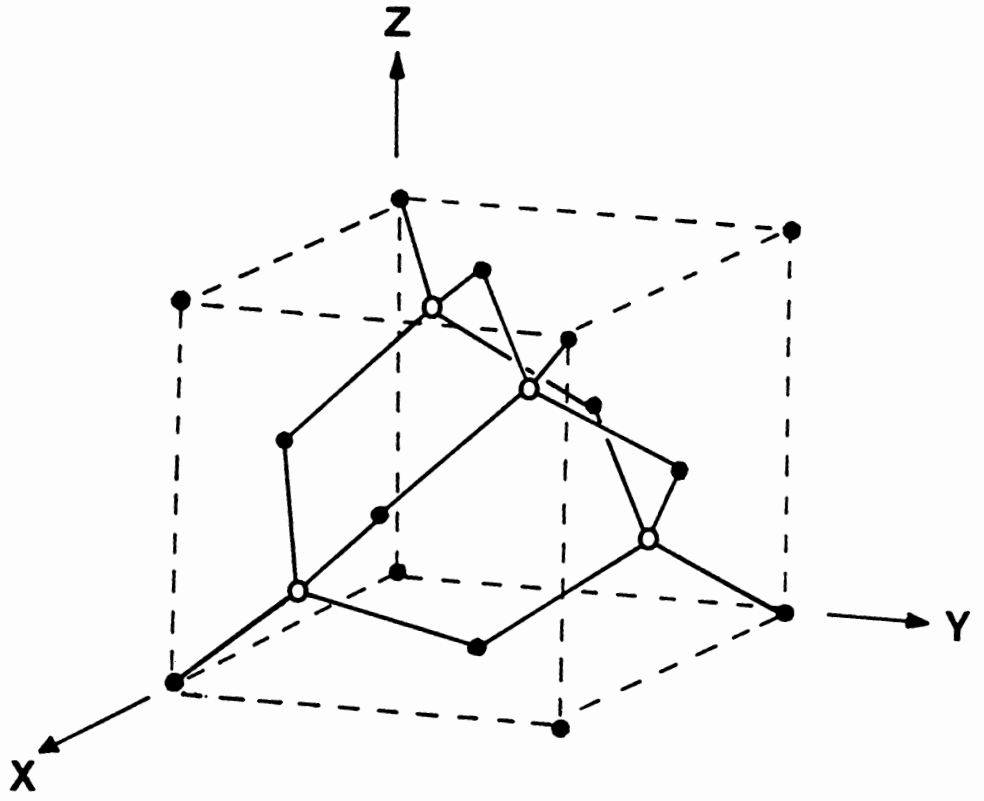

ZINCBLENDE

LATTICE

Fig. 1.1 Conventional cell of the zincblende lattice.

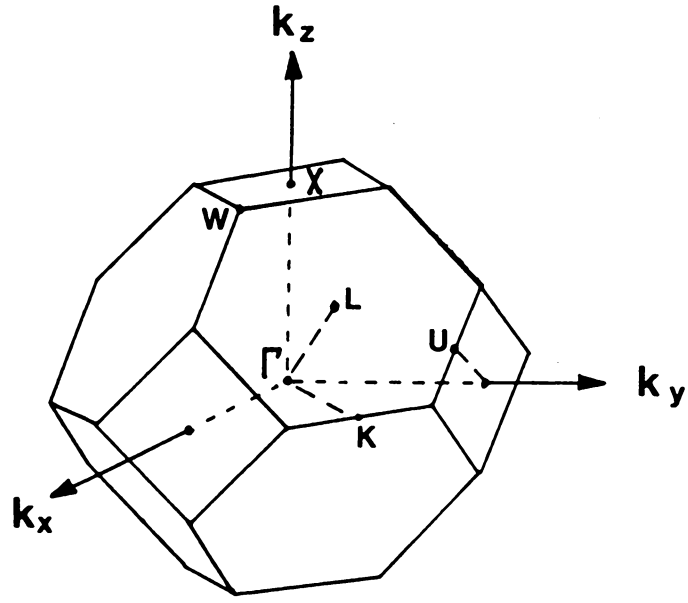

GaAs

BRILLOUIN ZONE

Fig. 1.2 Brillouin zone of the FCC lattice.

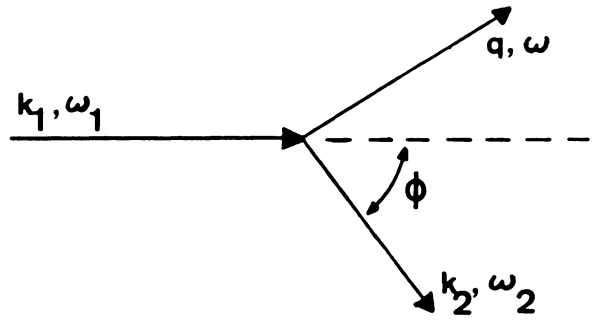

a

b

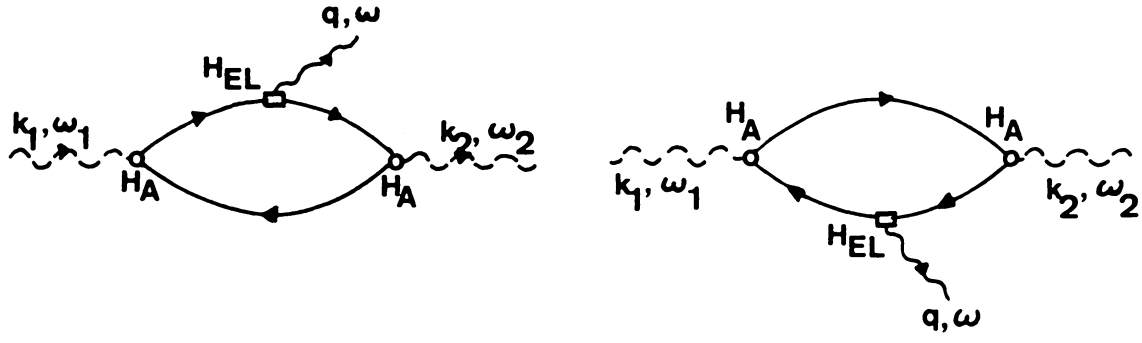

c

Fig. 1.3 Schematic representations of Raman scattering.

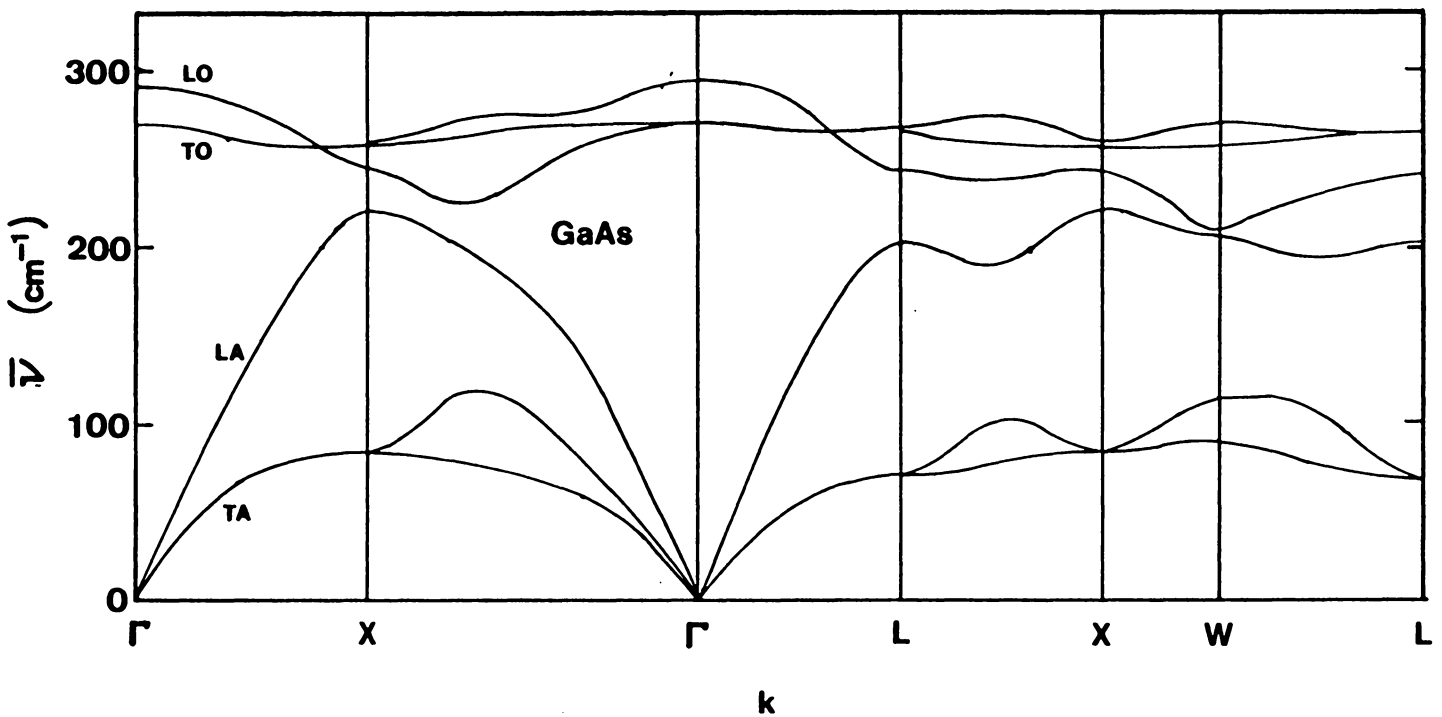

Fig. 1.4 Phonon dispersion for GaAs.

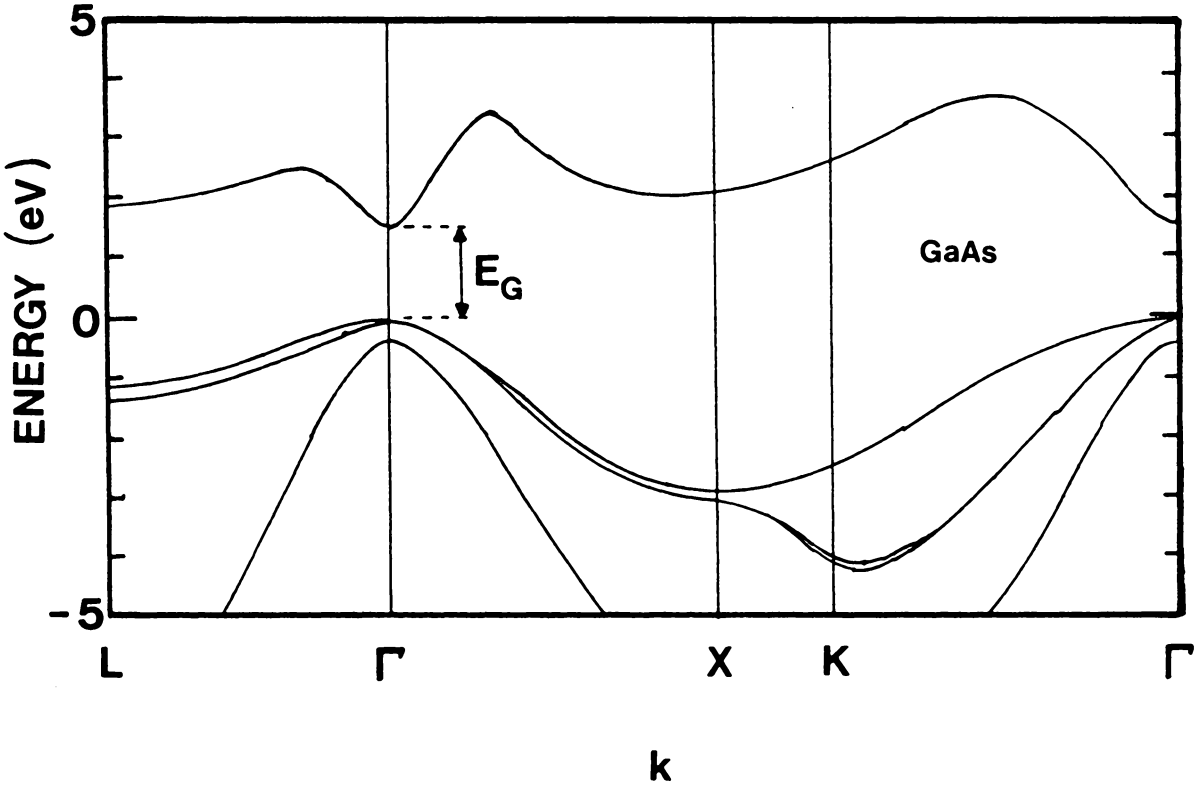

Fig. 1.5 Electronic energy bands for GaAs.

CHAPTER 2: EXPERIMENTAL ASPECTS

GaAs single crystals (c-GaAs) used in these experiments were (100)-oriented, commercially grown by the liquid encapsulated Czochralski (LEC) method. Specimens provided by Texas Instruments were chromium doped, semi-insulating single crystals; those provided by ITT were undoped, semi-insulating single crystals. Crystals were cut, then polished using a sequence of graded abrasives. Remaining pits and scratches were removed by etching in 8:1:1 (TI) or 5:1:1 (ITT) H_2SO_4 : 30% H_2O_2 : H_2O to yield smooth surfaces with excellent optical quality.

Ion implanting was carried out at room temperature by TI or ITT in commercial implanters. Ions were implanted 7° to 9° from the (100) normal in order to reduce the probability of ions traveling deep into the crystal by passing relatively unimpeded down a crystalline channel. By implanting away from any of the primary crystalline axes the spatial distribution of the host lattice sites will appear to be nearly random, decreasing the effect of this so-called "channeling" phenomenon. The randomness of the target atom distribution also facilitates prediction of the ion concentration, which is made tractable for completely random targets [Gibbons et al., Ziegler et al.].

Various ion species and implant energies were used

in these experiments. These parameters are summarized in Table 2.1. The implants studied represent a wide range of implant ion masses and energies, which results in a wide range of ion damage to the substrate. 28-amu Si^+ ions were used by ITT because they are the dominant silicon species, 29-amu Si^+ ions are used for device-quality implanting to discriminate against N_2 which has a molecular mass of 28 amu. Ignoring this slight difference in the silicon masses, the predicted peak in the ion concentration (and maximum projected range into the sample) occurs at a depth of 1000 (1800), 1300 (2200), and 1600 (2600) A from the surface for 120-, 150-, and 180-keV Si^+ ions, respectively [Gibbons et al.]. For beryllium we estimate 1000 (2400) and 4000 (7000) A for 45- and 180-keV Be^+ ions, respectively [Gibbons et al.]. The nature of the SiF_3^+ ion range shall be discussed in Chapter V. As shall be discussed shortly, the importance of the ion ranges is that they must be significant with respect to the optical penetration depth of the light used to excite the Raman spectrum.

In addition to the ion-implanted GaAs, amorphous GaAs (a-GaAs) films were obtained for Raman-scattering experiments which were prepared via "standard" techniques for amorphous semiconductors [Zallen]. The flash-evaporated a-GaAs film studied was provided by A. Gheorghiu and M-L. Theye of the Université Pierre et Marie Curie, Paris

[Theye & Gheorghiu]. The 785-A thick film was evaporated onto a glass slide. Sputtered a-GaAs was obtained from J. Burnett and W. Paul of Harvard University. These films also were supported by a glass slide.

For the annealing studies, implanted samples were encapsulated with a 2000-A thick layer of SiO_2 by chemical-vapor deposition, in order to prevent GaAs stoichiometric degradation through As loss at the surface. The encapsulant was then stripped off using hydrofluoric acid following the anneal and prior to Raman measurements. The anneal was either a standard furnace anneal (SFA) at 850° C for 20 minutes in flowing nitrogen with 10% hydrogen (forming gas), or a rapid thermal anneal (RTA) under a commercial quartz-halogen lamp system at about 950° C for 6 to 12 seconds in pure nitrogen. All annealed samples (discussed in Chapter 7) were 120-keV Si^+ or SiF_3^+ implants (ITT), found to be n-type by Hall measurements.

The depth profiling was accomplished using a weak acidic solution of 1:1:100 H_2SO_4:30% H_2O_2:H_2O [McLevige]. Etching was done at room temperature for up to six minutes, in one-minute steps. The etch was calibrated by masking a narrow strip with polymethyl methacrylate photoresist prior to successive etches. The etching was performed in successive one-minute steps with the aid of a rack and pinion mount. The resist was then removed and the step

height of the masked area was determined using a stylus profilometer (Tencor Instruments, Alpha-Step) and by Tolansky Interferometry [Tolansky] (at Texas Instruments). Because the damage is expected to affect the etch rate, both pristine crystal and heavily implanted (5×10^{14} cm^{-2}) samples were measured. Depth versus etch time results for these samples are shown in Fig. 2.1. The unimplanted crystal is seen to etch uniformly at a rate of about 530 A/minute, in excellent agreement with a reported result [Ryssel & Ruge]. The ion damaged material etches more quickly, approximately 660 A/minute, and is expected to etch at the same rate as the crystal beyond the damaged region.

Conventional Raman spectra were collected using visible light as excitation in the single-frequency, cw mode. The Krypton-ion laser used (Coherent,Innova 90-K) has laser lines from 5682 to 6764 A using standard optics, as well as two near-infrared laser lines (7525 and 7993 A) obtainable by use of special optics, all listed in Table 2.2. Also in Table 2.2 are the <u>in vacuo</u> wavelengths for the Argon-ion laser source (Coherent, Innova 90-5) used in these experiments. The Argon-ion lines span 4579 to 5145 A. The two-laser capability thus provides a spectral range from 4579 to 7993 A (2.71 to 1.55 eV), which nearly spans the entire visible spectrum of the human eye. Output power

stability is better than a few percent per hour, following the standard thirty-minute warm up.

In order to discriminate against spurious laser plasma lines, the plane-polarized laser light is passed through a grating tunable excitation filter. This filter has an f/4 aperture and a 1200 gr/mm grating, resulting in a resolution of 12 A. At 4579 A this resolution translates into 60 cm^{-1} and at 7993 A it has a resolution of 20 cm^{-1}. The overall efficiency of the bandpass filter is typically 50%. The resulting nearly pure, single-frequency light is then passed through an all-lines polarization rotator before it is focused onto the sample using a spherical lens with a 4.5 cm focal length.

Since GaAs is opaque to visible light, a near-back-scattering geometry is appropriate in which the incident light is directed onto the sample at ~ 40° from the normal. In GaAs this results in an internal incident angle of $\leq$ 10° from the normal direction. The (100) back-scattering selection rules are therefore only approximately correct. Scattered light is collected in a cone around the (100) normal. In this manner the primary reflection is not passed into the spectrometer, which greatly aids in discrimination against stray light. The experimental set-up is diagrammed schematically in Fig. 2.2.

For c-GaAs, 5145-A laser light has an optical

penetration depth d_{OPT} (= $1/2\alpha$ for back-scattering, where α is the optical attenuation coefficient) of approximately 550 A [Aspnes & Studna]. For 5145-A light in a-GaAs d_{OPT} = 140 A [Theeten & Erman]. Estimates for d_{OPT} at the pertinent laser photon energies are listed in Table 2.3. The higher photon energies in the visible therefore probe only a narrow surface region in GaAs which is on the order of or smaller than the implanted ion ranges cited above. This makes Raman scattering an excellent way to study these shallow implant damaged regions. For studying variations in the Raman spectra of such regions, it is extremely important to understand the spatial variations in the damage over the depth of the probe.

For highly reflecting specimens, the focus of the laser at the sample is sufficiently intense to excite the vibrational and rotational Raman spectra of the N_2 and O_2 molecules (primarily) present in the atmosphere when collecting room temperature spectra. The spectrum of "air" was collected using 5145-A light by focusing the light in front of the spectrometer collection optics. Intensity of the laser source was increased by reflecting the beam back to the point of focus using a spherical mirror. The spectrum is shown in Fig. 2.3. Since this air spectrum will be superposed upon the GaAs spectrum, the air in the immediate surroundings of the point at which the laser is

focused was purged by a constant stream of argon gas. Without this steady flow of argon the low-frequency spectrum would be difficult to interpret. Conversely, the frequency of the sharp air lines can be used similar to the way laser plasma lines are used to obtain precise frequency calibrations.

In order to estimate Raman-scattering intensities between different samples and for different laser photon energies, an external, transparent reference standard was used. CaF_2 is transparent throughout the visible, and has constant Raman-scattering efficiency below 5 eV [Cardona, p.45]. CaF_2 possesses a strong line at 322 cm^{-1}, in very close proximity to the c-GaAs longitudinal optical (LO) line at 292 cm^{-1}. This makes simultaneously collecting the GaAs intensity and the CaF_2 intensity unreliable. Evaporating CaF_2 onto each specimen is impractical due to the number of different samples studied and the obvious heating consequences.

A kinematic replacement procedure was developed to overcome this dilemma. The GaAs sample is mounted in front of a removable shim, which is machined to the same thickness as the CaF_2 to be used for the calibration. The GaAs LO intensity is measured with the flat shim in place. The shim is then carefully removed and the CaF_2 crystal is placed on <u>top</u> of the same GaAs piece just measured. Thus,

the CaF_2 surface is in the same position as the GaAs surface was when it was measured. The CaF_2 322 cm^{-1} line intensity is then measured with no further adjustments made to the sample configuration or the optical alignment, giving the external reference calibration desired.

The advantage of this CaF_2 normalization process is that it removes the question of spectrometer preference to a given photon wavelength range (blaze, spectral bandpass, detector response, etc.) over the broad range used. Also, the laser source intensity is taken care of along with the usual λ^4 factor. The disadvantage is that several operations are involved which naturally limit the precision. The GaAs spectra were always collected with an entrance slit height of 2 mm. By measuring the CaF_2 intensity with a 2 cm entrance slit height it was found that repeatability was improved dramatically, due to the thickness ot the CaF_2 (1 mm) and the resultant scattering volume. The slit height did not affect the GaAs intensity. By increasing the slit widths (both GaAs and CaF_2) precision is also improved and measurement time is decreased. Carefully repeated measurements resulted in ~ 3% error; however, a conservative expected precision of no better than 10% is expected, especially for the weaker Krypton-ion laser lines which are difficult to see.

For variation of the GaAs temperature, the specimen

was kept in contact with the cold finger of a closed-cycle compressed-helium cryostat (Cryosystems, 22C Cryodyne). Temperature control from 15 to 300 K was achieved by using a silicon diode detector mounted to the cold finger and a cryostat controller (Palm Beach Cryophysics, model 4075) used directly or operated by computer using the PZ-80 IEEE-488/RS-232 converter interface designed and built by Roger Link of the Virginia Tech Physics Electronics Shop. A near-backscattering geometry was employed. Because of the large amount of space required for the cryostat head, the efficiency of the collection optics was reduced significantly.

Scattered light is collected by an f/1.4 elliptical mirror which subtends a solid angle of ~ 2/3 steradians. (Cryostat dimensions require a reduction of this collection angle by a factor of nearly 1/4.) In using an elliptical mirror one attempts to position the sample (point at which laser is focused) at one focus of the ellipse and simultaneously have the spectrometer entrance slit at the other ellipse focus. The collection optics are designed so that when the sample mount is correctly placed the maximum solid angle (defined by the spectrometer optics) is subtended by the focused light. One then takes full advantage of the spectrometer maximum efficiency (and resolution). A 90° mirror is used to direct the converging

light into the spectrometer entrance.

Prior to the entrance slit, the light may be filtered by a polarizing film for analysis. The light is also passed through a quarter-wave plate, or polarization "scrambler" [Jenkins & White, p.564]. Plane-polarized light will emerge with circular polarization after passing through the scrambler. This defeats the preference of the gratings to diffract one polarization more readily than the other, which may result in incorrect spectra.

Raman spectra are dispersed using a SPEX 1403 double monochromator, shown schematically in Fig. 2.5. The monochromator has a focal length of 0.85 m with an f/7.8 aperture. Gratings are holographically generated, measuring 11.0 cm x 11.0 cm with 1800 gr/mm used in first diffraction order. Mounts for the gratings are Czerny-Turner cosecant type with a single lead screw driving both gratings. Using this arrangement makes $\bar{\nu}$ $(1/\lambda)$ proportional to angular rotation of the lead screw. The full spectral range is 11,000 to 31,000 cm^{-1}.

Grating angle is controlled by the SPEX DATAMATE. The spectrometer position is controlled to within 0.1 cm^{-1}, with the aid of a stepper motor (Bodine Electric, 23-T-1BEHH) and control card. The controller removes lead screw backlash by sending the spectrometer 50 cm^{-1} above the scanning start point. Data are collected for the

prescribed integration time, after which the spectrometer is incremented to the next position in a decreasing (absolute) wavenumber direction.

Light focused into the spectrometer should subtend the solid angle defined by mirror M1 and entrance slit S1 in Fig. 2.5. The diverging light collected by M1 is collimated upon reflection toward grating G1. Filling mirror M1 results in full usage of the surface area of G1, improving the grating resolution since it is in proportion to the number of grooves illuminated (total path difference). Light diffracted to mirror M2 is still collimated, so that M2 focuses the light through intermediate slit S2 and onto mirror M3. The second stage of the double monochromator is a mirror image of the first stage. Mirrors M1, M2, M4, and M5 are approximately 10 cm in diameter, aluminized and overcoated with MgF_2 for protection. Although these spherical mirrors are used slightly off-axis, some of the consequent aberration from M1 (M4) is compensated for by M2 (M5) [Hayes & Loudon, p.76].

Although the use of the double monochromator reduces throughput by a factor of two, this loss of efficiency is more than compensated for by the increased ability to discriminate against Rayleigh scattering of the laser line. This "spectral purity" is 10^{14} when the

spectrometer is 20 cm^{-1} from the laser frequency.

The 1403 monochromator is fitted with four straight slits. S1 and S4 (entrance and exit) control spectral resolution while S2 and S3 primarily serve to block stray light from passing into the second stage, and eventually to the detector. Slit S3 is an extremely important addition (circa 1980) to the SPEX double monochromator. Prior to this added spatial filtering, spectral purity in the SPEX 1401 was 10^{11} at 100 cm^{-1} (!) [Hayes & Loudon]. Slit widths may vary from 10 μm to 3 mm. In practice, S1 and S4 are not precisely aligned below 50 μm and S2 and S3 block diffracted light below 200 μm.

The resolving power of a grating instrument is the ability to discern between distinct features at ν and $\nu + \Delta\nu$:

$$R = \lambda/\Delta\lambda = \nu/\Delta\nu = \bar{\nu}/\Delta\bar{\nu} = mN \qquad (2.1)$$

where m is the (integer) diffraction order and N is the number of grating grooves. The slit width affects the overall resolution through the linear dispersion, $\Delta\ell/\Delta\lambda$, at the focal plane ℓ [Jenkins & White, p.362]. That portion of the diffraction order passed through the slit is dependent upon the angular dispersion and the slit width. A convenient quantity for this purpose is the spectral

bandpass of the instrument. The bandpass is a function of the reciprocal linear dispersion, $\Delta\bar{\nu}/\Delta\ell$, which depends on wavelength λ, grating constant, instrument focal length, and spectral order. For the 1403 the spectral bandpass B is related to the linear dispersion and slit width by

$$B = \frac{W}{\Delta\ell/\Delta\bar{\nu}} \qquad (2.2).$$

The approximate reciprocal linear dispersion is (empirically) related to wavelength by

$$\Delta\ell/\Delta\bar{\nu} \approx 0.043\ \lambda - 140 \quad (\text{in } \mu/\text{cm}^{-1}) \qquad (2.3)$$

when λ is expressed in A. The spectral bandpass is then found from Eqs. (2.2, 2.3) by knowing laser wavelength λ and W for S1 and S4. The resolution can be improved by decreasing entrance and exit slit widths (note: intensity ~ slit width squared), until the slits have the same dimensions as that of the sample focus passing through S1, below which no further resolution is possible.

Resolution is also affected by the entrance slit height. The 1403 is equipped with 2 mm, 1 cm, and 2 cm rectangular slit height limits as well as three circular Hartmann apertures. Increasing the slit height will decrease resolution due to the spherical nature of the

incident wavefront. All spectra reported here were taken using a slit height of 2 mm.

The air spectrum shown in Fig. 2.3 is a good demonstration of the 1403 resolving power. Taken with a 0.5 cm^{-1} spectral bandpass, the peak near 60 cm^{-1} is in fact a doublet. This is confirmed by close examination of this very finely meshed spectrum (see inset in Fig. 2.3). The 60 cm^{-1} doublet also indicates excellent spectrometer stability. The data represents multiple scans lasting a total time of about eight hours. Spectrometer drift may be caused by a variety of influences, particularly temperature. Over the fairly long time period involved, stability is shown to be excellent. One final note is that by halving the S1 and S4 slit widths the weak feature in the Raman spectrum of air at 2.0 cm^{-1} was also resolved from the Rayleigh line.

Spectral bandpass affects the observed linewidth of a peak with natural linewidth Γ_0. If the spectral bandpass is B, then the observed linewidth is given by

$$\Gamma^2 = \Gamma_0^2 + B^2 \qquad (2.4)$$

for small B. Typical bandpasses used here are 2 to 5 cm^{-1}. Thus, when comparing intensities for narrow Raman lines, the natural linewidth must be used, making the slit widths

an important experimental parameter.

Scattered light which succeeds in passing through the spectrometer exit slit is focused by a condenser lens and detected by a photomultiplier tube (PMT). The PMT (RCA, C31034A-02) has a highly sensitive GaAs photocathode with an eleven-stage, in-line copper beryllium dynode structure. Tube temperature is maintained at approximately - 20° C using a thermo-electric cooler. At this temperature with an operating voltage of - 1400 V, the dark count is very low, from 5 to 25 cps. The response of the PMT varies by less than 20 % over the wavelength range 3000 to 8500 A.

The photomultiplier spike output is discriminated and converted to square voltage pulses and collected in the standard photon-counting mode. No count-rate saturation was observed up to 10^5 cps. The data pulses are counted by the SPEX DATAMATE minicomputer spectrometer controller (M-6800 based). Data are normalized to cps, and may be stored in one of eight working data files. Data may then be written onto floppy diskette and/or plotted using a Houston Instruments DMP-40 plotter, accessed by using the DATAMATE BASIC. Data may be transferred over RS-232 to other computers using the TRA command. An example is the NEC APC-III, for which a receive program is listed in Appendix 1. Also listed in Appendix 1 are programs for using the APC-III to plot data using the DMP-40.

Signal averaging was accomplished by collecting multiple spectra on a given specimen successively. The spectra are directly added, thereby increasing the data collection time. This is preferred to single, long data scans because of possible loss of laser output power over the long time periods often involved. Clean spectra of the silicon local modes in GaAs (Chapter 7) require as much as 100 hours of signal averaging. Data may be smoothed using a simple boxcar averager. Fine spectral details may be lost in this process, so it is generally avoided.

TABLE 2.1 Summary of Implant Fluences and Energies by Ion Species.

- TI -

$^{9}Be^{+}$		$^{29}Si^{+}$	
1×10^{13} cm^{-2}	45 keV	2×10^{13} cm^{-2}	180 keV
5×10^{13} cm^{-2}	"	1×10^{14} cm^{-2}	"
1×10^{14} cm^{-2}	"	5×10^{14} cm^{-2}	"
5×10^{14} cm^{-2}	"		
5×10^{14} cm^{-2}	180 keV		

- ITT -

$^{28}Si^{+}$		SiF_3^{+}	
6×10^{12} cm^{-2}	120 keV	6×10^{12} cm^{-2}	120 keV
2×10^{13} cm^{-2}	"	1×10^{13} cm^{-2}	"
8×10^{13} cm^{-2}	"	4×10^{13} cm^{-2}	"
2×10^{14} cm^{-2}	"	2×10^{14} cm^{-2}	"
1×10^{15} cm^{-2}	"	4×10^{14} cm^{-2}	"
3×10^{15} cm^{-2}	"	8×10^{14} cm^{-2}	"
1×10^{16} cm^{-2}	"	1×10^{15} cm^{-2}	"
		3×10^{15} cm^{-2}	"
1×10^{13} cm^{-2}	150 keV	1×10^{16} cm^{-2}	"
5×10^{13} cm^{-2}	"	3×10^{16} cm^{-2}	"
1×10^{14} cm^{-2}	"	1×10^{17} cm^{-2}	"

TABLE 2.2 Laser Wavelengths (*in vacuo*), Photon Energies, Frequencies, and Maximum Output Powers for Coherent Lasers.

λ (A)	$\hbar\omega_L$ (eV)	λ^{-1} (cm^{-1}) (meas)	Power (mW)
Argon-ion			
4579	2.712	21838.8 (21834.6)	400
4658	2.666	21468.4	-
4727	2.628	21155.1	-
4765	2.607	20986.4	-
4880	2.545	20491.8 (20490.6)	2000
4965	2.502	20141.0	-
5017	2.476	19932.2	-
5145	2.414	19436.3 (19433.6)	2400
Krypton-ion			
5682	2.186	17599.4 (17598.7)	150
6471	1.919	15453.6 (15453.4)	600
6764	1.836	14784.2 (14782.7)	140
7525	1.651	13289.0 (13288.0)	150
7993	1.554	12510.9 (12509.0)	50

TABLE 2.3 Optical Penetration Depth ($d_{OPT} = 1/2\alpha$) into Crystalline and Amorphous GaAs for Relevant Photon Energies.

$\hbar\omega_L$ (eV)	λ (A)	c-GaAs * d_{OPT} (A)	a-GaAs † d_{OPT} (A)
1.554	7993	3900	670
1.651	7525	2600	510
1.836	6764	1800	330
1.919	6471	1500	270
2.186	5682	800	190
2.414	5145	550	140
2.545	4880	450	110
2.712	4579	260	90

* Aspnes & Studna

† Theeten & Erman

FIGURE CAPTIONS

Fig. 2.1 : Calibration of the GaAs etch rate for the weak etchant used to depth profile. Both unimplanted c-GaAs and GaAs implanted with 45-keV Be^+ to a fluence of 5×10^{14} cm^{-2} were calibrated.

Fig. 2.2 : Schematic of the experimental setup used.

Fig. 2.3 : Raman spectrum of air. For low-frequency spectra from highly reflecting specimens the air must be purged in the neighborhood of the focused laser. Note the doublet near 60 cm^{-1} (inset).

Fig. 2.4 : Schematic of the SPEX 1403 double monochromator used to measure Raman spectra.

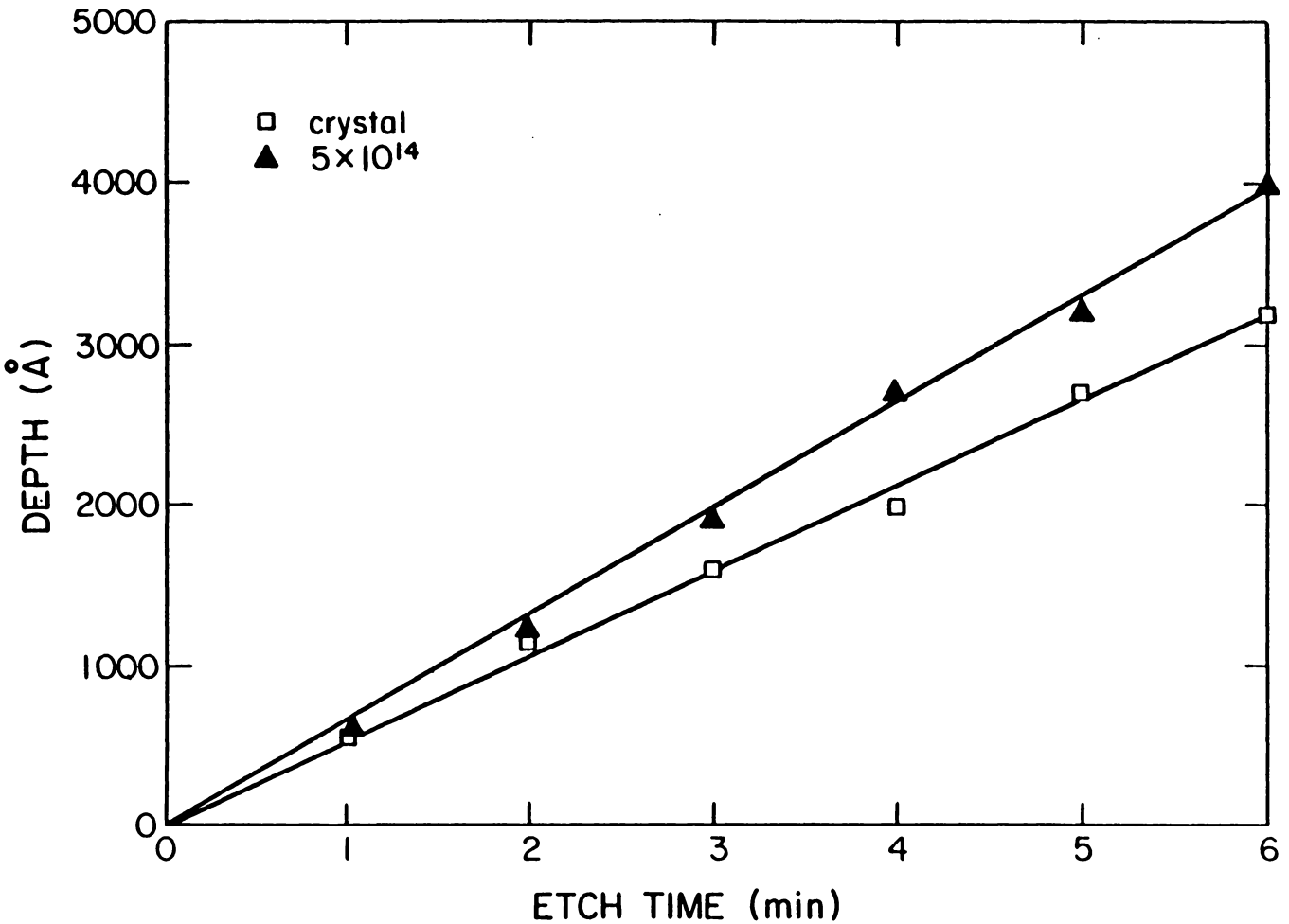

Fig. 2.1 Etch rate calibration.

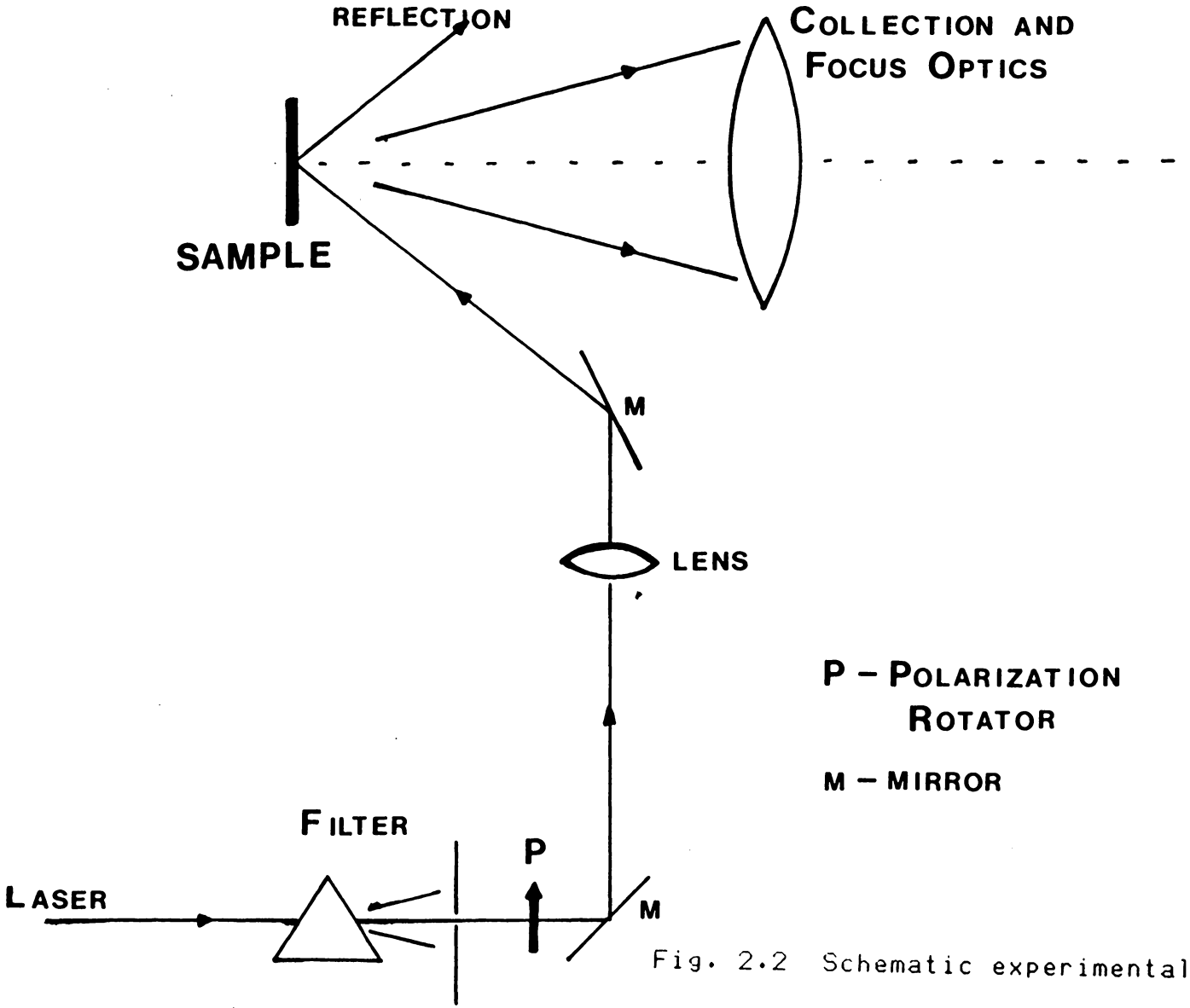

Fig. 2.2 Schematic experimental diagram.

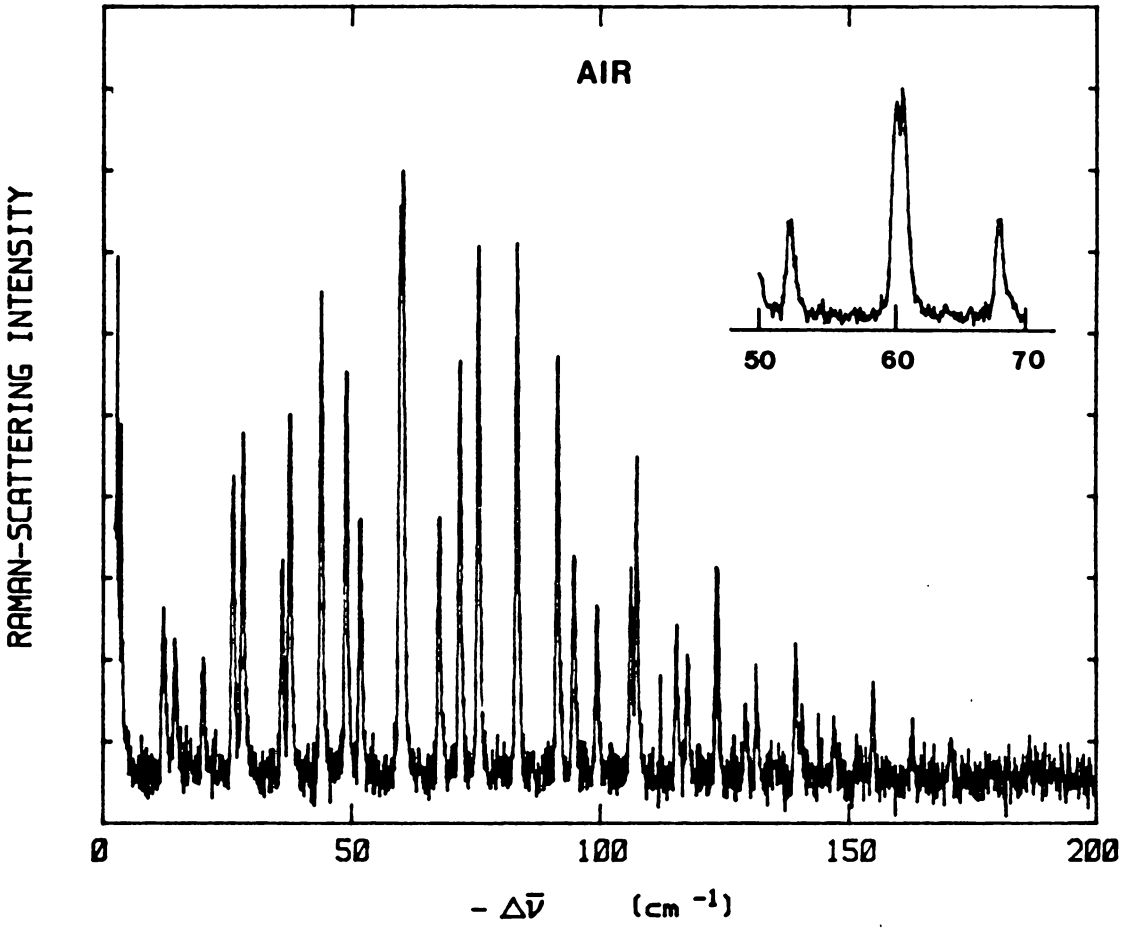

Fig. 2.3 High-resolution Raman spectrum of air.

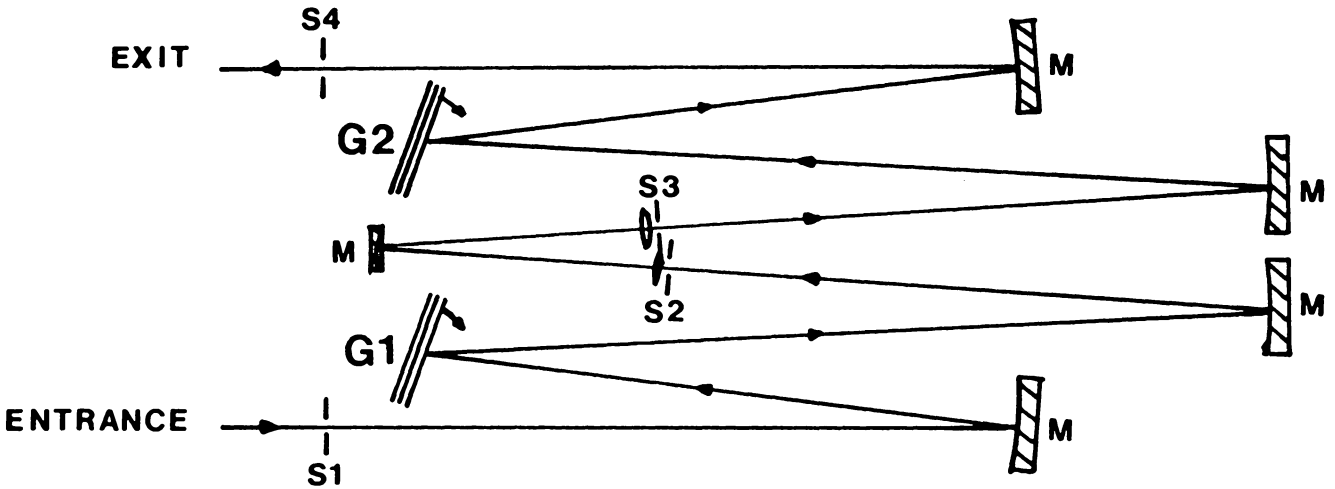

G – GRATING

M – MIRROR
S – SLIT

SPEX 1403

Fig. 2.4 Schematic of double monochromator.

CHAPTER 3: RAMAN-SPECTRUM CHARACTERIZATION OF IMPLANTATION-INDUCED DAMAGE IN GaAs

3.1 OVERVIEW OF RAMAN SPECTRA FOR VARIOUS INPLANT CASES

In Figs. 3.1 - 3.6, implant fluence sequences are exhibited for a variety of ion species and energies (5145-A, 2.41-eV green light as excitation). The (100) crystal is shown in Figs. 3.1, 3.3, and 3.6. All three spectra are identical, exhibiting a strong LO signal at 292 cm^{-1} (FWHM = 3.0 cm^{-1}) since we are backscattering along (100). Also evident in the crystalline spectrum is a weak TO line at 269 cm^{-1}. This symmetry-forbidden peak is observed here because a true 180° backscattering geometry was not employed, and because scattered light is collected in a cone around the (100) normal. In all spectra shown, the laser line "parasitic" scattering is small due to the excellent optical quality of all samples and due to the stray light rejection capability of the monochromator.

Figure 3.1 is for the 45-keV Be^+ implants (CaF_2 intensity standard). Figure 3.2 is the 180-keV Be^+ implant. Figures 3.3, 3.4, and 3.5 are all Si^+ implanted GaAs for varying ion energies, 120, 150, and 180 keV, respectively. In Fig. 3.6 the implant species is the heavy SiF_3^+ ion (85 amu), implanted at 120 keV, which produces a fully amorphized surface layer, as shall be discussed.

Common to all the implant sequences in Figs. 3.1 - 3.6 is the LO phonon, which shifts down in frequency (with increasing fluence) while broadening and losing intensity (Fig. 3.1 for intensities, see also Ch.4). This LO line has been successfully identified as that of the microcrystalline remnant of GaAs by Tiong et al.. In their analysis, the LO has a frequency-dependent intensity (from Eq.(1.10))

$$I(\omega) \sim \int_{BZ} d^3q \; C(0,q)^2 \; \frac{1}{(\omega - \omega(q))^2 + (\Gamma_0/2)^2} \tag{3.1}$$

where C is from Eq(1.12) and Γ_0 is the crystalline LO line width, 3.0 cm^{-1}. They assumed a spherical, spherically symmetric Brillouin zone and used

$$\omega(q) = 269.5 + 22.5 \cos(\pi q), \text{ in } cm^{-1} \tag{3.2}$$

for the LO dispersion. By varying the average crystallite size ℓ in C, and numerically generating $I(\omega)$, they were able to correlate the LO peak shift and line width (i.e. line shape) with crystallite diameter, for small enough crystallites ($\ell \leq 200$ A). Results for 270-keV As^+ implanted GaAs were in good agreement with experiment.

In Fig. 3.7 the theoretical curve of Tiong et al.

is shown with experimental results from Figs. 3.1 - 3.6 for the LO line of the microcrystalline remnant (also listed in Table 3.1 are the ℓ values from $\bar{\nu}_{LO}$). It was found here that subtraction of the a-GaAs component of the spectrum (to be discussed soon) was important. The results are in satisfactory agreement with theory, better for less-damage cases.

The importance of Fig. 3.7 is that spectroscopic evidence supports the presence of a microcrystalline remnant in the ion-implanted GaAs, independent of ion species or energy. Spatial correlation (confinement) [Richter et al.] is seen to be a valid description of the breakdown of crystalline selection rules in microcrystalline systems.

The agreement between theory and experiment in Fig. 3.7 is good enough to use for <u>estimating</u> average crystallite sizes present in ion-bombarded GaAs. The <u>actual</u> ℓ cannot be taken too seriously, but <u>trends</u> for fairly large variations in ℓ can be characterized.

3.2 COMPARISON OF ION-DAMAGED GaAs TO a-GaAs

Another qualitative observation on the implant sequences (Figs. 3.1 - 3.6) is that the silent region of the c-GaAs spectrum (0 to 300 cm^{-1}, LO and TO excluded) shows a three-band Raman spectrum which increases in intensity with fluence. For the 120-keV SiF_3^+ implant

sequence of Fig. 3.6 an implant fluence of 2×10^{14} cm^{-2} completely quenches the LO microcrystallite remnant. Simultaneously, the three-band spectrum grows stronger.

In Fig. 3.8 the Raman spectrum is shown for GaAs implanted five separate times with 120-keV SiF_3^+, each time to a fluence of 2×10^{14} cm^{-2}. This is compared to the Raman spectrum of a-GaAs prepared via flash evaporation and sputtering. All three spectra are very similar. This therefore constitutes spectroscopic evidence that sufficient ion implantation results in a surface layer of a-GaAs.

This result is important, yet it remains somewhat qualitative. To support it further the depolarization ratio was measured. The depolarization ratio, ρ, is a characteristic for liquids and other randomly oriented systems, e.g. amorphous solids. Define

$$\rho = \frac{I_{HV}}{I_{VV}} \tag{3.3}$$

where V denotes light plane-polarized perpendicular to the scattering plane, and H is for light polarized in the scattering plane [Loudon, p.112]. Thus, I_{HV}, for example, is the Raman-scattering intensity measured when incident light is polarized parallel to the scattering plane, and scattered light is analyzed perpendicular to the scattering

plane. For randomly oriented scatterers

$$0 \leq \rho \leq 3/4 \qquad (3.4)$$

for which the maximum (completely depolarized) occurs when the trace of the Raman tensor matrix is zero (all symmetries except Γ_1 in Table 1.3), and the minimum occurs when the diagonal elements of the Raman tensor matrix are identical and the off-diagonal elements are zero (Γ_1 in Table 1.3). Thus, the only hard deductions which may be made from $\rho(\omega)$ is whether the vibration participating in the Raman scattering has Γ_1 symmetry or not. However, it is a spectroscopic fingerprint which may be used for identification purposes.

Polarization analyses of the flash evaporated a-GaAs are shown in Fig. 3.9. The a-GaAs spectra all have three primary bands with band maxima near 70, 150, and 250 cm^{-1}. For the 250 cm^{-1} band, where parasitic scattering is negligible, the depolarization ratios were measured for the three samples whose Raman spectra are shown in Fig. 3.8. Zero intensity was taken at 350 cm^{-1}. Because light is not incident normal to the specimen, differences in transmission were accounted for between light plane-polarized in and normal to the scattering plane [Jackson, p.281]. For a refractive index of 4.3 near 2.41

eV [Theeten & Erman], and an incident angle of ~ 40° (outside the sample), transmission differs by a factor $T_H/T_V \approx 1.2$. The depolarization ratios at 250 cm^{-1} were found to be 0.69, 0.69, and 0.70 (all ± 10%) for flash evaporated, sputtered, and ion-damaged amorphous GaAs, respectively.

These values may be considered identical to this precision. The entire depolarization spectrum (20 to 300 cm^{-1}), generated using full spectra like those in Fig. 3.9, were in excellent agreement for the flash evaporated and ion-implanted a-GaAs , rising from ~ 0.55 at 70 cm^{-1} to ~ 0.70 at 250 cm^{-1}. The sputtered a-GaAs had a lower value at 70 cm^{-1}, $\rho \approx 0.46$, possibly due to the slightly higher parasitic scattering from this specimen. Since Rayleigh scattering does not alter the light polarization, the HV will discriminate against the laser reflection and the VV will not. This effect is clear in the low-frequency region of the spectra in Fig. 3.9.

When a microcrystalline LO signal is still observed (even for very heavily damaged GaAs), it retains its full single-crystal (100) selection rules (as in Table 1.4). Thus, these very small remnants have retained their pre-implant orientation. By orienting the ion-implant

amorphized GaAs for $z(x,y)\bar{z}$ = HV scattering, with the x and y axes defined in the crystal before implanting, the LO is

allowed and the a-GaAs is weaker. The LO is still not observed under these conditions. The ion-implant a-GaAs depolarization ratio is invariant under rotation of the sample about the norm, just like the conventionally prepared a-GaAs, indicating no appreciation for its origins.

From this evidence it is concluded that these three forms of a-GaAs are essentially identical. Ion damage then leads to a-GaAs, a point which has been commonly asserted in ion-implantation literature without conclusive supportive evidence.

3.3 A QUANTITATIVE DISCUSSION OF THE COMPOSITION OF THE RAMAN SPECTRA

An important assertion which may now be made is that the three-band continuum observed in the Raman spectrum of ion-implanted, but not amorphized, GaAs (Figs. 3.1 - 3.6) is due to regions of the damaged layer which have been converted to a-GaAs by the ion damage "track" as it passes through the crystal, colliding with the target atoms.

The picture which emerges of the ion damaged surface layer is one of a mixture of GaAs crystallites and pockets of a-GaAs. For very high damage the crystallites are rendered completely amorphous ($\ell \rightarrow 0$). The volume fractions of the surface layer which are amorphous/

crystalline, and the distribution of sizes of the crystallites, depend upon the implant conditions. Higher proportions of a-GaAs are synonymous with smaller crystallites, for a given ion mass and energy.

In Fig. 3.10 one form of amorphous/microcrystalline comparison is presented. The fraction of the reduced Raman spectrum ($g_b(\omega)$ in Eq.(1.13), assuming C_b constant) which is amorphous (i.e. component integrated intensities), ϕ_a, is shown for several ion species and energies: 45-keV Be^+ (Be symbol); 120-, 150-, and 180-keV Si^+ (S1, S2, and S3, respectively); and 120-keV SiF_3^+ (SF).

For a crystal, ϕ_a is of course zero. For the fully amorphized 1 and 2 x 10^{14} cm^{-2} SiF_3^+ implant the spectrum is completely amorphous ($\phi_a = 1$). Below the amorphization fluence ϕ_a steadily rises. If the average slope of ϕ_a (linear scale) can be interpreted as the volume amorphized by each ion per unit length, then the SiF_3^+ ions amorphize the crystal at a rate of ~ 12 A^2/ion between 6 x 10^{12} and 10^{14} cm^{-2} fluences. For cylindrical damage tracks this corresponds to a track diameter of 4 A/ion (recall a_o = 5.64 A).

It is noteworthy that after an implant exceeding 4 x 10^{14} cm^{-2} with 120-keV SiF_3^+ ions, the crystalline LO line is revived (as indicated in Fig. 3.10 by a decrease in ϕ_a). This situation is also observed in the 120-keV Si^+

implants as well (data not shown). The reason for this recrystallization is that some of the incident ion energy is released as heat (electron-ion scattering and atom-ion scattering with insufficient energy transfer to break the Ga-As bonds). When this heat raises the temperature, the implant process itself causes annealing of the implanted layer. This so-called "self annealing" process [Geissberger et al.] shall not be investigated in any detail here.

Also plotted on Fig. 3.10 is a single point labeled 5X at $\phi_a = 1$, fluence = 10^{15} cm^{-2}. This is for the five consecutive implants of 120-keV SiF_3^+, each to a fluence of 2×10^{14} cm^{-2}, with exposure to air between each to return it to room temperature. The Raman spectrum has been shown in Fig. 3.8. For implant fluences below the self-annealing threshhold the ion damage is cumulative (unless already amorphized). For room temperature targets it is therefore possible to avoid self-annealing and reach higher stages of damage using multiple, below-threshhold implants.

For the 120- and 150-keV Si^+ ion implants, the data in Fig. 3.10 show good agreement. Between 6×10^{12} and 10^{14} cm^{-2} the rate of amorphization is ~ 35 A^2/ion, or a track diameter of 7 A/ion. Both saturate near 10^{14} cm^{-2}, even though $\phi_a \approx 0.85$.

The 45-keV Be^+ data (Be) in Fig. 3.10 are interesting. These data favor a curve with decreasing slope. For the 10^{13} to 10^{14} cm^{-2} fluence range the curve has a slope ~ 42 A^2/ion (D ≈ 7 A/ion). Between 5 x 10^{13} and 5 x 10^{14} cm^{-2} the slope is closer to 5 A^2/ion (D ≈ 3 A/ion). The 3 A/ion estimate is in quite good agreement with independent estimates from actual amorphous volume fractions discussed in Chapter 4.

The decrease in the rate at which c-GaAs is converted to a-GaAs is viewed as a combination of two effects: (1) With increasing temperature the amorphization <u>efficiency</u> of each ion decreases (the lattice does not quench the damage, but helps it to recrystallize), (2) The probability of an ion striking a microcrystal decreases with higher amorphous volume fractions and smaller crystallites (discussed further in Chapter 4).

Each of the various slopes associated with the data in Fig. 3.10 is in some manner a measure of the amorphization efficiency of a given ion, which itself depends on the fluence. Data for the 120- and 150-keV Si^+ ions show a much larger slope than the 180-keV Si^+ (track diameters of 7, 7, and 1 A/ion, respectively). This is not accounted for by the differences in the nuclear scattering cross-sections ($\sigma \sim E^{1/2}$) [Schiff, p.105]. The 180-keV Si^+ implants are therfore considered to be close to the

saturation levels, even at a fluence of 2×10^{13} cm^{-2}, making the damage track seem disproportionately low.

It is interesting to note that the bare Si^+ ion possesses a larger track diameter than the SiF_3^+ ions (D = 7 A as compared to 4 A). These two are difficult to compare. It is expected that upon collision with the target atoms the SiF_3^+ ions break up into a Si and three F atoms. The resulting kinetic energies (assuming negligible loss during break-up) are ~ 40 keV for Si and ~ 27 keV for each F atom. In this scenario, the ion fluence must also be considered to be higher. For fluences of four times the SiF_3^+ unit-ion fluences, the track diameter (average) is closer to 3 A/ion, comparable to the Be^+ ion track diameter.

This analysis is carried out only to show that there is consistency within the data. Of course, actual values are only <u>estimates</u>. The important point is that ion implantation damages GaAs in a similar manner, independent of ion species and energy. The damage is well-characterized as a mixed amorphous/ microcrystalline system. The fact that the SiF_3^+ ion dissociation makes sense is important, and shall be used in the context of non-destructive damage depth profiling in Chapter 5.

TABLE 3.1: LO Shift and Line Width For Various Implants in GaAs

Implant Type	Fluence (cm^{-2})	LO Shift (cm^{-1})	LO FWHM (cm^{-1})	$\langle \ell \rangle$ (A)
45-keV Be^+	1×10^{13}	0.0	3.0	∞
	5×10^{13}	- 0.7	5.0	180
	1×10^{14}	- 1.8	6.3	85
	5×10^{14}	- 3.3	7.8	55
180-keV Be^+	5×10^{14}	- 3.0	7.5	60
120-keV Si^+	6×10^{12}	- 1.0	5.0	100
	2×10^{13}	- 2.0	7.5	75
	2×10^{14}	- 5.0	10.0	50
	3×10^{15}	- 4.5	10.0	50
150-keV Si^+	1×10^{13}	- 2.0	6.0	80
	5×10^{13}	- 5.0	10.0	50
	1×10^{14}	- 5.5	10.0	40
180-keV Si^+	2×10^{13}	- 2.5	8.0	70
	1×10^{14}	- 5.0	9.0	50
	5×10^{14}	- 4.8	11.5	45
120-keV SiF_3^+	6×10^{12}	- 2.0	8.5	75
	1×10^{13}	- 2.5	9.0	65
	4×10^{13}	- 5.0	10.0	50
	2×10^{14}	no LO		"0"

FIGURE CAPTIONS

Fig. 3.1 : Raman spectra for the 45-keV Be^+ fluence sequence studied. Fluences shown are measured in ions/cm^2. 5145-A excitation.

Fig. 3.2 : Raman spectrum of 5 x 10^{14}-cm^{-2} 180-keV Be^+ implanted GaAs. 5145-A excitation.

Fig. 3.3 : 120-keV Si^+ implant fluence sequence. 5145-A source.

Fig. 3.4 : 150-keV Si^+ fluence sequence. λ_L = 5145 A.

Fig. 3.5 : 180-keV Si^+ implant fluence sequence. 5145-A excitation.

Fig. 3.6 : 120-keV SiF_3^+ implant fluence sequence. By 2 x 10^{14} cm^{-2} the spectrum is the same as amorphous GaAs spectra. 5145-A source.

Fig. 3.7 : Comparison of the spatial-correlation model [Tiong et al.] to the experimental results of Figs. 3.1 - 3.6. Error bars show typical precision. λ_L = 5145 A.

Fig. 3.8 : Raman spectra for a-GaAs prepared using three different techniques. 4579-A (2.71-eV) source.

Fig. 3.9 : Polarization breakdown of the flash-evaporated

a-GaAs film. The intensities are plotted arbitrarily; $I_{HV}/I_{VV} \approx 0.7$ at 250 cm^{-1}, as discussed in the text, is the measured ratio. λ_L = 5145 A.

Fig. 3.10: Fraction of the (reduced) Raman spectrum, which is from the a-GaAs component, versus fluence for several implanted ion species. 5145-A source was used throughout.

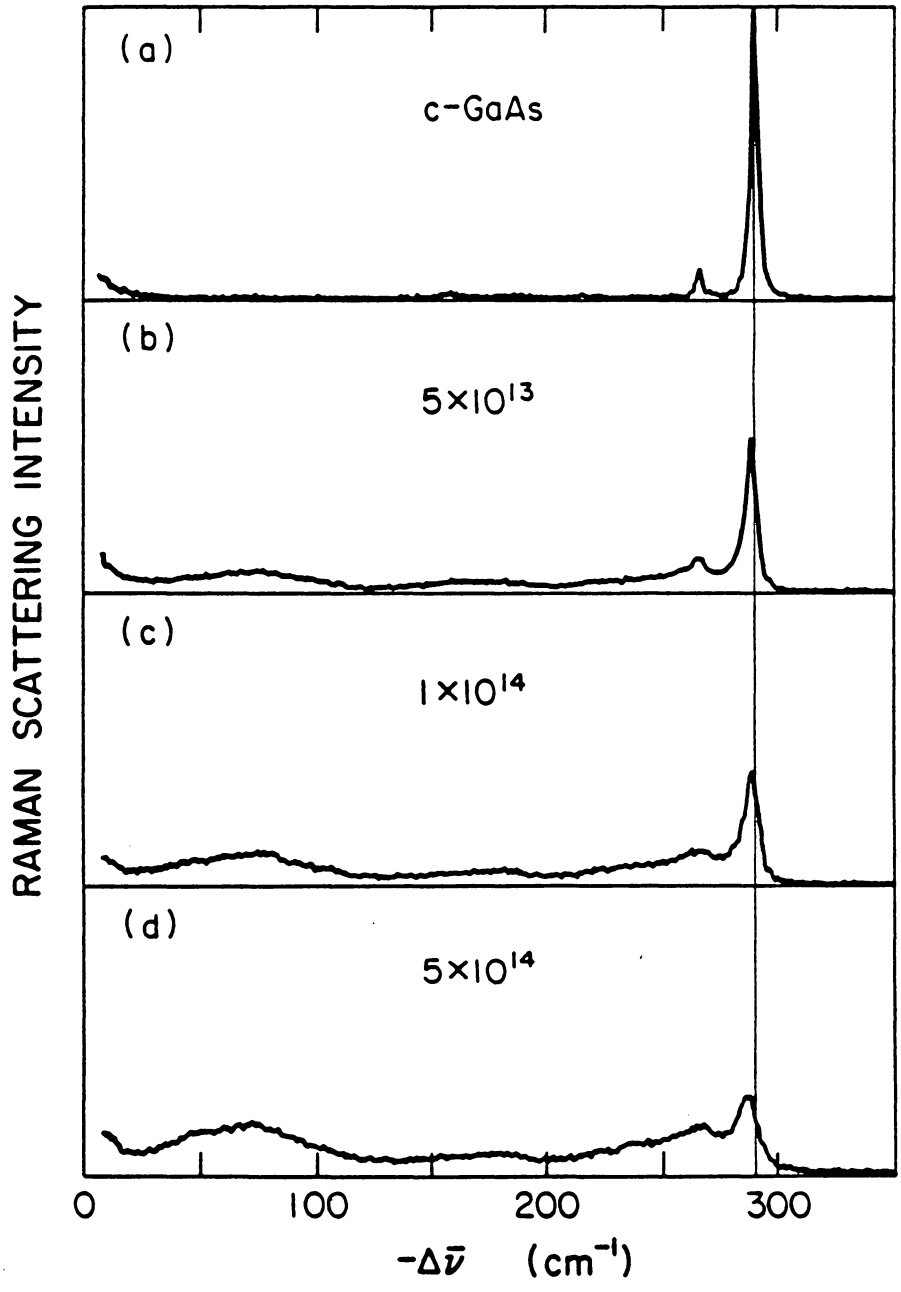

Fig. 3.1 45-keV Be^+ implant sequence.

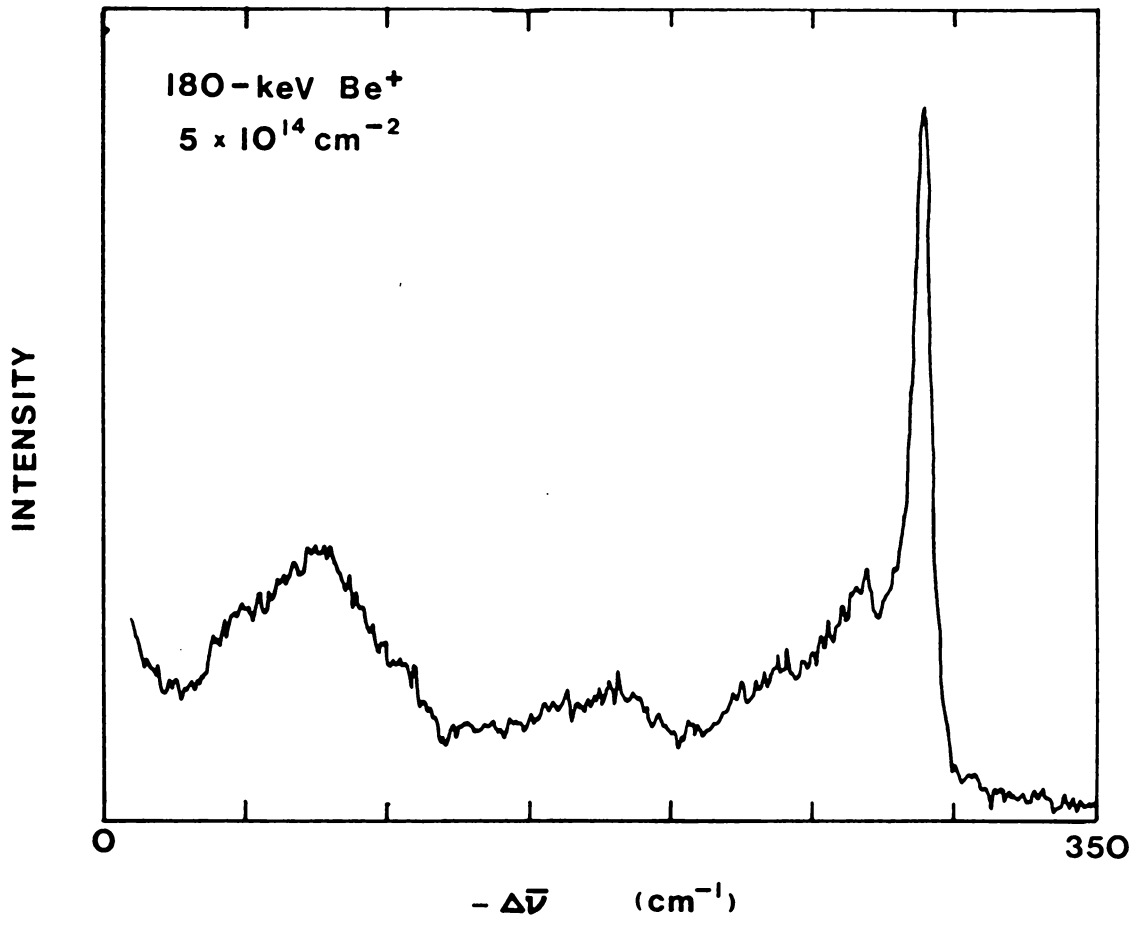

Fig. 3.2 180-keV Be^+ implant, 5 x 10^{14} cm^{-2}.

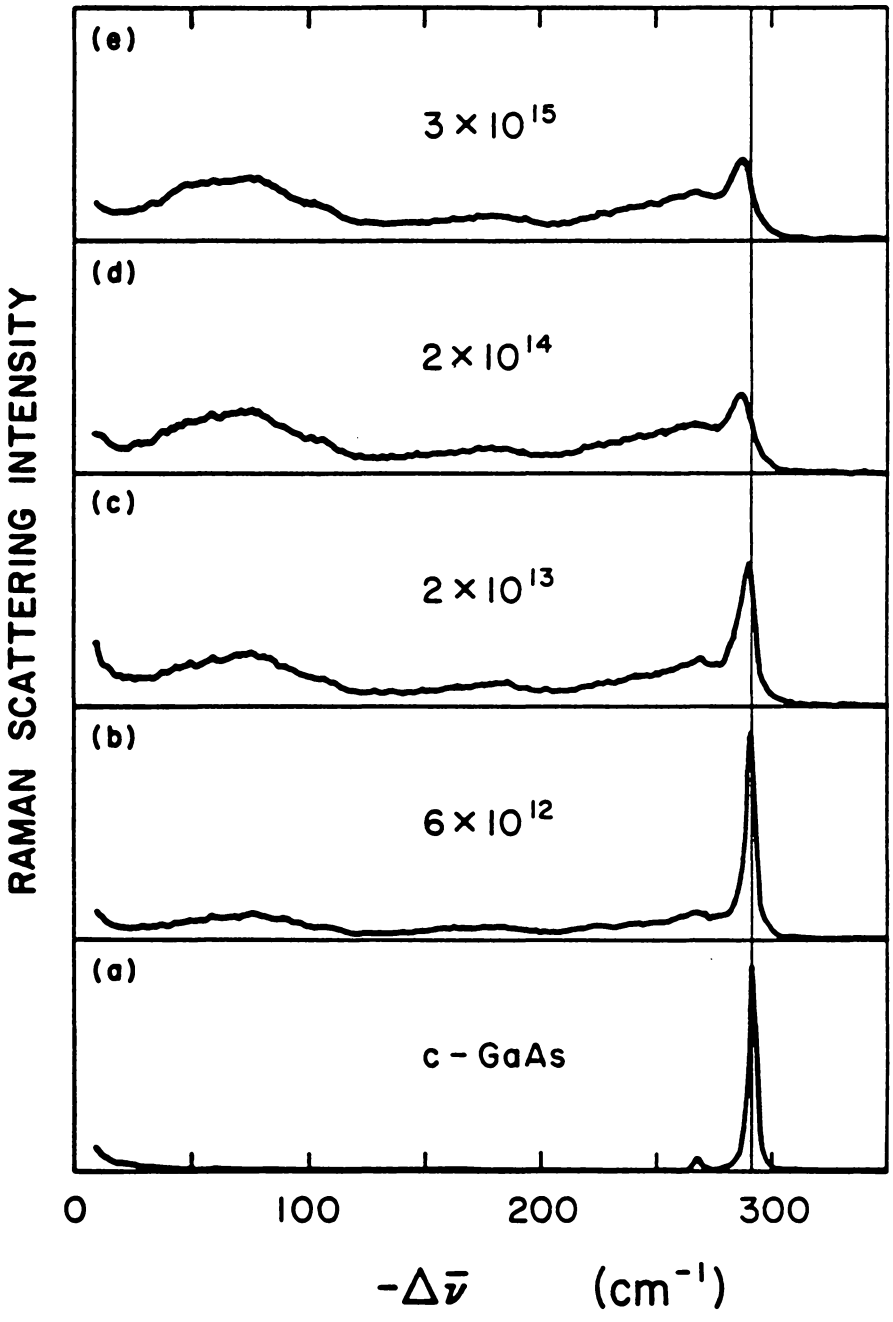

Fig. 3.3 120-keV Si^+ implant sequence.

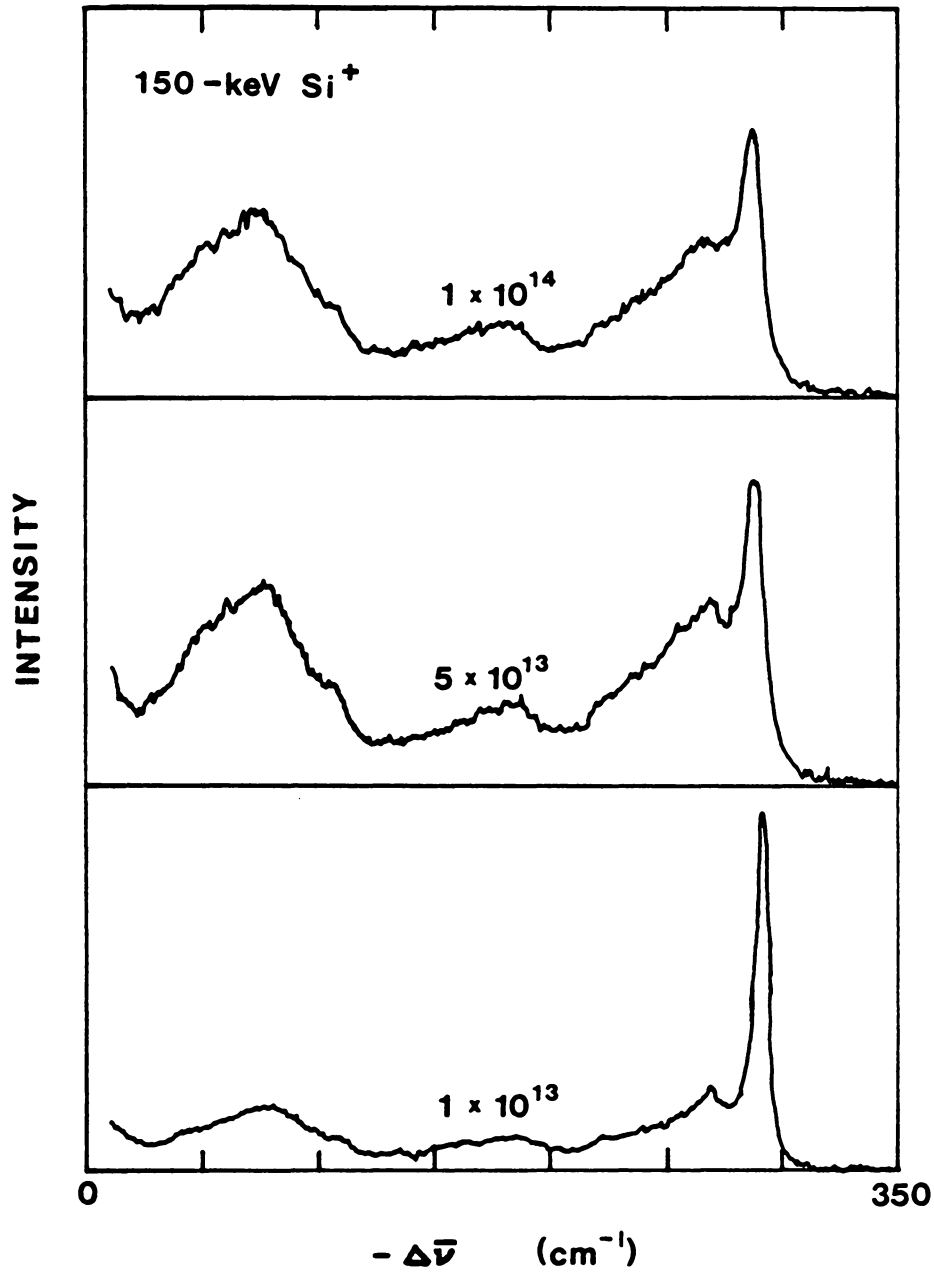

Fig. 3.4 150-keV Si^+ implant sequence.

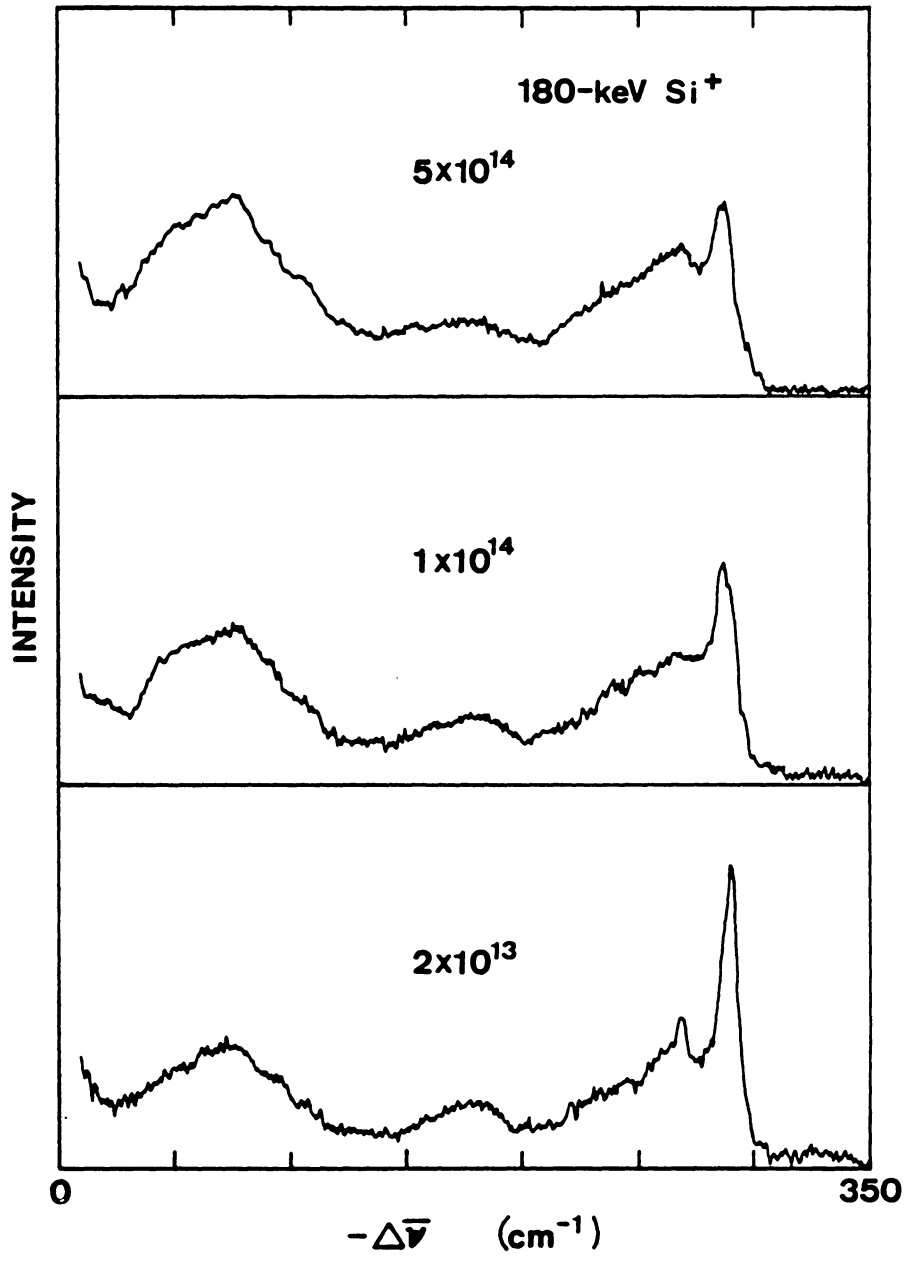

Fig. 3.5 180-keV Si^+ implant sequence.

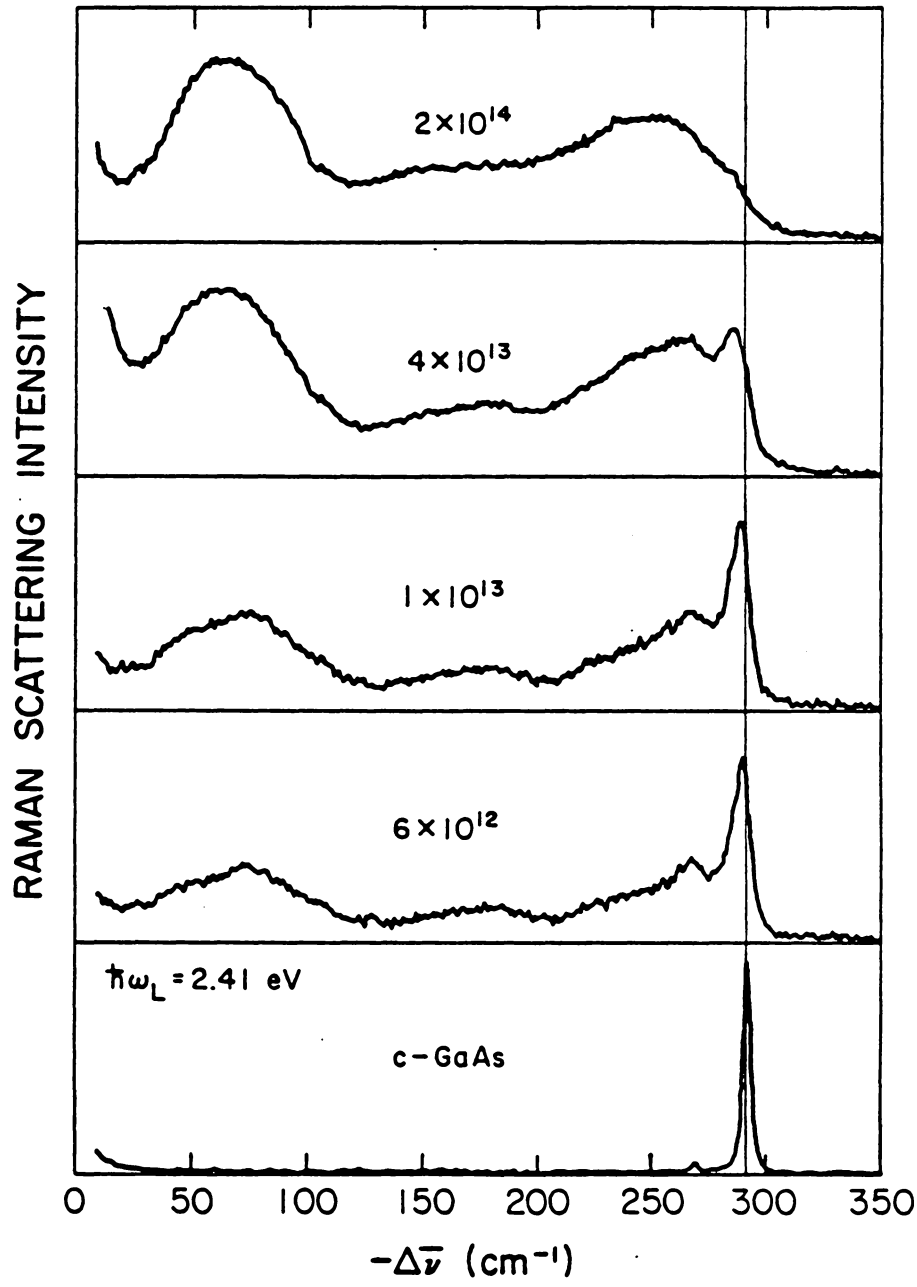

Fig. 3.6 120-keV SiF_3^+ implant sequence.

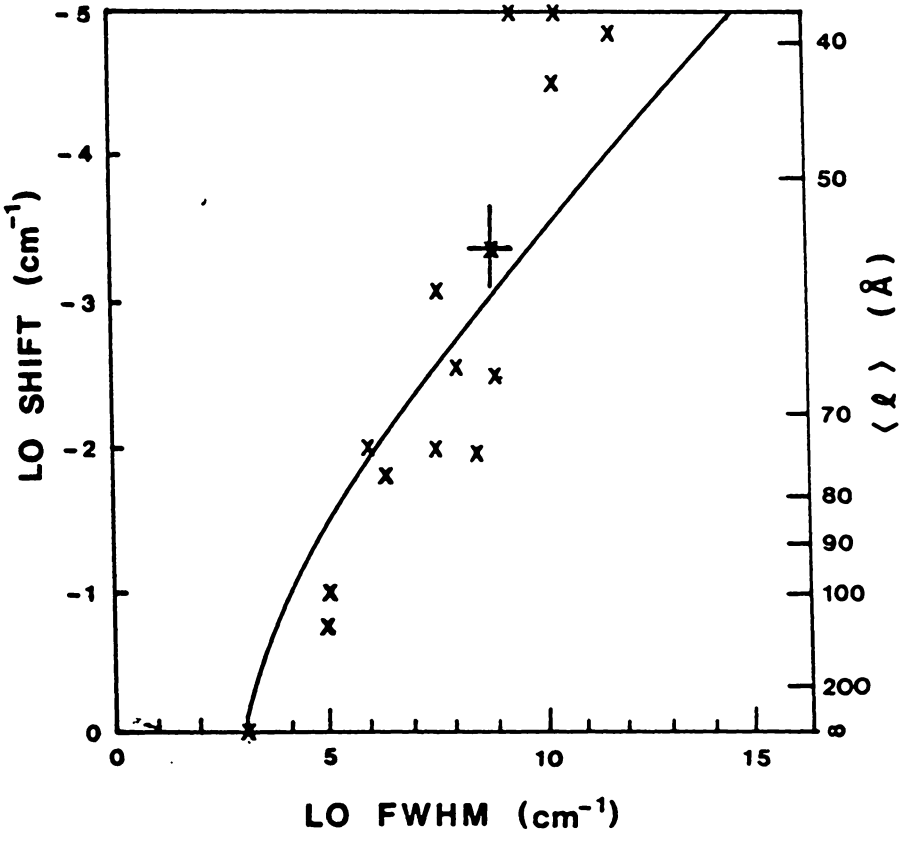

Fig. 3.7 LO phonon line shape vs. theory [Tiong et al.].

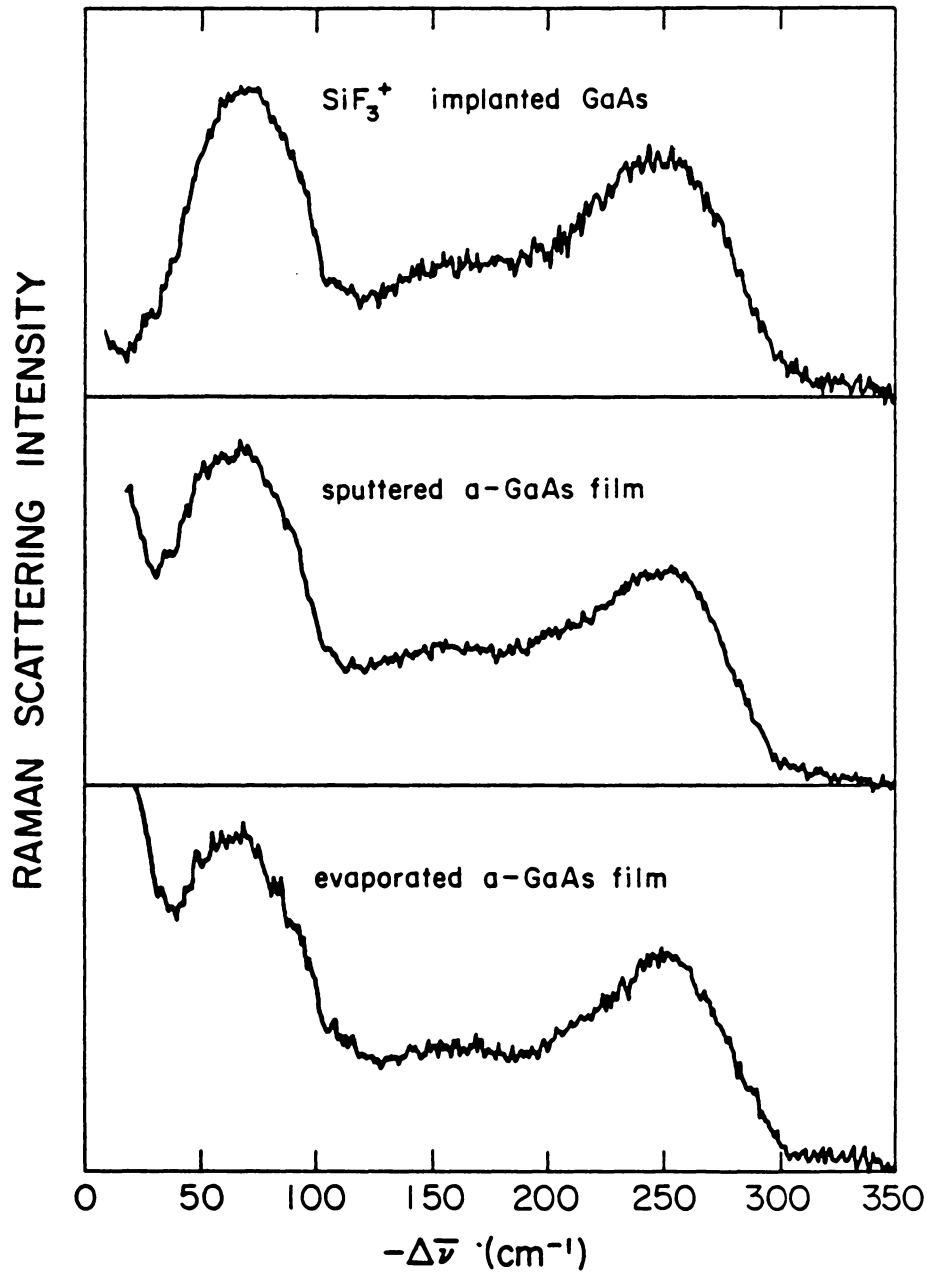

Fig. 3.8 Comparison of three a-GaAs specimens.

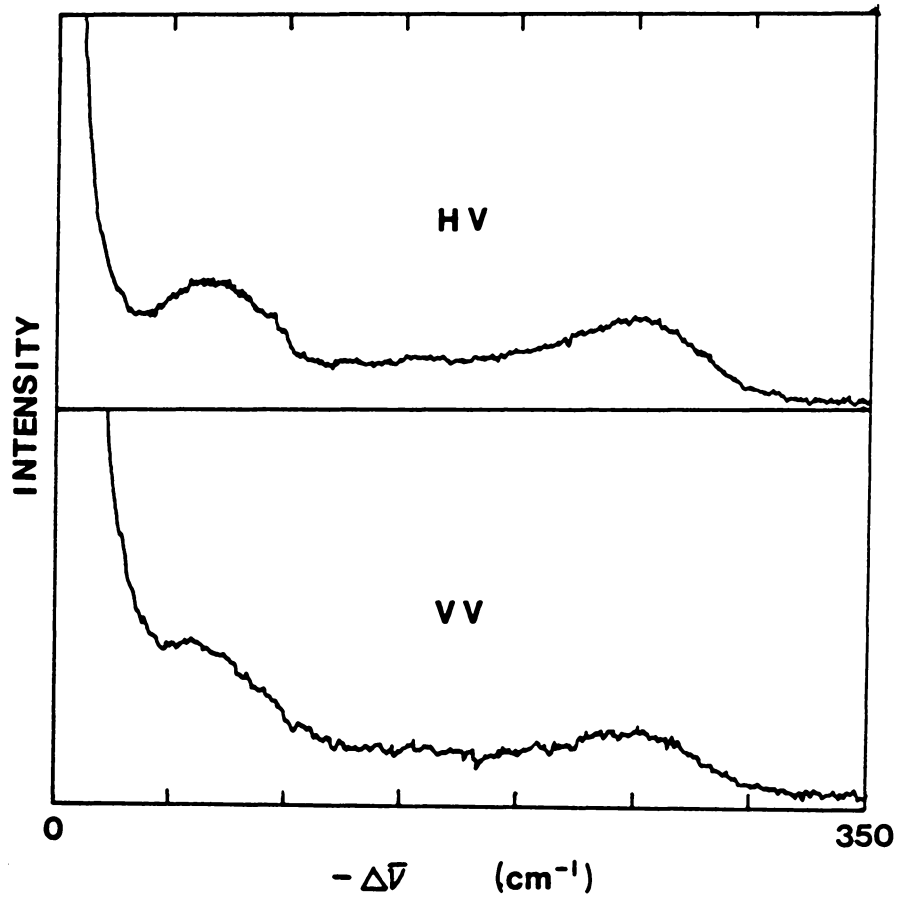

Fig. 3.9 Polarization breakdown of a-GaAs.

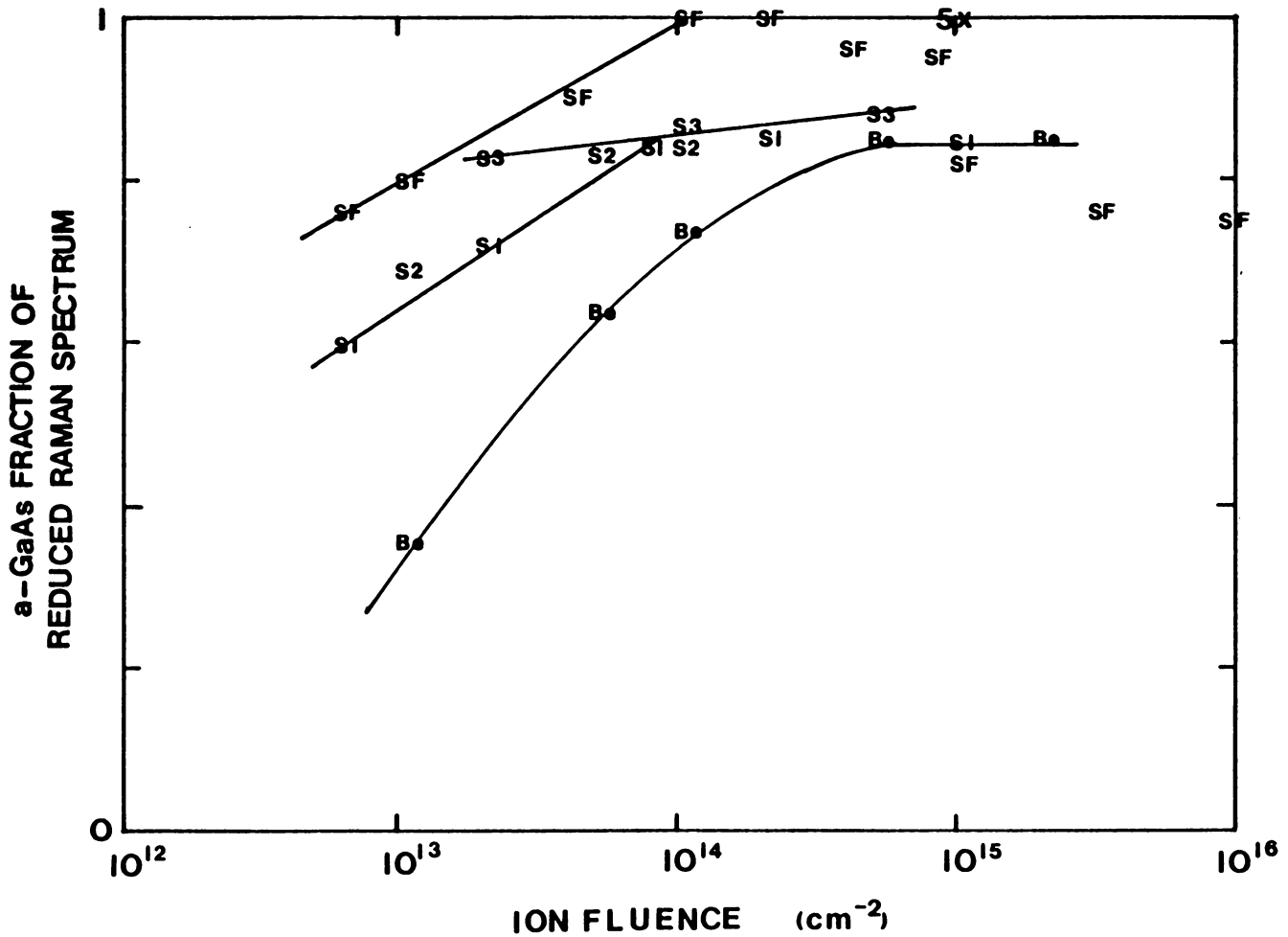

Fig. 3.10 Fluence dependence of the amorphous component.

CHAPTER 4: RAMAN SCATTERING DEPTH PROFILE OF THE STRUCTURE OF Be^+-IMPLANTED GaAs

4.1 INTRODUCTORY REMARKS

In this chapter we report the results of an extensive Raman-scattering investigation of the structure of the damage layer that is produced in GaAs by bombardment with Be^+ ions (common p-type dopant). Depth profiles of the structural character of the implanted layer were obtained by analyzing the spectral changes which occur as a function of both chemical etch time and laser photon energy. The observed spectral changes are interpreted in terms of a depth-dependent crystalline/amorphous mix and crystallite size distribution; these Raman-derived profiles constitute the structural information which is our main focus. Information is also obtained about the optical absorption in partially amorphized GaAs. In addition, we have observed damage-dependent resonance-Raman effects; these are attributed to the influence of crystallite size.

The etching was carried out as described in Ch. 2. The calibration of the etch rate is shown in Fig. 2.1. Essential to the following analysis is the intensity reference, also described in Ch. 2, from which two independent spectroscopic quantities (intensity and line shape) are used to generate consistent results for the

degree of damage. The evidence presented here strongly supports the amorphous/crystalline mixed phase assumption, discussed in Ch. 3. Fig. 4.1 is the same as Fig. 3.1, repeated here for easy comparison.

4.2 DAMAGE LAYER DEPTH PROFILE

Figure 4.1 shows full first-order Raman spectra of (100) GaAs before implanting and following various implants of 45-keV Be^+ ions. Here Stokes Raman-scattering intensity is plotted versus frequency shift $-\Delta\bar{\nu}$ in wavenumber units ($1/\lambda$ in cm^{-1}) from the laser frequency. The spectra of Fig. 4.1 (as well as those of Figs. 4.2 and 4.3) were obtained using the argon green line: λ_L = 5145 A, $\hbar\omega_L$ = 2.41 eV. The intensity scales for all of the curves presented on a given figure have the same normalization with respect to the CaF_2 standard.

The crystal spectrum at the top of Fig. 4.1 exhibits a strong LO line at 291 cm^{-1}, accompanied by a weak TO line at 268 cm^{-1}. Although the TO is forbidden in backscattering along (100), we observe it here because we are not in a strict backscattering geometry and because the scattered light is collected in a cone about (100). With increasing fluence, the LO line is seen to decrease in intensity, downshift in energy, and broaden in linewidth. This is due to the implantation-induced change in the

crystalline portion from the bulk crystal to a collection of crystallites. A decrease in crystallite size limits the correlation length ℓ of the optical phonon and thereby replaces the strict $k = 0$ crystal selection rule with a more permissive range ($\Delta k \sim 1/\ell$) of LO phonon k values [Richter et al.].

Also evident in Fig. 4.1 are additional low-energy bands which increase in intensity with higher fluence. These broad bands comprise the Raman signature of amorphous GaAs [Tiong et al., Nakamura & Katoda, Zallen et al., Abels et al.]. Implanting, then, produces a near-surface damage region which consists of an amorphous/ microcrystalline mixture. The simultaneous appearance of spectral signatures of both the crystalline form (LO line, albeit shifted and broadened) and the amorphous form (three-band continuum from 0 to 300 cm^{-1}) supports this picture.

In Fig. 4.2 we show detailed spectra of the LO region for the same set of implants as in Fig. 4.1. From these spectra we obtain LO intensities, frequency shifts, and linewidths which can then be used to quantify the implant damage. In generating such values correctly, it was found to be important to subtract the amorphous contribution to the Raman spectrum in the LO region, especially for higher doses, as is evident in Fig. 4.1. To

do so, the full spectrum (20 - 300 cm^{-1}) was collected and the spectrum of amorphous GaAs (Ch. 3) [Theye & Gheorghiu] was subtracted after appropriate scaling. Without this correction for the amorphous contribution, the LO frequency would be overestimated and its low-frequency wing would be too large.

The variation with etch time of the LO spectrum (raw data) is shown in Fig. 4.3 for the 5 x 10^{14} cm^{-2} implant. The spectra for zero, one, and two minutes of etch (corresponding to etch depths of 0, 660, and 1320 A) are identical in all respects (in fact, the full spectra are identical), indicating that the level of damage is constant in this region. After 2000 A have been etched away, the LO line begins to narrow while shifting toward higher frequency and growing in intensity, indicating less damage. By 3500 - 4000 A the spectrum is that of the pristine crystal, indicating that the full damage layer has been etched away to expose the undamaged crystalline substrate.

The similarity of the curves for etch times of 0, 1, and 2 minutes shows that the optical penetration depth d_{OPT} is smaller than the depth corresponding to one minute of etch (d_{OPT} < 660 A). In the present context, in which the scattered light must return along the same sample length as that penetrated by the laser light, d_{OPT} is taken

to be $1/(2\alpha)$, where α is the optical absorption coefficient. At 2.41 eV, d_{OPT} is 550 A in crystalline GaAs [Aspnes & Studna] and about 140 A in amorphous GaAs [Theeten & Erman], values consistent with our finding that $d_{OPT} < 660$ A in the mixed phase.

Etch profiles like those in Fig. 4.3 for 5×10^{14} cm^{-2} were obtained for 5×10^{13} and 1×10^{14} cm^{-2} implants under identical conditions. All of these results are summarized in Figs. 4.4, 4.5, and 4.6. Figure 4.4 displays the shift in the peak position of the LO line ($\bar{\nu}_{LO}$(damaged) - $\Delta\bar{\nu}_{LO}$(crystal)) as a function of etch depth. Figure 4.5 shows the LO linewidth (corrected for instrument resolution) versus depth, with the crystalline linewidth at 3.2 cm^{-1}. Relating these results to average microcrystallite size (right hand border of Fig. 4.4) using the analysis of Tiong et al., we find consistency between Figs. 4.4 and 4.5 and their results. Figures 4.4 and 4.5 can thus be used to estimate a characteristic crystallite size as a function of depth, and this will be done below. Several main features are already clear at this point. Our experiments reveal a total damage- layer depth (for 45-keV Be^+ implants) of about 4000 A, and a high-damage plateau region of constant high damage extending from the surface to a depth of about 1500 A. The amplitude of the damage profile naturally increases with

increasing fluence, but the depth-dependent shape is insensitive to fluence.

Figure 4.6 presents the LO integrated intensity observed as a function of etch depth for each of the same three fluences. These measurements of absolute Raman-scattering intensities are difficult; they rely upon repeated sample substitutions and comparisons to the CaF_2 standard. The appreciable scatter is therefore not surprising. However, the pattern is quite clear and is consistent with Figs. 4.4 and 4.5. Specifically, the total depth of damage is the same for all three fluences (of course, the degree of damage increases with fluence), and all three implants exhibit a similar near-surface high damage plateau region. Within the high-damage plateau, the LO intensity is small because the fraction of the scattering volume which is still crystalline is small and because the penetration depth is also reduced.

The curves in Figs. 4.4 and 4.5 are simply smooth representations of the data points, unlike the curves in Fig. 4.6 which are the results of theoretical calculations based on a simple model of the damage layer. Since we expect the optical properties to vary with the crystalline/amorphous mix, which in turn varies with depth, the measured intensity of the crystalline component of the spectrum (i.e., the LO integrated intensity) is related to

the volume probed by

$$I_c \sim \int_0^{\infty} dx\, f_c(x)\, e^{-2\int_0^{x} \alpha(x')dx'} \qquad (4.1)$$

where x (x') is the depth from the surface, $f_c(x)$ is the crystalline volume fraction at depth x, and $\alpha(x)$ is the optical absorption coefficient at x. The factor of two in the exponent arises from attenuation of the laser light traveling a distance x into the material, and attenuation of the scattered light as it travels back out distance x. Differences between the crystalline and damaged GaAs reflectances were found to be small, a point which we will return to. We assume the same α for the scattered light as the laser beam (the two photon energies differ by only one percent), and we assume that losses due to Raman scattering are small compared to optical absorption. The sample thickness is taken as infinite compared to d_{OPT}.

Equation (4.1) is a generalization of the homogeneous, opaque case, for which $I \sim d_{OPT} = 1/(2\alpha)$, to inhomogeneous systems of varying microstructure and optical absorption. Our view of the implanted layer as a mixed crystalline/amorphous system requires that

$$\alpha = f_c\, \alpha_c + f_a\, \alpha_a \qquad (4.2)$$

where α_c and α_a are, respectively, the absorption coefficients of the crystalline and amorphous components, and f_a (= 1 - f_c) is the amorphous volume fraction. Thus, Eq. (4.2) becomes

$$\alpha(x) = f_c(x)\,\alpha_c + (\,1 - f_c(x)\,)\,\alpha_a \qquad (4.3)$$

and Eq. (4.1) depends only on $f_c(x)$ since α_c and α_a are known. The curves in Fig. 4.6 are generated from Eq.(4.1) using

$$f_c = \begin{cases} f_c(0) & ;\ 0 - 1600\ \text{A} \\ f_c(0) + [\,1 - f_c(0)\,]\dfrac{x - 1600\ \text{A}}{2600\ \text{A}} & ;\ 1600 - 4200\ \text{A} \\ 1 & ;\ \geq 4200\ \text{A} \end{cases} \qquad (4.4)$$

where the portion linear in x is a continuous interpolation from the end of the high-damage plateau (throughout which $f_c = f_c(0)$, the near-surface value) to the start of the undamaged substrate (f_c = 1). The dependence of I_c then follows from Eq. (4.1) by progressively moving the assumed front surface deeper into the damage layer.

The three different curves of Fig. 4.6 correspond to three choices for $f_c(0)$. All were normalized at a depth of 5000 A to agree with the crystalline intensity. The

simplest model (linear interpolation) for the transition region between the plateau and the pristine crystal was used; other depth dependences were considered, but the exact nature of Eq. (4.1) was not sensitive to the details of $f_c(x)$. As expressed in Eq. (4.4), 4200 A was used for the total damage depth and the plateau depth was 1600 A.

In evaluating Eq. (4.1) for Fig. 4.6 we have neglected small changes in reflectance (R) between damaged, etched, and crystalline samples (the etching itself results in higher surface reflectance, possibly due to the formation of surface oxides), or changes in scattering volume due to variations in the refractive index (n). This was justified by estimates of R and n obtained by means of the effective medium approximation [Aspnes, 1984]. Dielectric function values were taken from Aspnes & Studna (crystal), and Theeten & Erman and Aspnes [private comm.] (amorphous). (Absorption coefficients generated in this manner are in good agreement with Eq.(4.3).) Changes in R and n, over the range of f_c considered, were found to yield negligible corrections.

The values of $f_c(0)$ used to generate the curves in Fig. 4.6 were 0.93, 0.88, and 0.75 for 5×10^{13}, 1×10^{14}, and 5×10^{14} cm^{-2}, respectively. These values indicate that, even in the high-fluence implants, the sample remains predominantly crystalline although the average crystallites

are quite small (75% crystallinity in the plateau, with 60 A crystallites, at 5 x 10^{14} cm^{-2}).

Suppose we assume that each ion produces a cylindrical damage track of diameter D, in which amorphization occurs. Then, for fluence F, the statistical result for $f_c(0)$ is just exp(- FA), where $A = \pi D^2/4$. (This is the uncovered fraction of a plane upon which overlappable disks of area A are randomly placed with density F.) Using, for each F, the value of $f_c(0)$ obtained from the analysis of Fig. 4.6, this expression implies D values of 4.3 A, 4.0 A, and 2.7 A for the three fluences. While these are only modestly consistent with each other, a result of 4 A for the damage track diameter is reasonable in view of the lightness of the Be^+ ion. For As^+ implanted into GaAs, Aspnes et al. [1982] estimated a track diameter upper limit of 10 A.

Figure 4.7 displays our Raman-derived experimental results for the structural depth profile of the damage layer in implanted GaAs, for the case of 45-keV Be^+ (5 x 10^{14} cm^{-2} results are shown). Data points symbolized by filled-in circles are reciprocal crystallite sizes obtained from the peak and linewidth results of Figs. 4.4 and 4.5. Those represented by an x are direct amorphous intensities (relative to CaF_2) taken from full spectra (20 - 300 cm^{-1}) and scaled to agree with the other results in Fig. 4.7.

The heavy trapezoidal line is the amorphous fraction $1 - f_c(x)$ which corresponds to the model used (Eq. (4.4)) to generate the fit to the intensity data of Fig. 4.6. The overall agreement of these three measures of implantation-induced disorder is very satisfactory and supports the mixed amorphous/microcrystalline model for the structure of the damage layer. These measures reveal a high-damage near-surface plateau which extends to a depth that is about a third of the full depth.

The picture which emerges of the near-surface damage layer is a region of constant average crystallite size and constant crystalline volume fraction coexisting with amorphous GaAs within a fine-scale two-phase matrix. This high damage region extends approximately 1500 A from the surface for 45-keV beryllium implants. A transition region follows in which f_c and crystallite size grow steadily until the underlying single crystal is reached at approximately 4000 A.

Figure 4.7 also includes, for comparison to the experimental results, two widely-used theoretical estimates of damage profiles (shown for the case of 45-keV Be^+ into GaAs): LSS [Carter & Grant] and TRIM [Ziegler et al.] ("transfer of ions in matter," a Monte Carlo calculation of the displaced atoms). These are included as the curves in Fig. 4.7. The broad maximum in the TRIM calculation

agrees fairly well with the extent of the high-damage plateau revealed by our experiments. The LSS maximum occurs near the center of the observed damage plateau. Both calculations underestimate the full depth of the damage. A dip in the damage density is predicted at the surface by both calculations, but it is not observed experimentally. This is not an artifact of the finite optical penetration depth. We also depth profiled with the 4579 A laser line, which has a penetration depth of only 260 A in crystalline GaAs [Aspnes & Studna] and only 90 A in amorphous GaAs [Theeten & Erman], both smaller than the etch step. These Raman experiments, which probed a layer substantially thinner than the etch step, yielded the same result: the high-damage plateau extends to the surface.

Christel and Gibbons applied the transport equation approach to 50-keV boron in GaAs. They found a displacement density (As and Ga displacements) which increased toward the surface. Erman et al. depth-profiled, by chemical etching, high-fluence 10-keV Be^+ in GaAs using spectral ellipsometry. They observed a narrow damage plateau region at the surface which was about 40 % amorphous, followed by a monotonic transition region to the crystal. Theeten and Erman used spectral ellipsometry and the effective medium approximation to profile the damage induced by 10-keV B^+ in GaAs. Their results indicated a

high damage density near the surface, although their profile could be interpreted ambiguously. The evidence for a near-surface damage plateau is not restricted to low energy implants. Kwun et al. observed a similar damage profile, via the refractive index, for 250-keV beryllium implants. The presence of a damage plateau (to 9000 A in their case) is not expected by LSS. Also, in our own laboratory, we have observed uniform damage up to at least 4000 A for 180-keV Be^+ implants, as discussed in Ch. 5.

All of this supports the experimental evidence of Figs. 4.3 - 4.7 for a near-surface high-damage plateau region, and it contradicts the predictions of the LSS and TRIM simulations that there is a near-surface decrease in the degree of structural damage. The physical basis for this predicted near-surface dip in the damage comes from the energy dependence of the nuclear scattering cross-section [Schiff]. At the surface the high ion energy results in a small cross-section. As the ion loses energy, the cross-section grows, resulting in heavier damage. Of course, when the ion energy is very low it does not cause damage, even though the cross-section is large. A very shallow dip in the ion damage is reasonable, since the ion must travel at least one mean free path before undergoing a collision (on the average).

The explanation for the inadequacy of the

theoretical simulations, with respect to this point, is not understood and needs to be examined. It is in contrast to the success which these models have in predicting the concentration profile of the implanted dopant atoms [Duncan & Westphal]. It appears that, for the host lattice, the concentration of displaced atoms is not a satisfactory measure of the actual disordered structure that is produced by implantation, and collisions which transfer insufficient energy to break the GaAs bonds must be considered.

4.3 THE EFFECT OF PHOTON ENERGY: ABSORPTION COEFFICIENTS AND MICROCRYSTALLITE REMNANT LO PHONON

Optical penetration depth depends upon photon energy for an opaque semiconductor. Thus the depth probed by Raman scattering may be varied by changing the laser photon energy, $\hbar\omega_L$. This provides the possibility of a nondestructive probe of structural variations. In a simple two-layer material composed of structurally homogeneous layers, a simple superposition of spectra would be seen with the relative intensities of the separate spectral components varying with the depth probed. In our case we have a continuously-graded material, with the additional complication of a spectral component, the crystallite-size-dependent LO line, which has a spectral <u>shape</u> that varies with depth. This makes the deconvolution of

contributions from different depths more difficult. Fortunately, the broad-band continuum, which is the signature of amorphous GaAs, was found to be insensitive to $\hbar\omega_L$, so that this spectral component could be treated as invariant in shape.

In Fig. 4.8 the spectrum in the neighborhood of the LO line, for the 5 x 10^{14} cm^{-2} specimen (no etch), is plotted for laser photon energies of 1.65, 1.83, and 2.71 eV. All intensities are on the same absolute scale (CaF_2 standard), with the zero of intensity at 320 cm^{-1}. These uncorrected spectra are slightly different in shape (when plotted with the same peak height). However, after subtracting the amorphous GaAs contribution to the spectrum, all three lineshapes are identical, which means that the same distribution of crystallite sizes is being probed. Thus, the range of the probe does not extend beyond the high-damage plateau for these photon energies. The differences in intensity are then a matter of penetration depth and, as discussed below, resonance effects.

For the laser lines with $\hbar\omega_L \geq 1.84$ eV ($\lambda_L \leq 6764$ A), the LO line of the 5 x 10^{14} cm^{-2} implant does not change as etch time changes from 0 to 1 to 2 minutes. Thus, for these wavelengths, the penetration depth d_{OPT} is less than the depth corresponding to one minute of etch

(660 A). However, for 1.65 eV (7525 A) excitation, the LO lineshape observed after one minute of etch time is appreciably different from that observed for the unetched sample. It follows that d_{OPT} at this $\hbar\omega_L$ matches the thickness removed after an etch time of between 2 and 3 minutes. Using this procedure, along with the results of the previous section, and etch-profiling results obtained with other laser lines, it is possible to estimate d_{OPT}, and thereby $\alpha(\hbar\omega) = 1/(2d_{OPT})$, within the damage plateau region. Estimates of α for the 5 x 10^{14} cm^{-2} specimen obtained by this lineshape analysis are (30 ± 5) x 10^3 cm^{-1} (1.65eV) and (80 ± 10) x 10^3 cm^{-1} (1.9 eV). Using Eq. (4.2) with f_c = 0.75 (obtained from LO intensity measurements) we get α = 37 x 10^3 cm^{-1} (1.65 eV) and 70 x 10^3 cm^{-1} (1.9 eV). These estimates are in reasonable agreement with each other. A plot of d_{OPT} using Eq. (4.2) with 75% crystalline volume fraction is shown in Fig. 4.9 as a dashed curve. It is scaled using the 1.65 eV LO intensity value for the 5 x 10^{14} cm^{-2} implant.

Figure 4.9 shows the LO integrated intensity plotted against photon energy (i.e., the <u>excitation spectrum</u> for LO Raman emission) for the pristine crystal and for the implants of 1 and 5 x 10^{14} cm^{-2}. The left side of Fig. 4.9 reveals a strong increase in observed Raman signal at low $\hbar\omega$. Our etch-profile estimates for $d_{OPT}(\hbar\omega)$

reveal that this increase in the LO intensity is well accounted for by the increase in penetration depth (dashed curve) with decreasing photon energy. However, Fig. 4.9 also reveals an increase in intensity at high photon energy. Careful measurements show that this is a real effect, strongest for the crystal and weaker for implanted material. For the crystal, the LO intensity increases by a factor of 1.3 between 2.5 and 2.7 eV, even though the optical penetration depth decreases by a factor of 1.7 over this range. Thus, although the scattering volume is decreasing with increasing $\hbar\omega$, the observed scattering intensity is increasing. We interpret this increase in scattering efficiency as a resonance-Raman effect.

For GaAs, a very strong resonance in the Raman scattering by TO phonons is observed, at room temperature, at 2.9 eV [Grimsditch et al.]. This is the energy of the strong E_1 electronic interband transition absorption peak in GaAs. (The E_0 interband transition at 1.43 eV, the optical bandgap in GaAs, has much smaller oscillator strength and produces only very weak resonance.[28]) We attribute the increasing LO Raman-scattering efficiency with increasing photon energy, as seen in Fig. 4.9 for $\hbar\omega$ above 2.5 eV, to resonance with the approaching E_1 interband transition.

Figure 4.9 shows that the resonance-Raman effect at

high $\hbar\omega$ is substantially diminished by implantation. We believe that this damage-induced quenching of the resonance enhancement is a consequence of the decreasing crystallite size. Decreasing crystallite size broadens the interband peaks in the electronic spectrum [Aspnes et al, 1982], and it is likely that this broadening of the initially sharp crystal peaks is the dominant effect in reducing the resonance. Reflectivity changes are not a factor; at 2.7 eV, the reflectance change caused by implantation is at most a few percent [Erman et al., G.F.Feng private comm.]. Optical penetration depth is decreasing with $\hbar\omega$ throughout this region for both the crystal and the implanted material, more slowly for the latter [Aspnes et al., 1982]. Since $I \sim d_{OPT}$, correcting for $d_{OPT}(\hbar\omega)$ increases both the enhancement effect for the scattering efficiency and the enhancement <u>difference</u> between the crystal and the implanted GaAs.

Resonance-Raman effects in ion-implanted GaAs will be discussed more extensively in Ch. 6. The nature of the LO phonon resonance is explored there in more detail in connection with a new feature in the Raman spectrum of these implanted systems.

FIGURE CAPTIONS

Fig. 4.1: Full Raman spectra (spanning the first-order lattice fundamental regime from 0 to 300 cm^{-1}) for crystalline GaAs and for GaAs implanted with increasing fluences of 45-keV Be^{+}. Each curve is labeled in units of ions/cm^2. These spectra were taken with 5145 A excitation; intensities are normalized to the CaF_2 standard.

Fig. 4.2: Detailed spectra in the vicinity of the crystal LO line, for the same samples in Fig. 4.1. All curves are plotted on the same vertical scale (CaF_2 standard), with the zero intensity (taken at 320 cm^{-1}) displaced for clarity.

Fig. 4.3: LO spectra (5145 A source) of the 5 x 10^{14} cm^{-2} implant for various etch times. By five to six minutes of etch time the spectrum is indistinguishalbe from that of the crystal. All are on the same vertical scale (CaF_2 standard).

Fig. 4.4: LO downshift from the crystalline LO frequency versus etch depth for three fluences: 5 x 10^{13}, 1 x 10^{14}, and 5 x 10^{14} cm^{-2}. The right hand vertical scale is the crystallite size L, associated with the frequency shift on the left,

taken from Ref.(4).

Fig. 4.5: LO linewidth versus etch depth for the same three implant fluences in Fig. 4.4. The crystalline linewidth of 3.2 cm^{-1} is indicated by the horizontal line.

Fig. 4.6: LO intensity (linewidth x peak height), relative to CaF_2, versus etch for the same sequence of fluences and etches as in Figs. 4.4 and 4.5. The source used was 5145 A laser light. The curves were generated using Eqs. 4.1, 4.3, and 4.4, as discussed in the text. Precision can be seen from the repeated data points plotted for 1 x 10^{14} cm^{-2}, no etch.

Fig. 4.7: Experimental results for the structural depth pro- file of ion-implanted GaAs (45-keV Be^+, 5 x 10^{14} cm^{-2} case). The heavy trapezoidal line labeled 1 - $f_c(x)$ is the amorphous volume fraction derived from the model used to fit the LO intensity data Fig. 4.6. The crosses represent amorphous intensities, relative to CaF_2, taken from amorphous bands as in Fig. 4.1. Filled in circles denote reciprocal crystallite sizes obtained from the LO lineshape data of Figs. 4.4 and 4.5. The two curves are

theoretical calculations included for comparison.

Fig. 4.8: The LO spectrum of the 5 x 10^{14} cm^{-2} implant for a wide range of laser photon energies. All are plotted on the same scale, normalized to the CaF_2 standard.

Fig. 4.9: LO integrated Raman intensities for crystalline GaAs and for the implants of 1 and 5 x 10^{14} cm^{-2}, over a wide range of photon energies. All are normalized to the CaF_2 standard. The dashed curve shows the spectral dependence of the optical penetration depth for the high-implant sample.

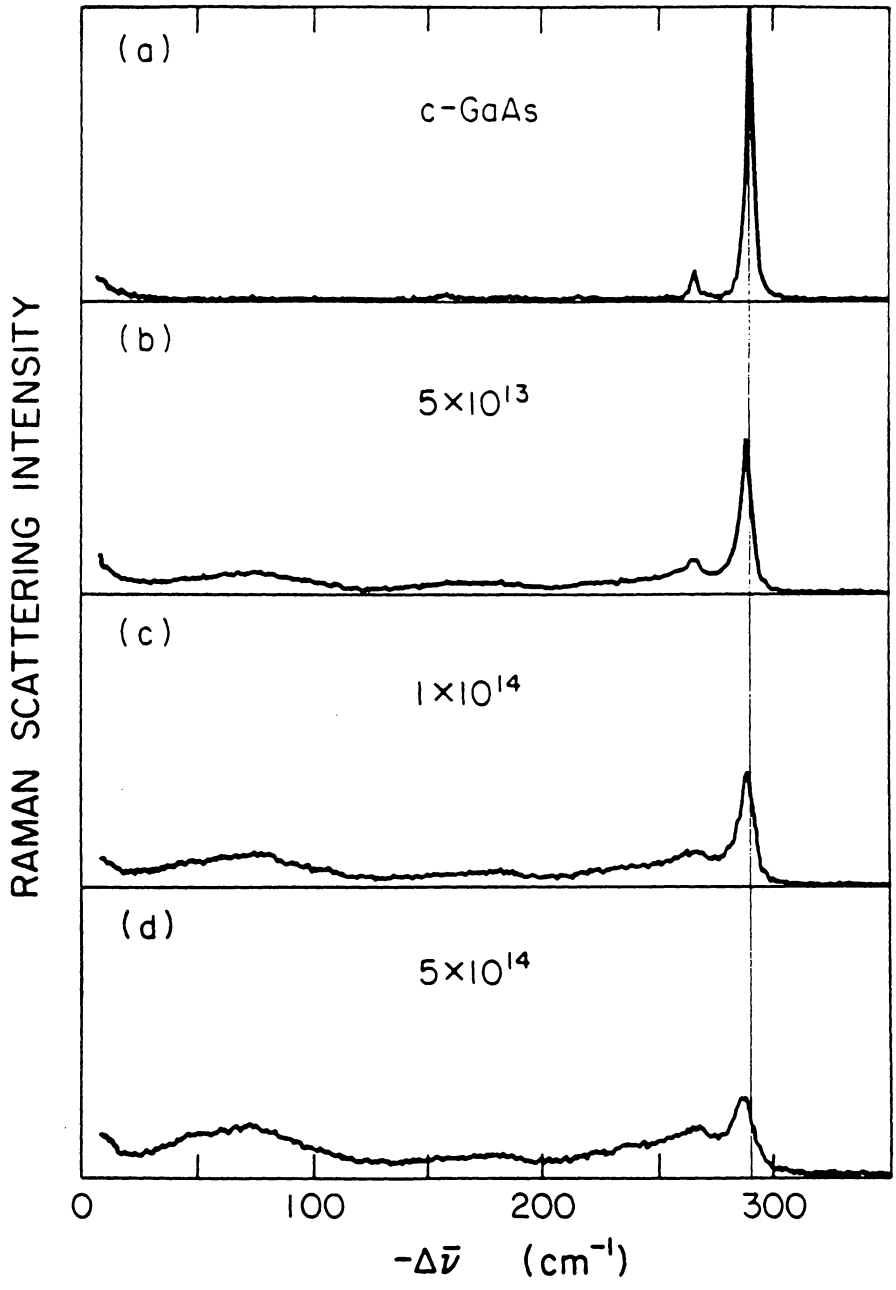

Fig. 4.1 45-keV Be^+ implant sequence.

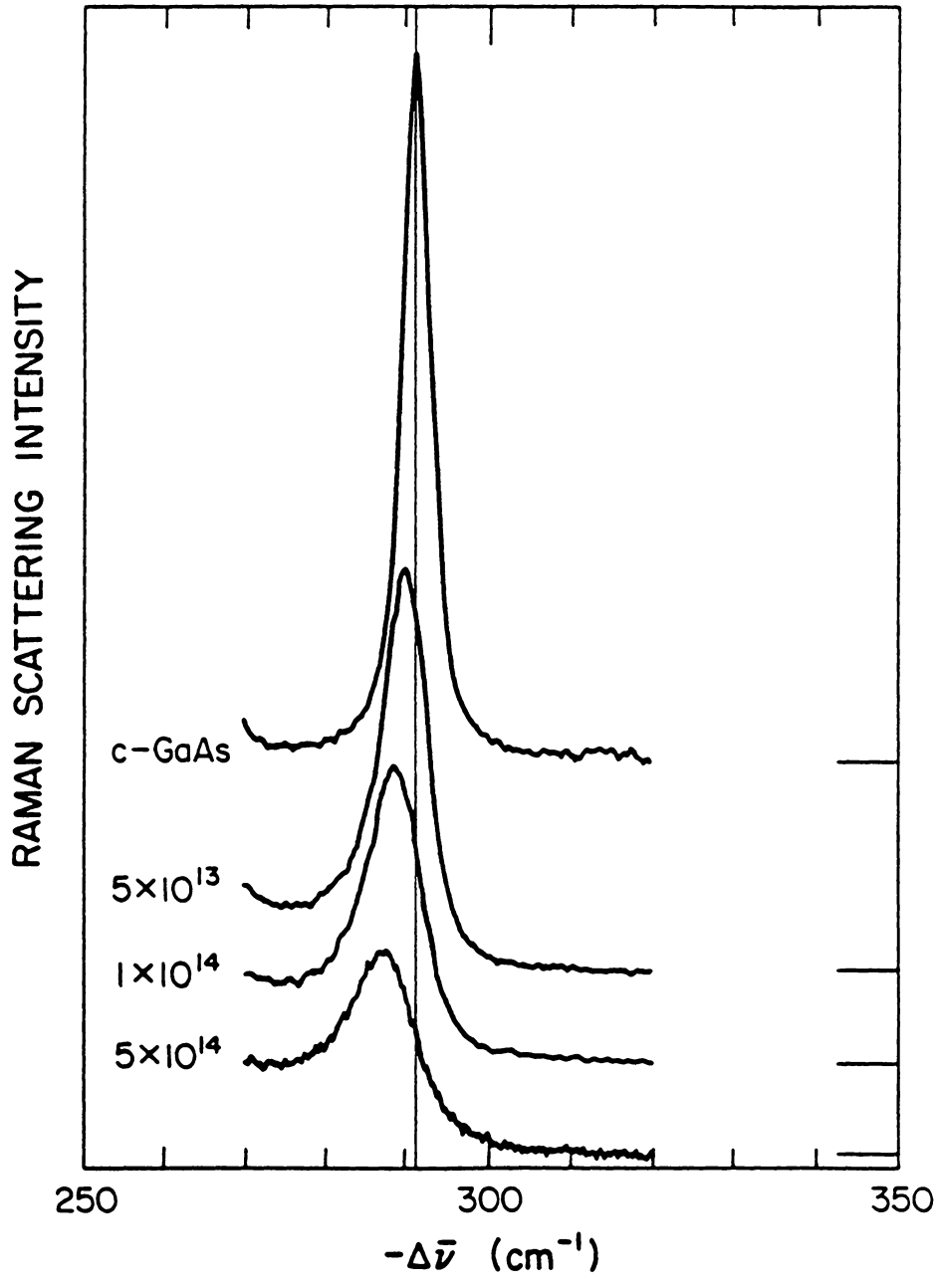

Fig. 4.2 Details of LO line for 45-keV Be^+ sequence.

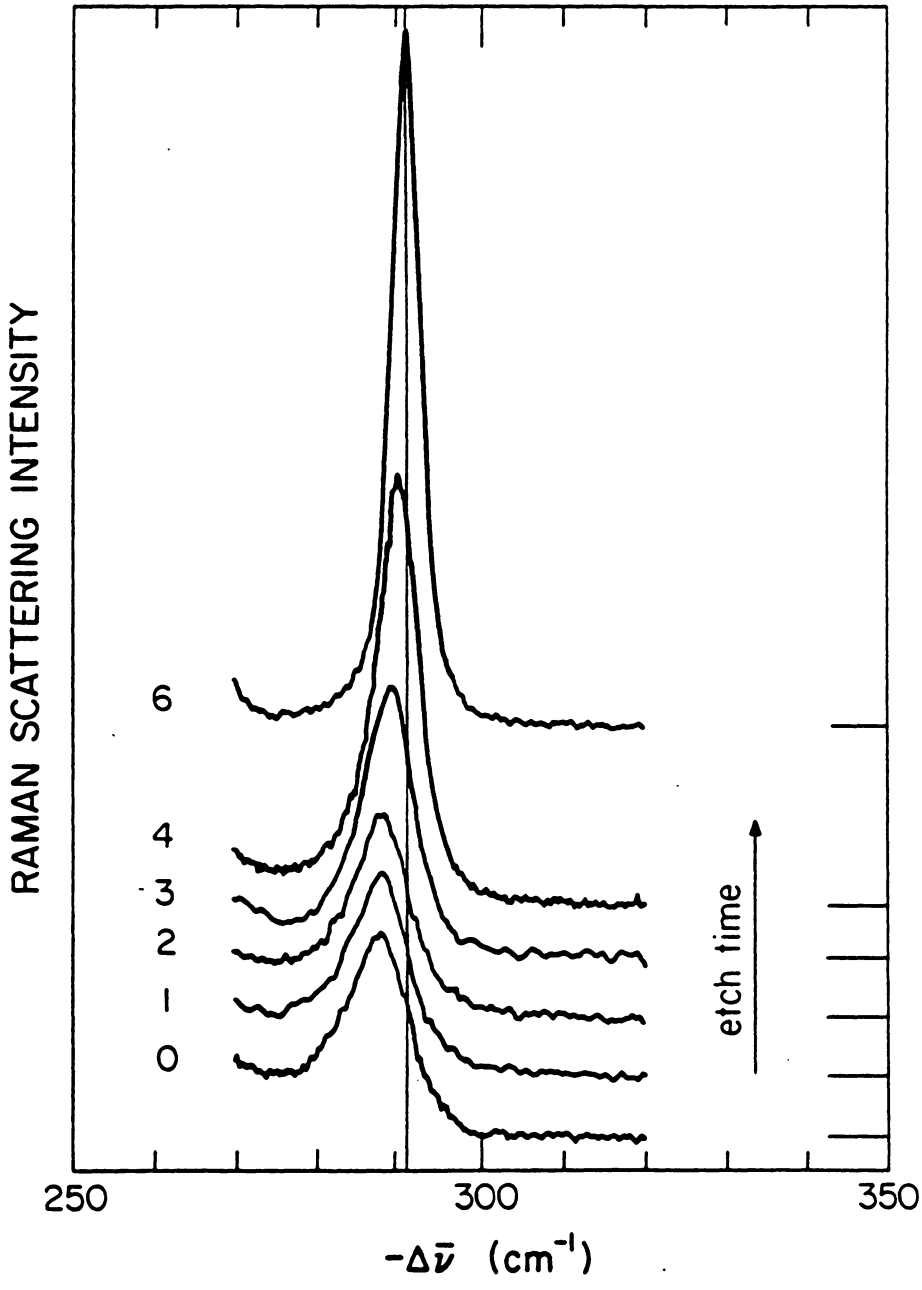

Fig. 4.3 LO phonon evolution vs. etch depth.

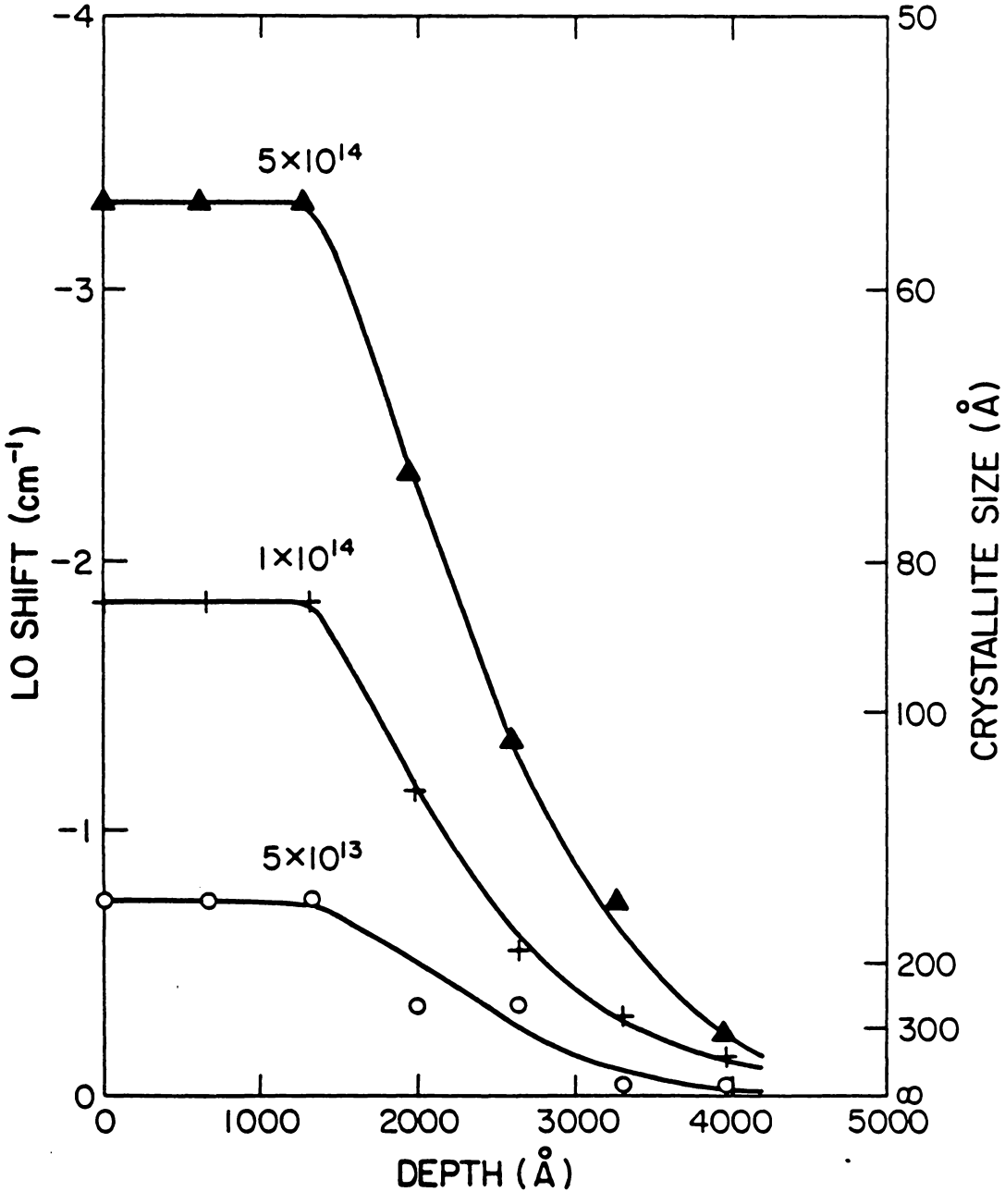

Fig. 4.4 LO line frequency shift vs. etch depth.

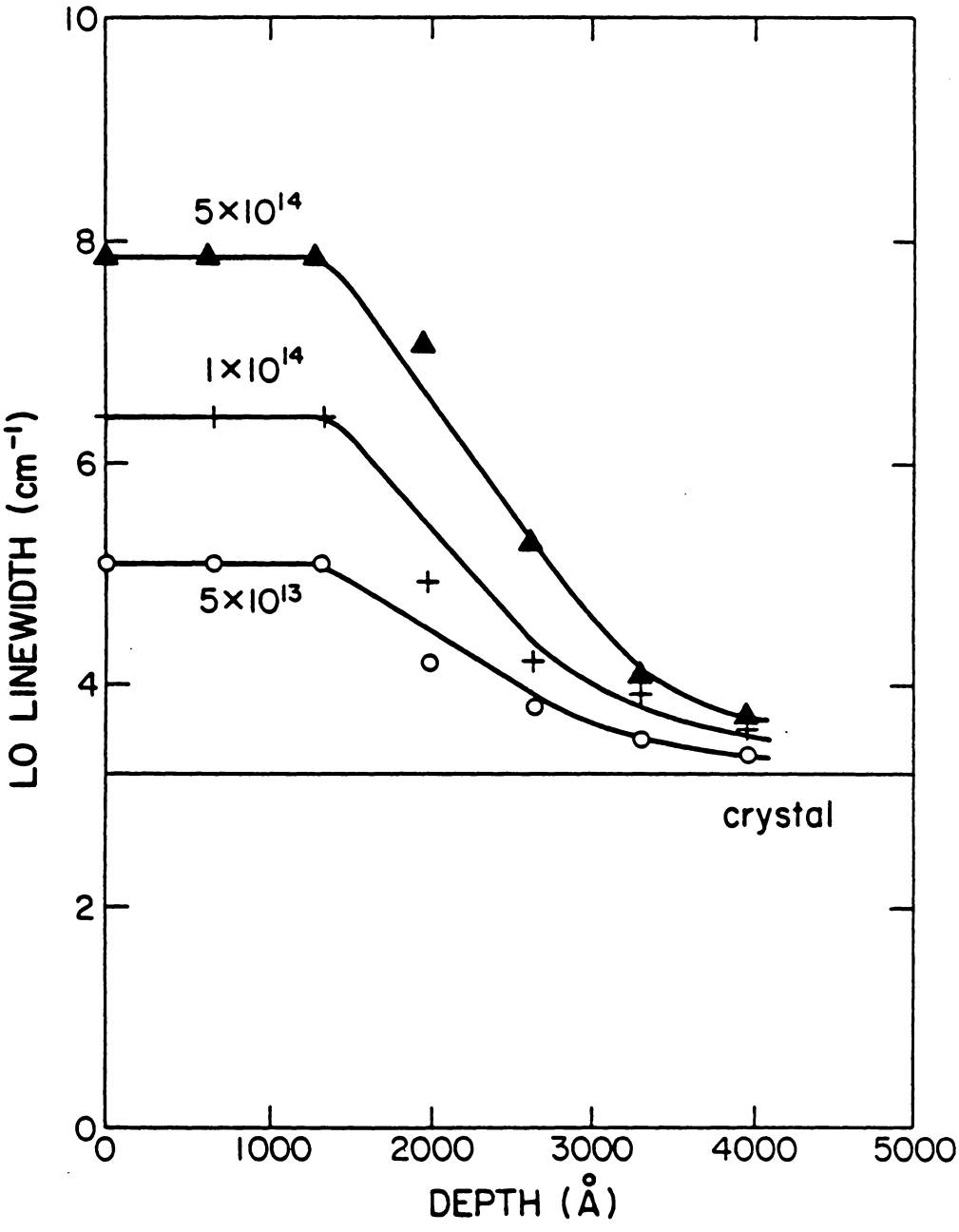

Fig. 4.5 LO line FWHM vs. etch depth.

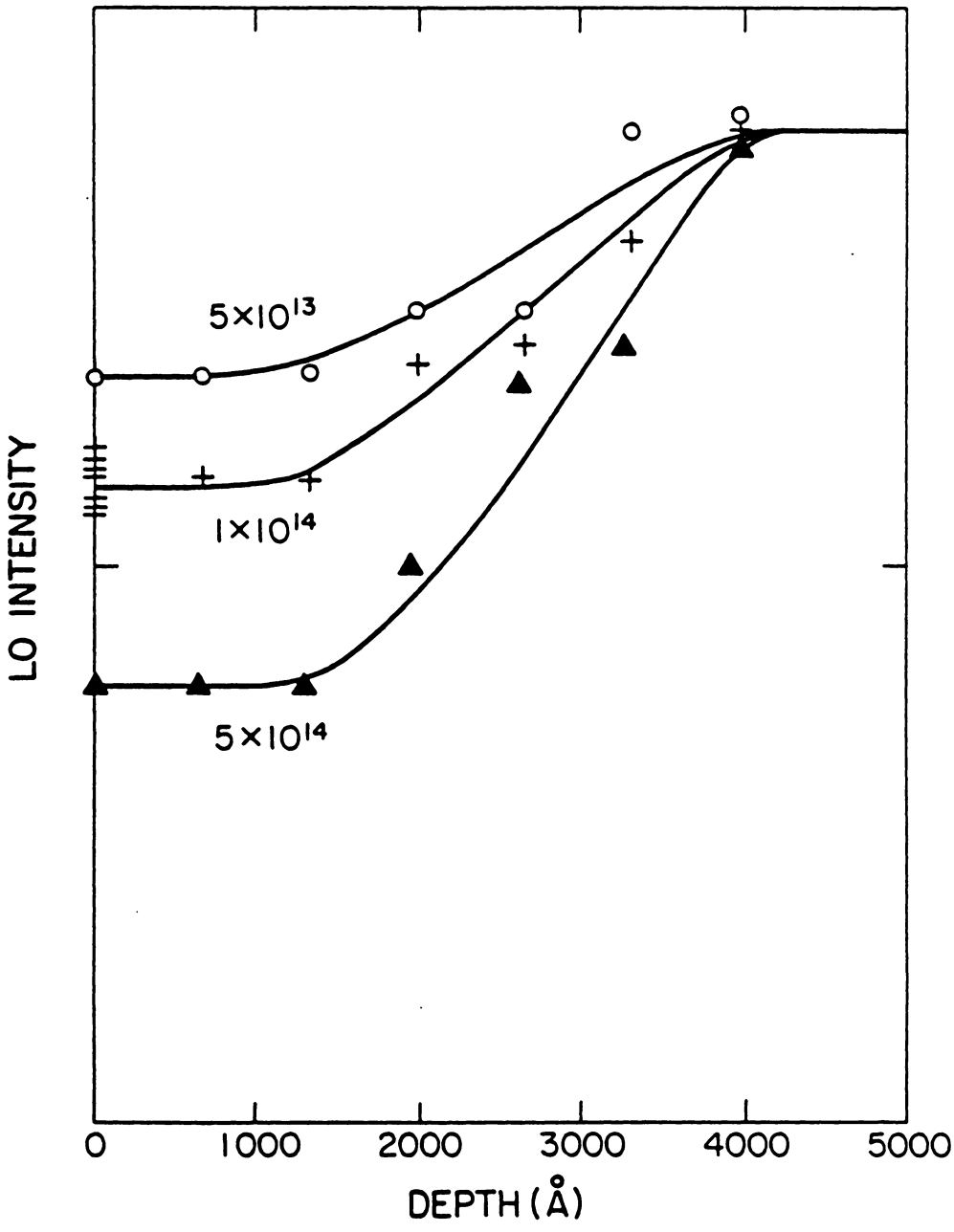

Fig. 4.6 LO line intensity vs. etch depth.

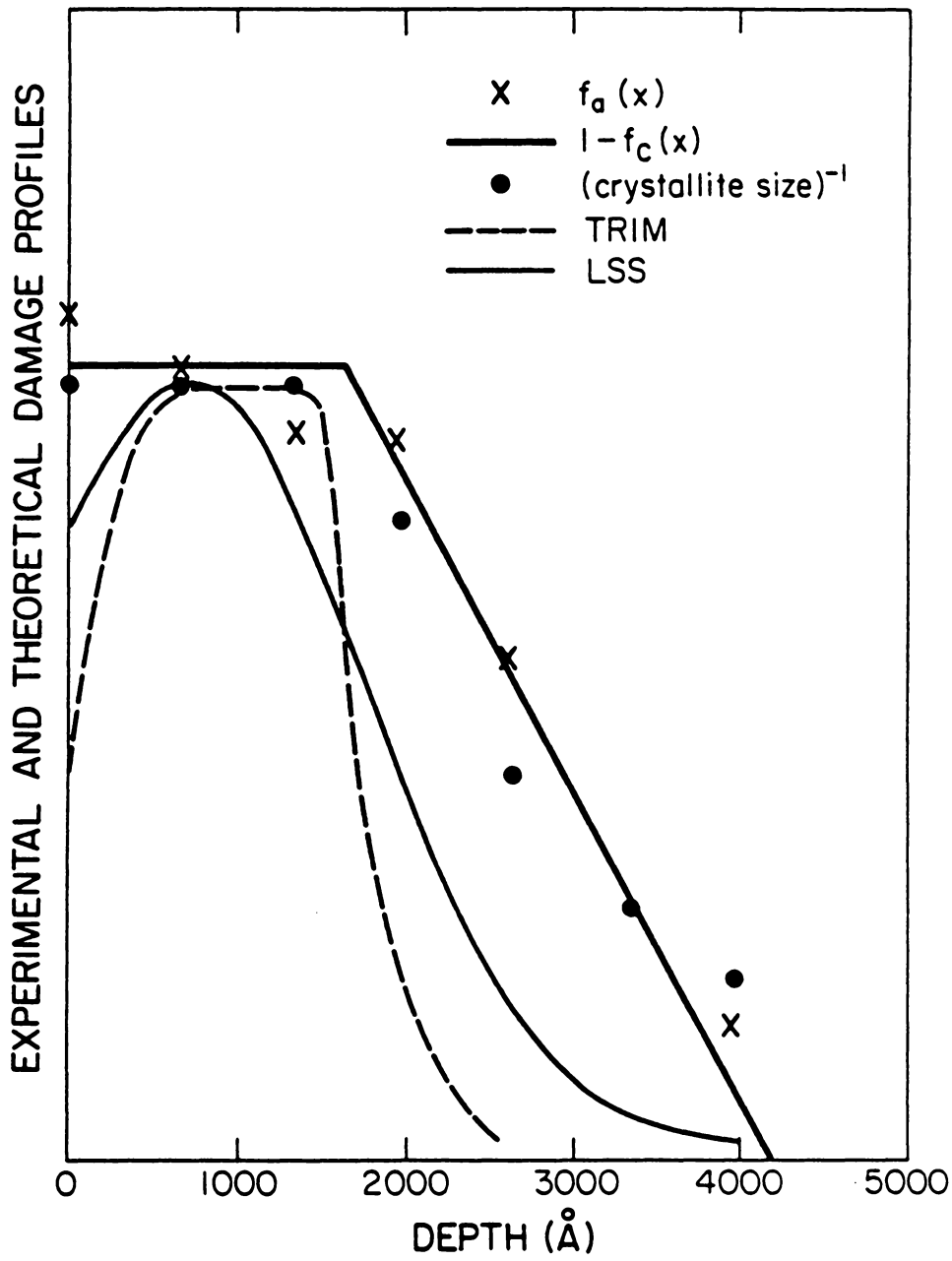

Fig. 4.7 Comparison of 3 exp. depth profiles and theory.

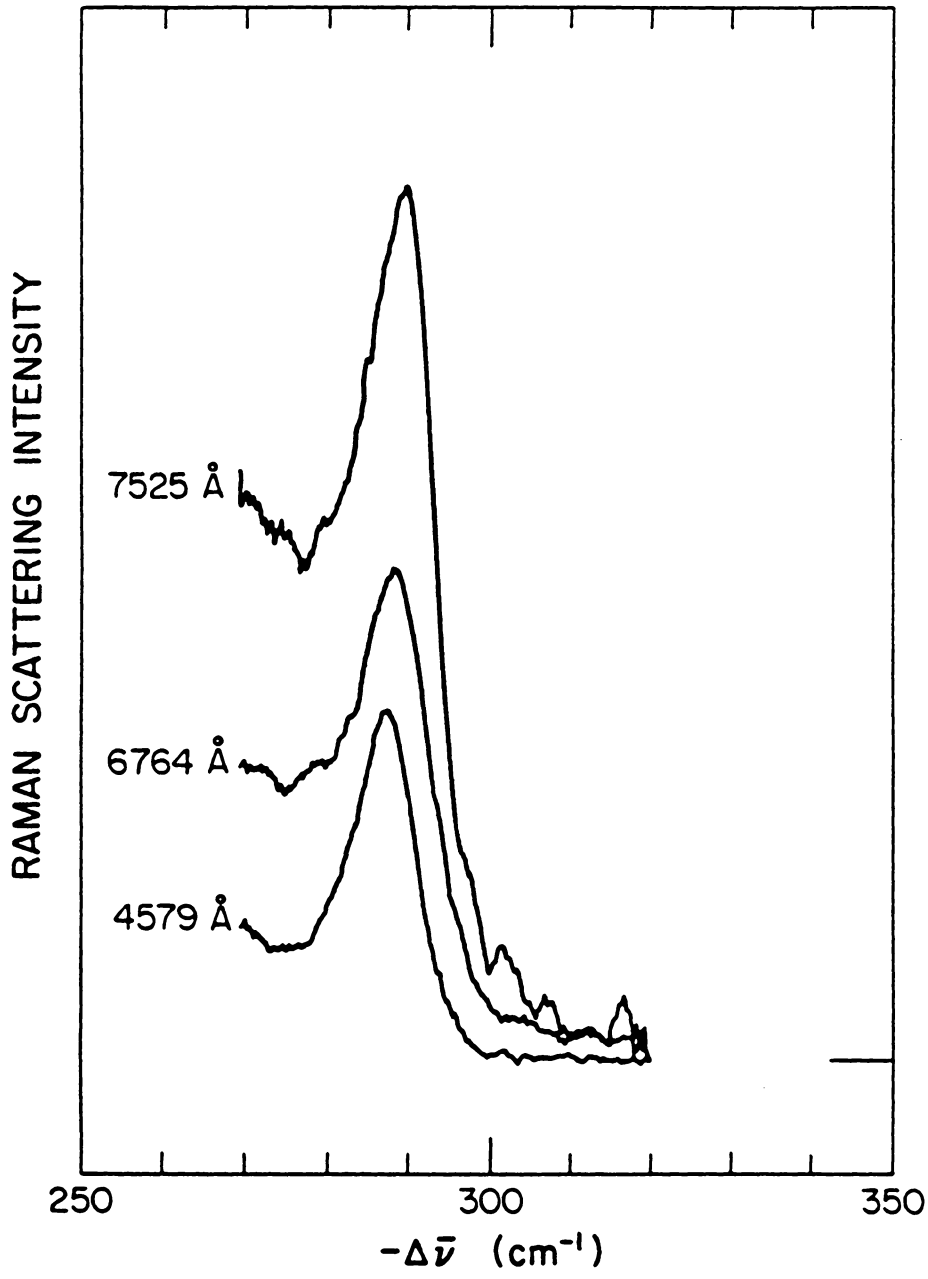

Fig. 4.8 LO line characteristics vs. laser wavelength.

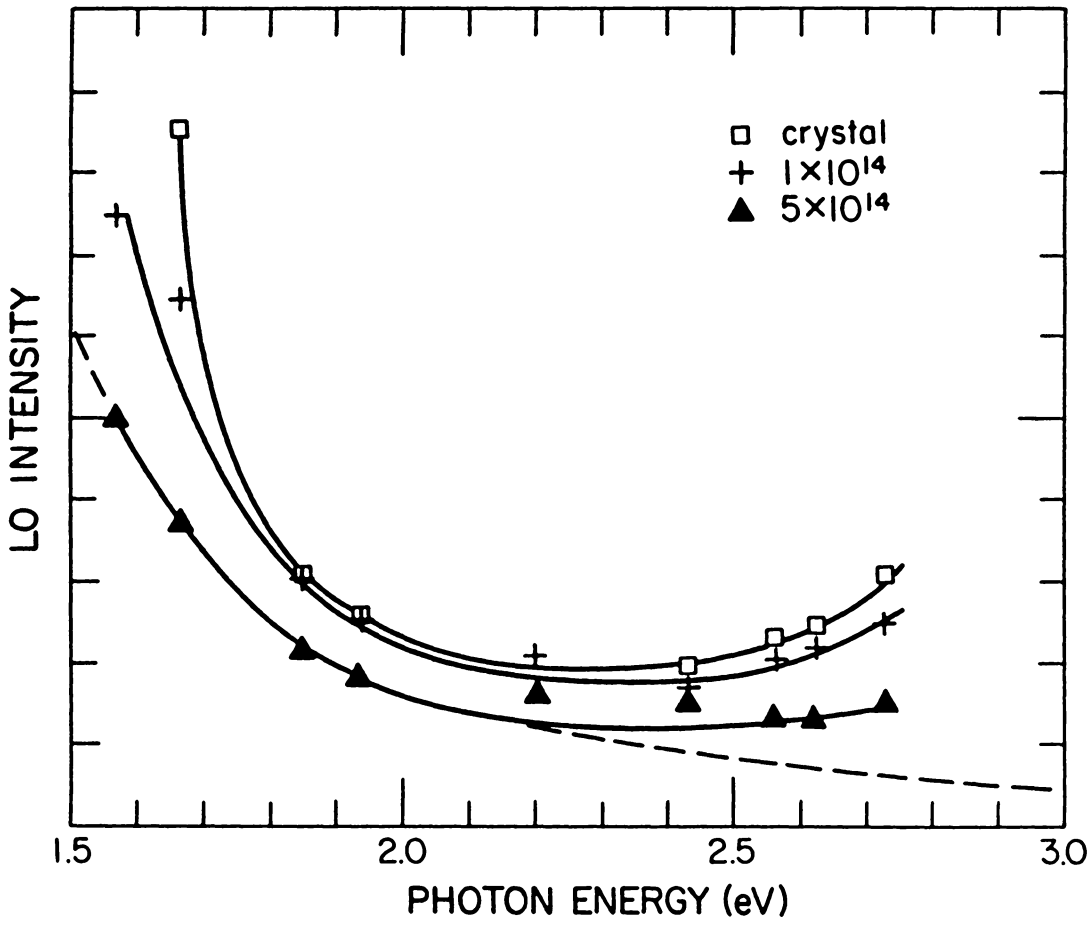

Fig. 4.9 LO line intensity vs. $\hbar\omega_L$.

CHAPTER 5: RAMAN SCATTERING USED FOR NON-DESTRUCTIVE DEPTH PROFILING

5.1 FULLY AMORPHOUS DAMAGE LAYER

In Ch.4 a damage depth profile was obtained solely from the spectroscopic characteristics of the LO phonon. The range of depths sampled by the Raman probe was controlled by etching successive layers from the surface of the implanted GaAs. In this section the usefulness of Raman scattering as a non-destructive depth probe is explored for the case of the fully amorphous ion-implanted GaAs (see Ch. 3). For this case, absorption coefficients for the homogeneous, single-phase surface material are known [Theeten & Erman].

Several non-destructive optical studies have been carried out, primarily in implanted silicon, to depth profile implanted damage layers [e.g. see: Balkanski et al., deWilton et al., Kim & Park, Kwun et al., Opyd et al., Theeten & Erman]. Other techniques which have been used include Rutherford backscattering [Bhattacharya et al.] and EXAFS [Bouldin et al.]. deWilton et al. varied the depth of their Raman probe into a-Si by controlling the angle of incidence of the laser beam (the c-Si TO phonon line seen superimposed on the a-Si broad bands is isotropic with respect to orientation, unlike the GaAs LO line).

Balkanski et al. varied the optical penetration into their a-Si implanted layer via the excitation photon energy.

By controlling the photon energy of the Raman excitation, the optical absorption coefficient (penetration depth) may be varied. As with c-GaAs, when light approaches the "pseudo-gap" in a-GaAs (from above) the absorption coefficient decreases, although less rapidly than in the crystal. Thus, for thin enough layers, one may be able to "look" through one phase into the other. For c-GaAs [Aspnes & Studna] and a-GaAs [Theeten & Erman] the optical penetration depths have been listed in Table 2.3 for the pertinent laser lines.

A detailed photon-energy depth profile is shown in Fig. 5.1 for the GaAs amorphous layer created by implanting c-GaAs with 120-keV SiF_3^+ ions to a fluence of 2 x 10^{14} cm^{-2} (see Fig. 3.6). For small optical penetration (2.71, 2.41, and 2.19 eV, corresponding to a-GaAs penetration depths of 90, 140, and 190 A, respectively) the Raman spectra are all identical (for the 2.41-eV spectrum see Fig. 3.6) both to each other and to the a-GaAs Raman spectra of Fig. 3.8. This indicates that the a-GaAs layer is homogeneous to optical probes with $\hbar\omega \geq 2.2$ eV.

For 1.91-eV excitation a small LO phonon signal is observed in Fig. 5.1 above the a-GaAs spectrum near 290 cm^{-1}. This spectrum is a superposition of the spectrum of

the a-GaAs surface layer and a weak contribution from a microcrystalline region. Light of this energy is therfore seen to penetrate beyond the a-GaAs top layer to sample the microcrystalline region beneath, which has been damaged to a lesser extent. Of course the microcrystalline LO phonon contribution is expected to be accompanied by an a-GaAs component, due to the mixed amorphous/microcrystalline nature which is found to prevail throughout these systems.

By 1.84 eV the LO line is stronger in Fig. 5.1, consistent with increased penetration into a less damaged region. The LO phonon frequency is 292 cm^{-1}, indicating large crystallites ($\ell \geq 200$ A), but it is still broader than the crystalline LO line, indicating some damage persists.

For 1.65-eV light the LO phonon scattering is strong and nearly identical to the LO phonon of single-crystal GaAs. Increasing d_{OPT} therefore eventually succeeds in probing beyond the fully amorphous damage layer deeper into the microcrystalline, low-damage transition region between the a-GaAs top layer and the undisturbed c-GaAs below.

The fact that even 1.65-eV light is not substantially probing the single-crystal GaAs presumed to reside beneath the damage layer is established by another optical process. In this photon-energy range, the room

temperature photoluminescence intensity (emission of light via direct electronic interband transitions in the crystal) is large in comparison to the Raman-scattering intensities. At $\hbar\omega_L$ = 1.65 eV the photoluminescence signal from the un-implanted c-GaAs starting material is much stronger than the Raman spectrum. Since this is not observed in the top spectrum of Fig. 5.1, it is clear that the strong LO signal comes from slightly damaged GaAs. Evidently, photoluminescence is more sensitive to low damage states than Raman scattering, although no information can be obtained from photoluminescence once the damage level is sufficient to quench it.

Also observed in the Raman spectra of Fig. 5.1 which possess an LO line is a weak feature near 50 cm^{-1} (seen only as a shoulder at 1.84 and 1.91 eV). The weakness of this feature indicates that it is coming from the amorphous/microcrystalline transition region and not from the a-GaAs top layer. It is not seen in the a-GaAs spectra of Ch. 3. The nature of this newly observed feature is discussed in detail in Ch. 6.

In each spectrum shown in Fig. 5.1 a superposition of the amorphous and crystalline spectra is observed. This suggests that Raman scattering may be useful for non-destructively depth profiling. One may be tempted to deduce that the thickness of the a-GaAs layer is between

d_{OPT} for 2.19-eV light and 1.91-eV light (190 and 270 A, respectively). However, this would be wrong.

For a simple, two-layer system (a-GaAs on c-GaAs) light penetrating into the second layer and back out again would be attenuated by a factor

$$e^{-2\alpha t} = e^{-t/d_{OPT}} \qquad (5.1)$$

where α is the $\hbar\omega$-dependent optical absorption coefficient, and t is the thickness, of the a-GaAs top layer. Thus, a 230-A layer of a-GaAs would permit ~ 30% of the 2.19-eV light to traverse the distance t into the crystalline sub-layer and, if scattered, back out again. The data in Fig. 5.1 do not support this.

In Ch. 6 it is demonstrated experimentally that the a-GaAs spectrum and the crystalline LO phonon have intensities which depend only on scattering volume (penetration depth) below ~ 2.2 eV. (In fact, the a-GaAs component intensity depends on scattering volume alone over the entire photon-energy range studied, 1.55 to 2.71 eV.) Normalizing the LO line intensity to the a-GaAs component intensity will therefore give an indication of the volume of crystal being probed.

The light attenuation due to the a-GaAs surface layer still results in the same factor in Eq.(5.1) with d_{OPT} for a-GaAs. In Fig. 5.2 the c-GaAs intensity is

plotted versus $2\alpha_a$ [Theeten & Erman] on a semi-log scale. The data are consistent with

$$I_c \sim e^{-500/d_{OPT}} \qquad (5.2).$$

Thus, by a straightforward analysis the a-GaAs layer is estimated to be 500 A ± 10% thick. Since the depth dependence of the transition region between the completely amorphous region and the crystal has been ignored, the 500 A estimate may be slightly high.

Between photon energies of 1.91 and 2.19 eV the factor in Eq.(5.2) drops by more than a factor of two. The 2.19-eV attenuation factor of 0.07 therefore serves as a practical lower-limit estimate for the detection of crystalline features through an amorphous layer.

Note that, in Fig. 5.1, no decrease is observed in the degree of damage close to the surface (smaller d_{OPT}). This is the same conclusion reached in Ch. 4 for the 45-keV Be^+ (and noted for the 180-keV Be^+) implants which had not reached a damage saturation stage. We conclude that the theoretical "prediction" of such a near-surface dip in the level of damage for ion-implanted systems [Lindhard et al., Ziegler et al., Carter & Grant] incorrect, on the basis of these experimental results, and others: see section 5.2 and [Bouldin et al., Kim & Park, Kwun et al., Opyd et al., Theeten & Erman].

SiF_3^+ has an atomic mass of 85 amu. However, due to the size of the molecule it is expected to break down into its atomic constituents upon initial contact with the GaAs target. If this initial collision is assumed to be elastic, then ~ 40 keV of the 120-keV initial energy goes with the ^{28}Si and each ^{19}F atom gets ~ 27 keV. LSS [Lindhard, Scharff, & Schiøtt] estimates for the 40-keV silicon ion ranges in GaAs are 300-400 A for the depth of the peak Si concentration and 700 A for the maximum range of the ions (i.e. related to total depth of the damage). For F we estimate ~ 400 A for the depth of the concentration maximum and 1000 A for the maximum range. Incidentally, for a single atom of 85 amu projected at 120 keV into GaAs, LSS theory predicts a peak ion concentration ~ 400 A deep and a range of ~ 600 A.

The LSS ranges are therefore consistent to zeroth order with the experimental scale. Our fully amorphous layer, however, extends beyond the predicted peak ion concentration for the extreme cases considered above. This was also found for the 45-keV Be^+ depth profile of Ch. 4. It is expected (by LSS as well) that the implanted ion concentration depth profile would lie deeper than the damage depth profile: ions about to stop may still travel but may not have sufficient energy to cause lattice damage. The usefulness of LSS theory to predict damage

concentrations or ion concentrations is therefore questionable.

An interesting point is that if we use the 0.07 estimate of the lower limit of detection (exponential factor in Eq.(5.1) equal to 0.07) along with the 500-A thickness estimate for a-GaAs on c-GaAs, then the 1.65-eV laser light (top spectrum in Fig. 5.1) probes significantly to a depth of nearly 5000 A. Since no photoluminescence is observed, this implies that disorder persists to 5000 A due to the SiF_3^+ implant. This estimate is large of course because the d_{OPT} used for the underlying material was that of c-GaAs [Aspnes & Studna], and, as just noted, the material is not simply crystalline. A lower bound for the effectiveness of the 1.65-eV light depth probe comes from a homogeneous, purely amorphous, infinitely thick layer. For this case substantial light scattering comes from the near-surface region up to a depth of 1400 A. Even this lower limit indicates that the total depth of the disorder extends much farther than the LSS prediction. This was also found to be true (Ch. 4) for the 45-keV Be^+ implants in GaAs.

The usefulness of Raman scattering as a depth profiling technique is restricted to estimates for simple cases, in this study. For the implant considered here, 2 x 10^{14} cm^{-2} SiF_3^+ ions at 120 keV, the crystalline LO phonon

intensity was found to vary exponentially as in Eq.(5.1), see Fig. 5.2. For a simple, two-layer model consisting of a-GaAs on top of c-GaAs, the a-GaAs layer is estimated to be 500 A thick. This agrees with the orders of magnitude predicted by LSS theory, although the full extent of the damage into the crystal is significantly larger than the predictions.

5.2 AMORPHOUS/MICROCRYSTALLINE DAMAGE LAYERS

Implanted GaAs which is not fully amorphous can also be depth-probed non-destructively by varying the excitation photon energy. In Figs. 5.3 and 5.4 it is shown how this technique may be carried out by characterizing the microcrystalline LO phonon alone. The LO phonon frequency and line width give a direct measure of the degree of damage probed by the light. If the phonon frequency or width are known, then the average crystallite size may be estimated (see Ch. 3).

In Fig. 5.3 the LO peak frequency is recorded for $\hbar\omega_L$ between 1.55 and 2.71 eV for three samples discussed extensively in Ch. 6: 180-keV Si^+, 180-keV Be^+, and 45-keV Be^+, each implanted to a fluence of 5×10^{14} cm^{-2}. The 45-keV Be^+ implant was found to have a surface layer which exhibited uniform damage up to ~ 1500 A. For this implant (shown as open circles in Fig. 5.3), the LO phonon

frequency is constant at approximately 288.3 cm^{-1} over the full range of depths probed. For this sample the LO line FWHM, shown versus $\hbar\omega_L$ in Fig. 5.4, is also constant at about 8.2 cm^{-1}. This confirms that this non-destructive technique yields results consistent with the etch profile of Ch. 4, provided the line shape only is considered (intensities will be discussed in Ch. 6). This same consistency was also noted in reference to Fig. 4.9.

For the 180-keV Be^+ implant Fig. 5.3 reveals the LO phonon frequency to be nearly constant at 288.8 cm^{-1}. An etch profile of this implanted sample was carried out between zero and ten minutes, as shown in Fig. 5.5. The spectra from no etch to eight minutes of etch (inclusive) are all the same. At low frequency, one must be careful to consistently subtract the parasitic scattering of the laser light, which is much stronger for the etched samples. This is indicative of surface degradation which occurs during the chemical etch.

The Raman spectrum after ten minutes of etch time is substantially different than for zero to eight minutes of etch time. Thus, this high-energy implant results in a uniformly damaged layer extending from the surface to approximately 5000 A.

For c-GaAs, 1.55-eV light has an optical penetration depth d_{OPT} = 3900 A [Aspnes & Studna].

Although d_{OPT} is not this large for damaged GaAs, the etch-depth results and the photon-energy results of Figs. 5.3, 5.4, and 5.5 are consistent and from Fig. 5.3 or 5.4 we now <u>know</u> that light with $\hbar\omega_L \geq 1.55$ eV probes a region of uniform damage (i.e. constant crystallite size distributions <u>and</u> amorphous/crystalline volume fractions).

Data are also shown in Figs. 5.3 and 5.4 for the 180-keV Si^+ implanted GaAs microcrystalline LO phonon. It is seen that the LO peak frequency is reasonably constant, showing a slight systematic drop from low to high photon frequencies. The average value is 287.7 cm^{-1}. Since all the data points are close to the average (within the experimental uncertainty), and since a similar trend is seen for the 45-keV Be^+ data, it is concluded <u>non-destructively</u> that this implant produces a uniformly damaged surface layer at least up to the depths probed here. The fact that the clean LO line widths concur with this result provides an important confirmation of this point.

It is therefore demonstrated that for systems which possess a microcrystalline remnant, non-destructive photon-energy depth profiling using Raman scattering is a practical means by which the uniformity of the near-surface region may be ascertained. This is extremely relevant to other optical techniques with photon energies above the

band gap, and is viewed (by me) as a constraint on the validity of compositionally dependent conclusions about implanted systems. This Raman technique has been developed here for two known damage profiles in GaAs (both Be^+ implanted) and applied to a Si^+-implanted GaAs case. The results of these studies are very important for the resonance-Raman investigations discussed in Ch. 6.

FIGURE CAPTIONS

Fig. 5.1 : Variation of the Raman spectrum of the ion-implant amorphized GaAs versus excitation photon energy. The ion dose used was 2×10^{14}-cm^{-2} of 120-keV SiF_3^+. As the photon energy gets closer to the crystalline bandgap (from above), the light penetration depth increases, sampling the less-damaged crystallites below as revealed by the sharp crystalline LO line.

Fig. 5.2 : Semi-log plot of the crystalline intensities of Fig. 5.1, normalized to amorphous intensity (penetration depth), versus $2\alpha(\hbar\omega)$ for a-GaAs.

Fig. 5.3 : LO line frequency versus photon energy for three heavily damaged, but not amorphous samples. The α's for these microcrystalline systems are not precisely known.

Fig. 5.4 : LO line full width at half maximum (corrected for instrumental resolution) for the same three samples of Fig. 5.3. Data points missing at 1.55 eV could not be corrected from the raw data because the instrumental bandpass was larger than the linewidth.

Fig. 5.5 : Full Raman spectra of 180-keV Be^+ implanted GaAs for various etch times. Excitation was with 6471-A, 1.91-eV light; intensity is relative to CaF_2. Spectra for zero through eight minutes are identical, indicating a deep damage plateau. By ten minutes the LO line is sharper, stronger, and higher in frequency than the other spectra.

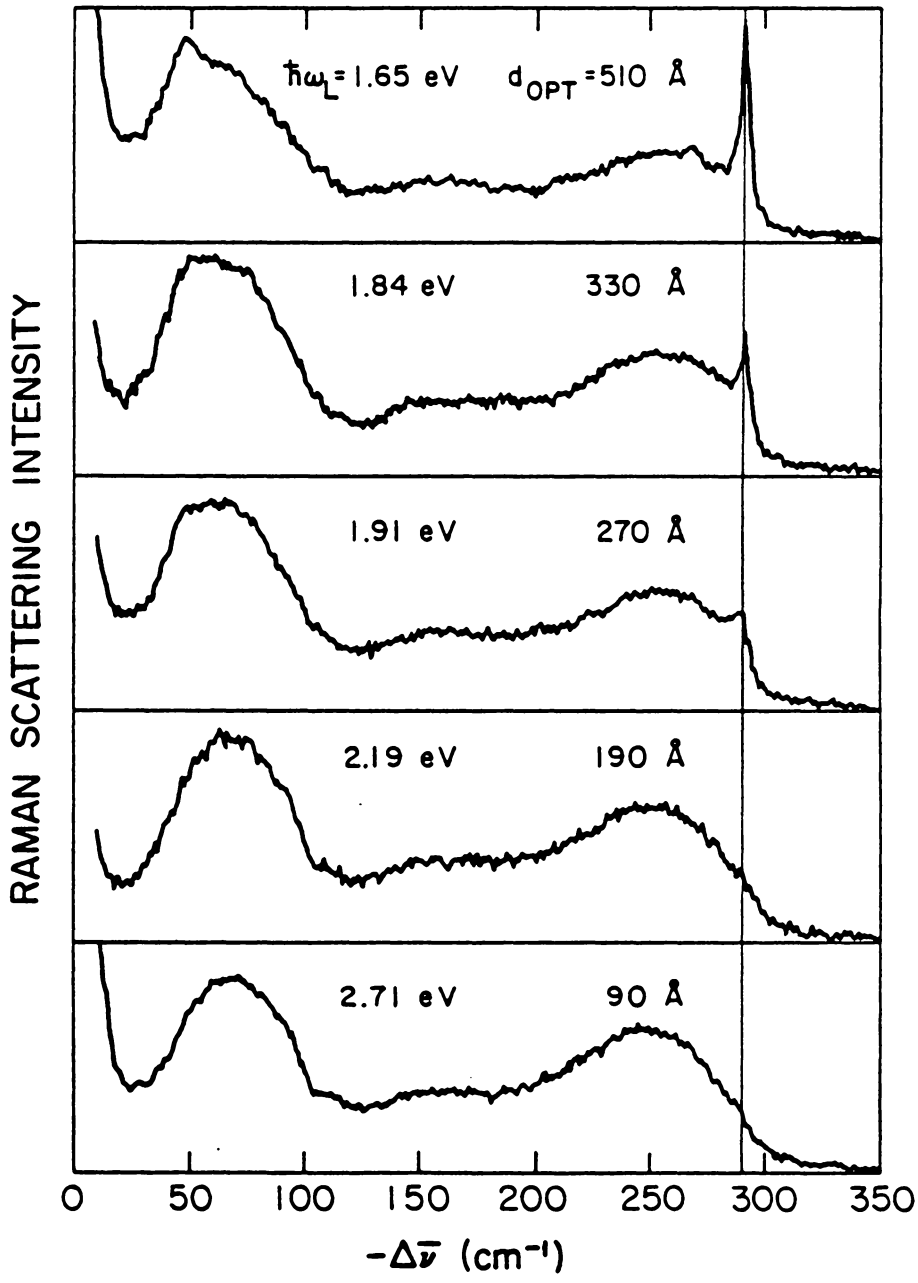

Fig. 5.1 Depth dependence of spectrum in implanted a-GaAs.

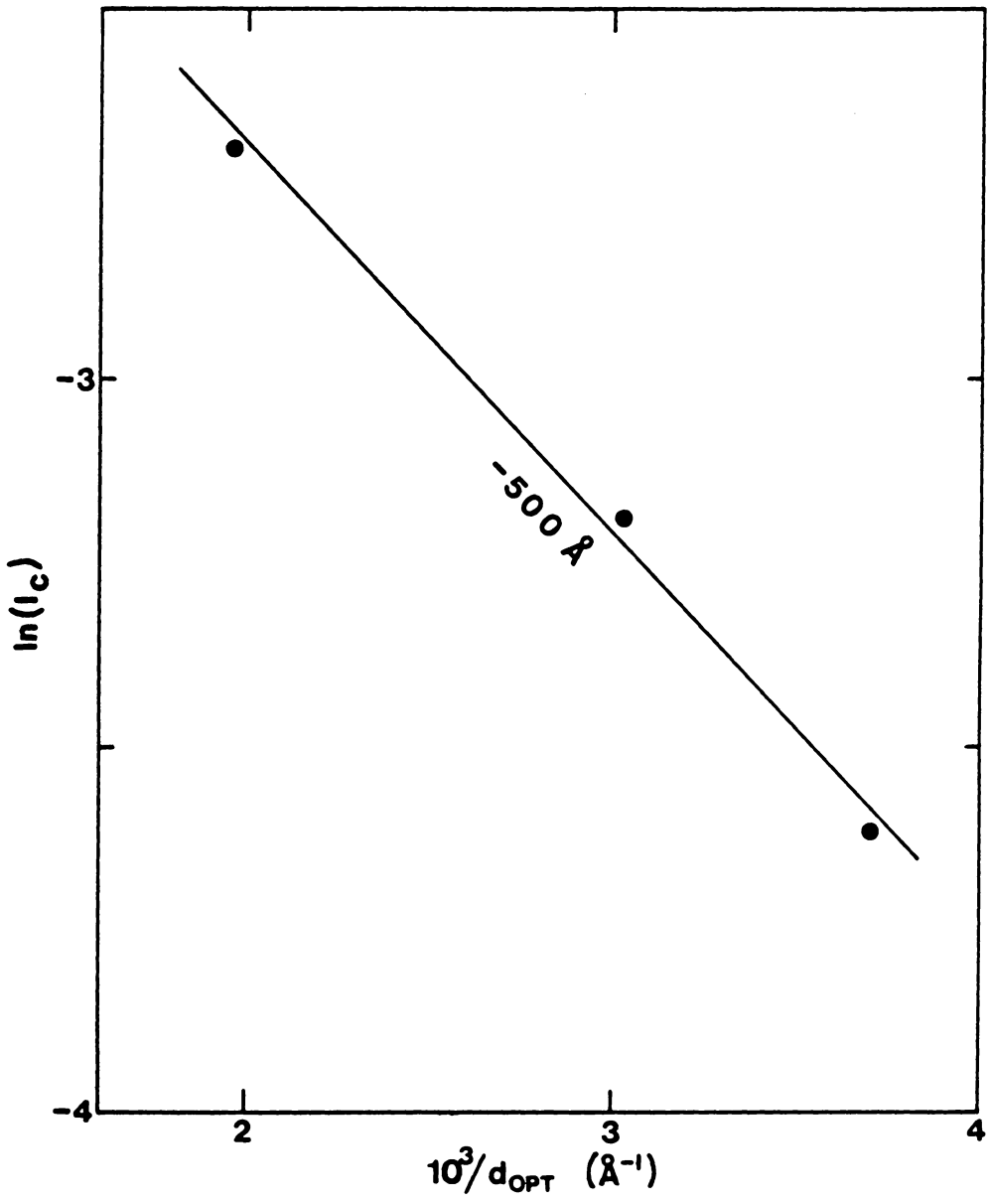

Fig. 5.2 LO phonon intensity vs. 2α.

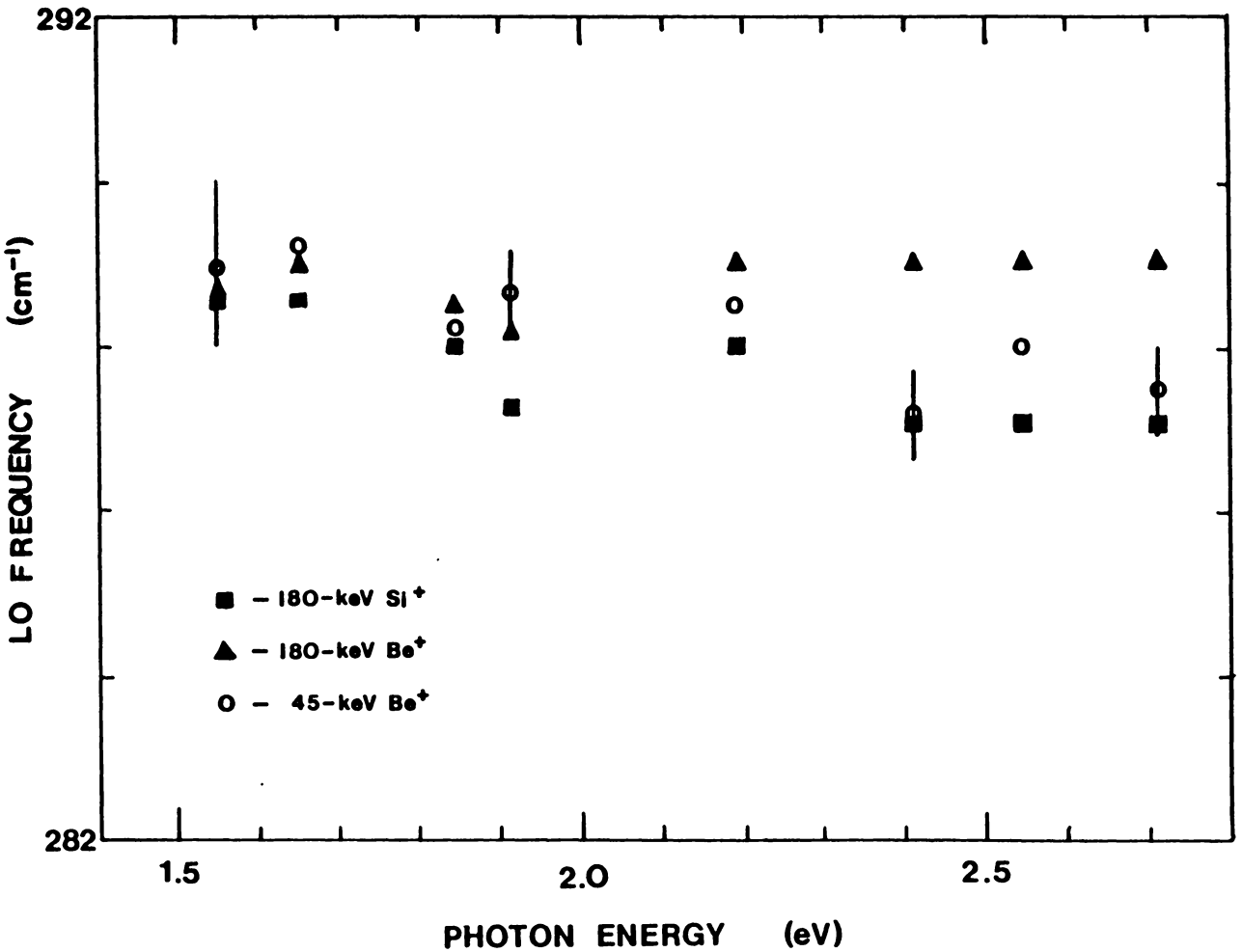

Fig. 5.3 Microcrystallite LO line frequency vs. $\hbar\omega_L$.

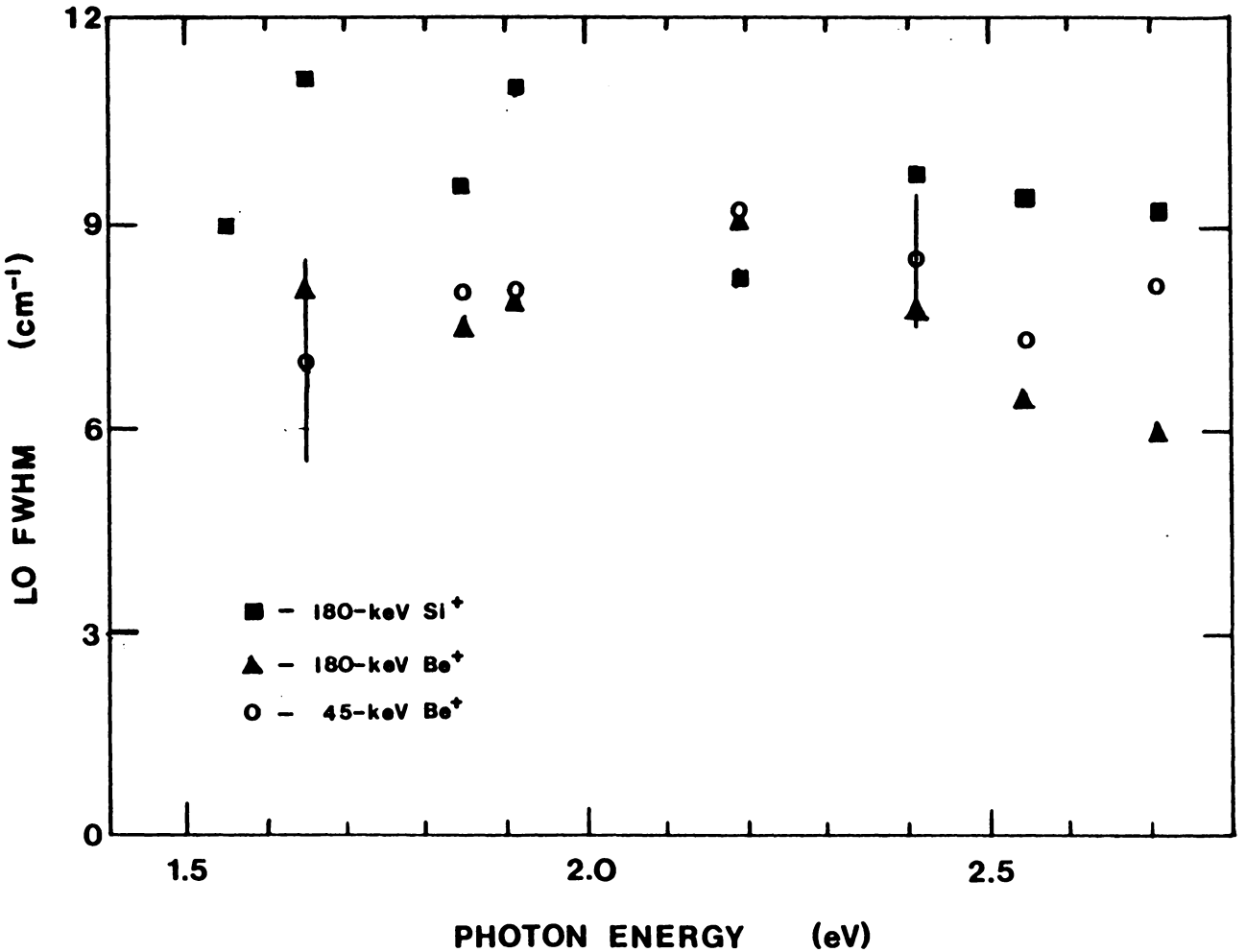

Fig. 5.4 Microcrystallite LO line width vs. $\hbar\omega_L$.

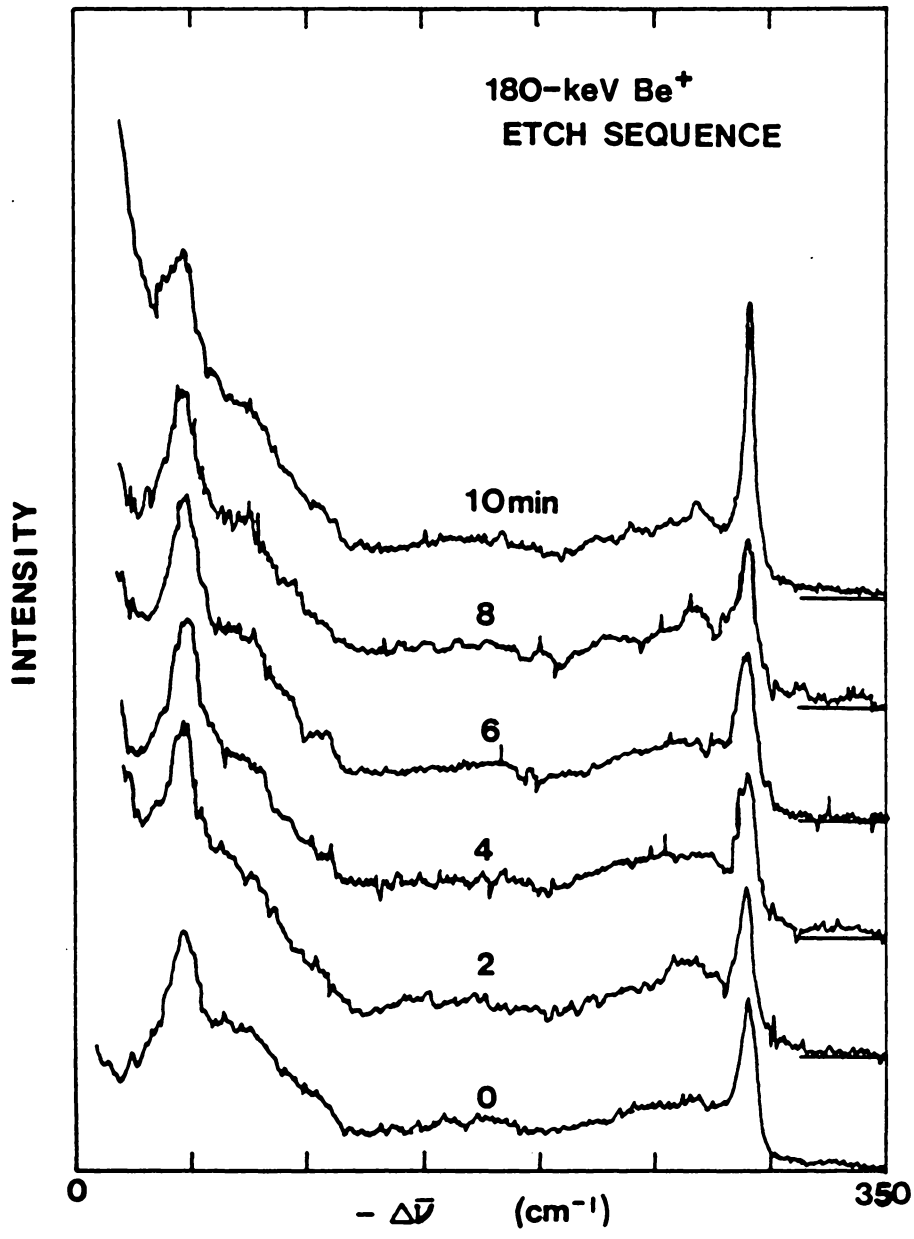

Fig. 5.5 Full Raman spectra vs. etch depth (λ_L = 6471 A).

CHAPTER 6: PHOTON-ENERGY DEPENDENCE OF THE SCATTERING INTENSITIES OF a-GaAs, THE LO PHONON, AND A NEW FEATURE OBSERVED IN THE CRYSTALLINE/ AMORPHOUS MIXED PHASE

6.1 INTRODUCTORY REMARKS

In Chapter 4, we have discussed measurements of the LO scattering intensity for 45-keV Be^+ implanted GaAs. The intensity of the LO line is observed to decrease with increasing ion fluence, corresponding to increased host lattice damage. The decreasing LO scattering intensity is attributed to a decrease in the optical penetration depth (scattering volume) and to a decrease in the fraction of the scattering volume which is still crystalline, as larger volume fractions of the substrate are converted to amorphous GaAs (a-GaAs). By varying the excitation photon energy we also observed that the LO Raman-scattering intensity <u>partially</u> retained its resonance with the E_1 electronic interband transition. Over a photon energy range of 1.55 to 2.2 eV (E_0 = 1.43 eV, [Blakemore]) the LO scattering intensity was found to depend solely upon the scattering volume, well within experimental precision. That study [Ch. 4] is, to our knowledge, the first attempt to study the photon-energy dependence of the Raman emission process in ion implanted GaAs.

Berg and Yu [1985,1986,1987] have discussed the effect that high energy electron and neutron irradiation has on Raman and resonance-Raman processes in GaAs (both bulk and defect related). In their case, the irradiation creates high-density point defects, leaving the material predominantly crystalline. Due to the large penetration depth of their particles, they probed a region of macroscopically uniform damage (homogeneous on a scale of 1000 A or greater), even near E_0 where the optical absorption coefficient is radically decreasing. They present a phenomenological development of disorder-induced resonance-Raman scattering for a variety of processes, in particular for the case of defect-induced first-order Raman scattering [Berg & Yu, (1987)]. Their development derives from the identification, made by Gogolin and Rashba, that impurity-assisted scattering is formally identical to the two-phonon Raman scattering process [Zeyher]. Elastic scattering between an electron (or hole) and an impurity/ defect results in a momentum transfer which may relax the $k = 0$ selection rule and allow (normally forbidden) additional scattering processes to occur. Near resonance these higher-order terms (fourth order perturbation expansion) may have intensities comparable to the allowed spectral features (third order).

In the present work we discuss the nature of a

newly observed strong feature in the Raman spectrum of ion bombarded GaAs: a relatively narrow, strongly resonant, low-frequency band. The intensity of this feature is strongly dependent upon the excitation photon energy. Under appropriate conditions, it is observed to be more intense than the LO phonon. The physical origin of this new Raman band, which is absent in both the crystalline and amorphous GaAs phases, is clearly of fundamental interest. Although our experimental results do not yet appear to permit a definitive identification of the scattering mechanism, we can eliminate some possibilities and support others. We develop an interpretation of this new band based upon disorder-assisted Raman scattering. However, we are obliged to state that the exact origin of the object of our study is still open to speculation.

6.2 OBSERVATION OF THE NEW FEATURE IN ION-IMPLANTED GaAs

Figure 6.1 shows the variation of the Raman spectrum with 45-keV Be^+ ion implant fluence. The excitation is 6471-A (1.92-eV) red laser light. In the crystal the usual $k = 0$ optical phonon selection rule is obeyed, resulting in strong LO phonon scattering since we are backscattering along a (100) direction. Also visible in the spectrum of the crystal is a weak TO line, observed because we are not in a strict backscattering geometry and

because we collect light in a cone about (100). As the implant fluence increases the LO line downshifts, broadens, and decreases in intensity. Simultaneously, the a-GaAs three-band continuum [Ch. 3] increases in intensity and a very strong feature A near 47 cm^{-1} (FWHM = 18 cm^{-1}) is observed, which increases in intensity with fluence. No evidence of peak A is seen in the crystal, but it is evident even for the lowest fluence studied.

Figure 6.2 is a set of spectra, all taken from the 5 x 10^{14} cm^{-2} 45-keV Be^{+} implant, obtained by varying the excitation from 5145 A (2.41 eV) to 7525 A (1.65 eV). At 5145 A the spectrum is typical of ion-damaged GaAs [Tiong, Nakamura & Katoda, Ch. 3] showing the downshifted and broadened LO line and the three-band continuum characteristic of a-GaAs. For this spectrum, excited with green light, feature A is very weak. As the laser photon energy is decreased, two changes occur: the spectrum increases in intensity (as normalized with respect to the CaF_2 standard) and the additional feature A rises above the low-energy broad band.

Previous work [Tiong et al.] has shown that the LO line broadens and downshifts with decreasing crystallite size. In these spectra the LO line is <u>not</u> changing shape or position, indicating that we are probing a range of depths having the same crystallite size distribution. The

increasing penetration depth is not responsible for the increase in A with increasing wavelength. To test this point, the depth dependence was studied via chemical etch removal of successive surface layers. The LO line is unchanging (position, line shape, and intensity) for approximately 1500 A, then it gradually shifts and sharpens and recovers the form of the crystalline LO line by 4000 A [Ch. 5]. Both the a-GaAs spectral component and the A band have intensity depth dependences complementary to that of the LO line: they are very strong near the implant surface then monotonically decrease in intensity with increasing etch depth, becoming unobservable when the observed LO line is identical to that of the crystal. Band A does not change <u>shape</u> during this etching process, only the intensity decreases. This result is independent of the laser wavelength used.

Spectra are shown in Fig. 6.3 for GaAs implanted with 180-keV Be^+ (a), 180-keV Si^+ (b,d), and 45-keV Be^+ (c). The excitation wavelength was 6471 A. Also included (e) is the spectrum we observe with 6471-A excitation for a flash-evaporated thin film of amorphous GaAs [Theye]. Since all vibrations are Raman-allowed, the a-GaAs Raman spectrum resembles the full vibrational density of states (DOS) of the amorphous network [Zallen, p.269]; it shows no sharp features anywhere [note: no indication of A is observed in

ion-implant amorphized GaAs, Ch. 5]. On the other hand, clearly visible in all spectra of the implanted GaAs is the strong peak A at 47 cm^{-1}.

It is also noteworthy to point out that no trace of the peak A was observed in AlGaAs alloyed crystals [Pinczuk]. In that case the disorder-activated zone-edge longitudinal-acoustic peaks in the phonon DOS [Kawamura et al.] were clearly observed.

We have therefore observed a strong feature in the Raman spectrum of ion-implanted GaAs which is not present in either crystalline or amorphous GaAs. From the preceding evidence we can draw the following conclusions about A: (1) Observation is strongly dependent upon excitation photon energy (but not optical penetration depth); (2) Frequency and lineshape are not strongly dependent on the extent of the damage; (3) A is intrinsic to ion-implanted GaAs and its presence is not specific to ion species.

In Fig. 6.4 polarization analyses are shown, obtained using the 6471-A light source. Here x, y, and z are coordinates in the zincblende cubic sublattices, i.e. (100), (010), (001); x' and y' are along (110) and (1$\bar{1}$0), respectively. The scattering direction is taken as z($\bar{z}$). The LO line retains its single-crystal selection rules [Hayes & Loudon] even for these very small crystallites,

indicating that they have kept their original orientation. Amorphous GaAs has a depolarization ratio of ~ 0.7 for the 250-cm^{-1} band (Ch. 3). Results for the a-GaAs components measured here are in reasonable agreement with this. A is primarily diagonal with some $z(x,y)\bar{z}$ scattering. The observed scattering strenghts are summarized in Table 6.1. For the A band, these imply a Raman tensor with components

$$R_{xx} = R_{yy} = a$$
$$R_{xy} = R_{yx} = -e \qquad (6.1)$$

with a and e positive, and $a \approx 4e/3$. The remaining entries in the 3 x 3 representation are undetermined. We find that $z(x',x')\bar{z}$ and $z(y',y')\bar{z}$ result in identical spectra.

6.3 DEPENDENCE OF a-GaAs AND LO PHONON SCATTERING INTENSITIES ON $\hbar\omega_L$

Figure 6.5 displays the photon-energy dependence of I_a, the integrated intensity of the a-GaAs component (normalized to the CaF_2 standard) for three implant cases: 45-keV Be^+, 180-keV Be^+, and 180-keV Si^+ each to a fluence of 5 x 10^{14} cm^{-2}. Amorphous semiconductors are not expected to resonate strongly, because the electronic spectrum lacks sharp structure. The measured scattering

intensity should then be a direct measure of the scattering volume. This postulate is confirmed by the following analysis of Fig. 6.5.

In Ch. 4, consistent estimates for the optical absorption coefficient α were obtained on the basis of spectral evolution with etch depth, and (independently) based on LO scattering intensity measurements and assuming a mixture of crystallites and a-GaAs. Within the mixed amorphous/microcrystalline model, the absorption coefficient is

$$\alpha = f_c \alpha_c + f_a \alpha_a \qquad (6.2).$$

The near-surface volume fractions were $f_c \approx 75\%$ and $f_a \approx 25\%$ for the 45-keV Be^+ case [Ch. 4]. In Fig. 6.5 we show $1/(2\alpha)$ using the 75/25 mixture in Eq.(6.2). Photon-energy dependent α's are from Aspnes & Studna (c-GaAs), Theeten & Erman (a-GaAs). The vertical scale for the $1/(2\alpha)$ curve has been adjusted to fit the I_a data: the agreement for the photon-energy dependence is good. Thus, we confirm that the measured a-GaAs intensity provides a good internal spectral measure of scattering volume. Normalizing other spectral components with respect to I_a thus allows us to obtain intensity values proportional to scattering efficiencies.

In Fig. 6.6 we implement this procedure for the LO line. The LO band integrated intensity is shown, normalized to the I_a values of Fig. 6.5, for the same three implants of Fig. 6.5. For $\hbar\omega < 2$ eV, the LO intensity is approximately constant, exhibiting no strong resonance effects. For higher photon energies, the scattering efficiency is clearly increasing, indicative of resonance with the approaching E_1 interband direct electronic transition which occurs at 2.9 eV in c-GaAs.

The LO line, which is present in the Raman spectrum due to the surviving crystalline component (though broadened and shifted by the effects of finite crystallite size, i.e. spatial correlation [Richter et al.]) is expected to have a resonance spectrum similar to that seen for the bulk crystal [Berg & Yu, (1987)]. The TO resonance-Raman spectrum has been reported by Grimsditch et al.. The scattering cross-section (for E_1 and $E_1 + \Delta_1$ electronic transitions only) is well described by

$$\sigma(\omega) \sim C_1 + C_2 \left[\frac{1}{1 - x_1^2} + \left[\frac{E_1}{E_1 + \Delta_1} \right]^2 \frac{1}{1 - x_{1s}^2} \right] \qquad (6.3)$$

where $x_1 = \hbar\omega/E_1$, $x_{1s} = \hbar\omega/(E_1 + \Delta_1)$, and Δ_1 is the spin-orbit splitting (= 0.2 eV) of the valence bands

responsible for this transition.

Reflectance measurements on our implanted samples, presented in Fig. 6.7, show that the E_1 and $E_1 + \Delta_1$ doublet in the crystalline joint DOS merges into a single, broad feature, with a slight increase in energy. Taking the peak in the DOS to be at the average energy (and the breadth to be $\approx \Delta_1$) Eq.(6.3) becomes

$$\sigma(\omega) \sim C_1 + \frac{2C_2}{1 - (x')^2} \qquad (6.4)$$

with $x' = \hbar\omega/E'$, $E' \approx E_1 + \Delta_1/2$. The cross-section in Eq.(6.4) is plotted in Fig. 6.6 with $C_1/C_2 = -0.5$, scaled to the data. The agreement between the data and Eq.(6.4) is acceptable, although Eq.(6.3) also provides similar agreement. The reason for this lack of resolution is because our data is still far from the peak in the DOS which is near 3 eV.

The general agreement between the LO scattering intensity data and Eq.(6.4) (or Eq.(6.3)) gives us confidence about the manner in which features which arise from the crystalline volume fraction, and which correspond to allowed Raman-active modes in the crystal, resonate with the electronic structure. Particularly relevant to the present topic is that the LO line is strongly resonating at the high end of our photon energy range, and is <u>not</u>

resonating between 1.55 and 2.2 eV (within our precision and mesh).

In Fig. 6.6 the curve from Eq.(6.4) has been scaled to fit the data for the 180-keV Be^+ implanted GaAs (triangles). This case corresponds to the largest crystallites and crystalline volume fraction. Thus, the stronger resonance at high photon energies is consistent with the lower damage: it is closest to the crystal. The other two implants shown in Fig. 6.6 have a resonance which has been quenched to a greater extent. The curve drawn can be made to fit the less-resonant data via a simple rescaling.

6.4 RESONANCE OF A NEAR E_0, $E_0 + \Delta_0$

In Fig. 6.8 the integrated intensity of peak A is exhibited (normalized to I_a) for the same implants shown in Figs. 6.5 and 6.6, over the same energy range. As can be seen in this figure (as well as directly from the data in Fig. 6.1), the scattering efficiency of A rapidly rises as $\hbar\omega_L$ decreases, it peaks between 1.6 and 1.8 eV, then decreases at 1.55 eV. Note that this strong variation in $I(A)/I_a$ affirms that A does not originate from the amorphous phase.

For the 45-keV Be^+ implant, it is possible that at 1.55 eV the light is weakly penetrating beyond the 1500 A

damage plateau region [Ch. 4]. The light probe may therefore sample regions characterized by different amorphous/microcrystal microstructures. For the 180-keV Be^+ implant, however, we observe a damage plateau (via chemical etch) to at least 5000 A which is larger than d_{OPT} for 1.55 eV light in c-GaAs (3900 A [Aspnes & Studna]). Thus, we are looking at uniform damage in this case across the full photon energy range studied. To determine whether or not we are probing uniform damage, the photon-energy dependence of the LO peak frequency and line width were monitored between 1.55 and 2.71 eV. For all three implants shown in Figs. 6.5, 6.6, and 6.8, both quantities (LO line frequency and FWHM) were constant over the full energy range. We thereby confirm <u>non- destructively</u> that the data in these three figures are from regions of macroscopically uniform damage, for three different implanted GaAs samples. A detailed account of this experiment has been presented in Ch. 5.The drop in $I(A)/I_a$, and consequently the peak in $I(A)/I_a$, is therefore <u>real</u> and the agreement between results for these three implants is quite good.

The results presented in Fig. 6.8 are interpreted as strong evidence of a resonance in A at an energy of about 1.6 - 1.7 eV, in the range between the E_0 and $E_0 + \Delta_0$ interband electronic transitions at 1.43 and 1.77 eV, respectively. The grid of laser lines used and the width

of the broad resonance peak does not permit an accurate specification of the photon energy at which A has maximum intensity, but identification of the mechanism responsible for A must be in accord with Fig. 6.8 and the general nature of the resonance exhibited here.

In Fig. 6.9 the intensity of peak A, normalized to the LO intensity (to give a measure of scattering efficiency), is shown versus ion fluence for the 45-keV Be^+ and the 180-keV Si^+ series. The excitation was 6471-A light. Over this fluence range the intensity of A is monotonic in ion fluence for both implant sequences. The intensity of A is therefore a measure of damage introduced into the lattice by the ions. This is confirmed by the higher intensities seen in the silicon-implanted GaAs.

Also graphed in Fig. 6.9 is the carefully measured frequency of peak A (right-hand scale). Of course the scales are adjustable, but the fact that both sets of data agree in form with the intensities indicates a weak dependence of the frequency of peak A on the extent of the damage. It is also observed in Fig.6.10 that the frequency has a photon-energy dependence. In obtaining these frequencies it is important to subtract the a-GaAs portion of the spectrum upon which A is superimposed. For both Figs. 6.9 and 6.10, weaker intensities correspond to lower frequencies. This suggests that something systematic in

the subtraction procedure may be responsible for the observed shift in A. If A is shifting with damage, the effect is very weak.

In Fig. 6.11 the intensity of A is related to the crystallite size, obtained from the LO line characteristics using the analysis of Tiong et al.. From this graph it is evident that $I_A \sim \ell^{-1}$ over the range of samples studied. It is interesting to note that if $I_A \sim \ell^2$ (crystallite surface area) and $I_{LO} \sim \ell^3$ (crystallite volume), then $I_A/I_{LO} \sim \ell^{-1}$. This is strong evidence that A is in some way associated with the crystallite/amorphous interface regions.

6.5 BRIEF SYNOPSIS OF THE EXPERIMENTAL FINDINGS ABOUT A

Thus far, we have presented summaries of data pertaining to the new feature A. The studies have included data over a wide range of implant fluences, with various ion energies and species. The experimental results are summarized as follows:

(1) A new, strong feature has been observed in the Raman spectrum of ion-implanted GaAs.

(2) It has constant line shape, is fairly narrow, and the frequency shifts very little over the large range of damage studied.

(3) It is absent in c-GaAs.

(4) It is absent in a-GaAs.

(5) It is absent in AlGaAs crystals.

(6) The intensity depth profile of the new feature within the damage layer is the same as the a-GaAs spectral-component intensity.

(7) It is strongly resonant near the E_0 / $E_0 + \Delta_0$ broadened interband transition, which is in strong contrast to the crystalline allowed LO line, which resonates near E_1.

(8) $I_A / I_{LO} \sim \ell^{-1}$.

6.6 DISCUSSION OF THE ORIGIN OF A

It is convenient to make a list of hypotheses pertaining to the fundamental nature of the new band.

(A) Maxima in the vibrational DOS, including micro-crystallite size effects.

(B) Acoustic vibrations made Raman active via Brillouin zone folding in these microcrystalline systems.

(C) Impurity-specific vibrations.

(D) Damage-induced native defects.

(E) Crystallite surface modes.

(F) Vibrations specific to the crystal/amorphous interface.

(G) Defect-assisted scattering of GaAs acoustic phonons.

Let us discuss the expected nature of each of these in light of the experimental results presented. (A): The frequency of A lies in the range of acoustical vibrations in c-GaAs [Waugh & Dolling, Dorner & Strauch]. The lowest-frequency critical point in the phonon (DOS) is the transverse acoustic band at the L point in the Brillouin zone, $\omega_{TA}(L) = 60\ cm^{-1}$. TA(X) and TA(K) critical points have frequencies at approximately 80 cm^{-1}. The longitudinal acoustic (LA) critical points occur between 210 and 230 cm^{-1}.

When the crystal to microcrystal transition occurs, some distortion of the vibrational dispersion bands is expected due to finite-size effects. It is expected that this would primarily affect the long-wavelength vibrations. The dispersion of the long-wavelength optical phonons is not strongly affected, based upon the success of the spatial correlation model in dealing with these modes [Tiong et al.]. For TA(L), $\lambda = 4a_0/\sqrt{3}$ which is small compared to the crystallite size. A distortion of 20% in the frequencies of the acoustical bands is therefore

unlikely. Another cause of distortion in the phonon DOS is the effect of crystallite boundary conditions [Pathria]. For small enough ℓ the Born-von Karman periodic boundary conditions no longer apply. This leads to modifications in the DOS which are strongly dependent on the crystallite size. We do not observe this in A: the frequency does not change for a variety of implant conditions, corresponding to different crystallite sizes. If A is an intrinsic c-GaAs vibration made active in the implanted material, we then conclude that $0 < k_p < k_{BZ}$.

(B): Zone-folding activates non-zone-center acoustic phonons in both crystalline GaAs/AlAs heterostructures [Sapriel et al.] and in amorphous heterostructures [Santos et al.]. While we do not have real order in our implanted GaAs, vibrational features may be affected by the apparently consistent texture of the scattering medium, although only in a statistical sense. However, the superlattices show Raman-active acoustic modes, present due to zone folding, with frequencies which vary as the reciprocal quantum well period. Since A has a nearly constant frequency, this is not a possibility.

Impurity-specific vibrations (C) are clearly eliminated by the fact that we observe A in different implants.

Native defects (D) resulting from the ion damage

(e.g. intersititals, vacancies, anti-site defects, etc. [Barker & Sievers]) are expected to be in high density. However, the low frequency of the A band, well within the fundamental phonon regime of GaAs, serves as an arguement against assigning it to a defect mode. Resonance with modes within the fundamental band would delocalize specific defect vibrations, broadening them beyond recognition (especially at room temperature). In contrast, we observe a well- defined peak.

The observation of a spectral feature present only in the mixed amorphous/microcrystalline phase characteristic of the ion-implanted material, but absent in either pure phase (c-GaAs, a-GaAs), clearly suggests a mechanism that involves the surfaces (E) or crystal/amorphous interface regions (F). Vibrational modes attributed to such interface regions have several attractive features for our purposes: the frequency would be constant and their number would increase in proportion to the internal surface area, $S/V \sim \ell^{-1}$. Over nearly one order of magnitude we observe that $I(A) \sim \ell^{-1}$, as shown in Fig. 6.11, with approximate crystallite sizes obtained from the LO line [Tiong et al.]. However, such modes have the same degeneracy with the fundamental vibrations as (D), and are therefore expected to be quite broad.

Critical findings are our observations of the

resonance behavior of A, and the great difference between this resonance and that exhibited by the allowed LO line. A resonates near E_0 and <u>not</u> near E_1. The LO line resonates near E_1 and <u>not</u> near E_0. The LO phonon Raman resonance is well accounted for in terms of the relative k-space volumes involved.

We do not expect symmetry to play a strong role in the resonance of these features because long-wavelength excitations (i.e. near the Γ point) will experience strong interactions with the disorder: long-range symmetry becomes less imposing with smaller crystallite size. The crystallite size is not simply affecting the acoustic vibrational spectrum, as it does the LO band, to permit sharp acoustic-phonon scattering. We know this because the LO peak shifts dramatically over our range of damage and the LO band has weak dispersion, A shifts little for abruptly changing acoustic phonon dispersion. Furthermore, the LO line and the A band would also possess the same resonance profiles.

Perhaps the large spatial extent of the electronic wavefunctions is a requirement for the effect we observe. Electrons with short wavelengths will not be strongly affected by the crystallite size. For $\hbar\omega < 2.2$ eV the uppermost valence bands and lowest conduction band [Cohen & Chelikowsky], near the E_0 and $E_0 + \Delta_0$ peaks in the DOS,

which are responsible for the overall optical properties in this energy regime, require that $|\mathbf{k}| \lesssim 0.2\ k_{BZ}$ ($\lambda \gtrsim 10\ a_0$). For the E_1 transition $|\mathbf{k}| > 0.3\ k_{BZ}$. Hence, electrons near the Γ point in the Brillouin zone would be strongly influenced by the microscopic nature of the disorder.

We therefore propose a mechanism for the strong scattering of GaAs acoustic phonons via a defect-assisted scattering mechanism (G). The "defects" in this case are the microcrystal/amorphous interface, or "surface" regions, which are present in implanted GaAs. The population of such defects is consistent with $I_A/I_{LO} \sim \ell^{-1}$. Such a defect elastically scatters the photon-excited electron, resulting in a momentum transfer. This transfer of momentum results in a breakdown of the $\mathbf{k} = 0$ infinite-crystal selection rule, imposed by long range order. The electron may then scatter with non-zone-center phonons. Electrons and phonons with similar wavelengths are expected to interfere strongly. Such resonances give rise to "special" points within the Brillouin zone (away from $\mathbf{k} = 0$) which are allowed to participate in first-order Raman scattering due to the defect-mediated process.

6.7 DEFECT-ASSISTED RAMAN SCATTERING

A prominent defect-assisted scattering analysis derives from two-phonon scattering [Zeyher] by replacing

one of the electron-phonon interactions with an elastic electron-impurity collision. This additional event acts to alter the electronic $\hbar$ vector, relaxing the strict $\hbar$ selection rules imposed by long-range crystalline order. The scattering process is fourth order involving electron (hole) scattering with the LO phonon and an extra elastic scattering event between an electron (hole) and the impurity, along with the usual photon absorption and emission. The process is formally the same as two-phonon scattering in semiconductors [Gogolin & Rashba].

Following the summary of the treatment of Berg and Yu [1987], the defect-assisted scattering is developed considering only two-band processes with parabolic bands. Excitonic effects are ignored and the Born approximation is used. Scattering cross-sections then take on the form

$$\sigma(\omega_L) \sim \int_{BZ} q^2 dq \mid f(q,\omega_L,\omega_s)\, A_T(q,\omega_L) \mid^2 \qquad (6.5)$$

where f is a function which accounts for the mechanisms involved in the electron-phonon scattering (e.g. deformation potential, Fröhlich interaction, etc.) and in the electron-impurity scattering. The function A_T accounts for the scattering processes involved in this fourth-order perturbation expansion. A_T incorporates all scattering permutations of both electrons and holes:

$$A_T(\omega_L) = A(s_e x,-s_e x,x_1,x_2,x_3) + A(s_h x,-s_h x,x_1,x_2,x_3)$$
$$- A(s_e x,s_h x,x_1,x_2,x_3) - A(s_h x,s_e x,x_1,x_2,x_3)$$
$$+ A(s_e x,-s_e x,x_1,x'_2,x_3) + A(s_h x,-s_h x,x_1,x'_2,x_3)$$
$$- A(s_e x,s_h x,x_1,x'_2,x_3) - A(s_h x,s_e x,x_1,x'_2,x_3) \qquad (6.6)$$

where

$$A(\lambda_1 q,\lambda_2 q,k_1,k_2,k_3) = \frac{\lambda_1}{\lambda_1 + \lambda_2} A(0,\lambda_1 q,S^{\frac{1}{2}},k_2,k_1)$$
$$+ \frac{\lambda_2}{\lambda_1 + \lambda_2} A(0,\lambda_2 q,S^{\frac{1}{2}},k_2,k_3)$$

$$A(0,\lambda_2 q,k_1,k_2,k_3) = \frac{16\pi^2}{(k_1^2 - k_2^2)\lambda_2 q}$$
$$\times \left\{ \tan^{-1}\left[\frac{i\lambda_2 q}{k_1 + k_3}\right] - \tan^{-1}\left[\frac{i\lambda_2 q}{k_2 + k_3}\right]\right\}$$

with

$$x = aq, \quad x_j = ak_j, \quad x'_2 = ak'_2, \quad a = \left[\frac{\hbar^2}{2\mu\hbar\omega_{L0}}\right]^{1/2}$$

$$k_j = \left[\frac{2\mu}{\hbar^2}\{\hbar\omega_L + i\eta - E_c - (j-1)\hbar\omega_P - \delta_{j2}\hbar^2 q^2/2M\}\right]^{1/2}$$

$(j = 1,2)$

$$k_3 = \left\{ \frac{2\mu}{\hbar^2}\{\hbar\omega_L + i\eta - E_c - \hbar\omega_P\} \right\}^{1/2}, \qquad Im(k_3) > 0$$

$$k_2' = \left\{ \frac{2\mu}{\hbar^2}\{\hbar\omega_L + i\eta - E_c - \hbar^2 q^2/2M\} \right\}^{1/2}, \qquad Im(k_2') > 0$$

along with the following definitions

$$M = m_e + m_h \;, \quad s_{e,h} = m_{e,h} / M \;, \quad \frac{1}{\mu} = \frac{1}{m_e} + \frac{1}{m_h}$$

$$S = \frac{\lambda_1 k_3^2 + \lambda_2 k_1^2}{\lambda_1 + \lambda_2} - \lambda_1 \lambda_2 q^2$$

with the physical quantities

$m_{e,h}$ = electron, hole effective masses

E_c = critical-point energy

η = energy width of the E_c transition

The λ's are replaced by the appropriate $s_{e,h}$ in Eq.(6.6). The cross-section in Eq.(6.5) may then be approximated numerically, once the scattering mechanisms f have been identified.

Menéndez and Cardona observed impurity-assisted LO phonon scattering (Fröhlich) near $E_0 + \Delta_0$ in GaAs. The dopant impurities were allowed to interact with the electrons (holes) via a screened-Coulomb potential

$$V(k) = \frac{4\pi e^2}{\epsilon_0 (k^2 + k_F{}^2)} \qquad (6.7).$$

k_F is determined by the mean distance between defects. The LO scattering was via the Fröhlich mechanism introducing an additional 1/k factor [Fröhlich]. Thus, Eq.(6.5) becomes

$$\sigma(\omega_L) \sim \int_{BZ} \frac{dq}{(q^2 + q_F{}^2)^2} \mid A_T(q,\omega_L) \mid^2 \qquad (6.8)$$

The additional scattering event caused the system to show double-resonance effects with the largest contribution to the scattering intensity coming from phonons with $k \approx 0.2/a_0$ (a_0 is the lattice constant). Their calculated results [Menéndez & Cardona] were in good agreement with experimental results. Of particular interest is the fact that strong double-resonance effects were seen for phonons with k large compared to k_F and k large compared to $k_i = 2\pi n(\lambda_L)/\lambda_L + 2\pi n(\lambda_s)/\lambda_s$, the (backscattering) wavevector required for intrinsic double-resonance scattering.

Berg and Yu [1987] extended the Menéndez-Cardona results to the case of a variety of defects in electron- and neutron-irradiated GaAs. They discuss the generalization of the fourth-order scattering process near E_0. For defect vibrations which may be treated as local modes they find that double-resonance scattering comes

primarily from a narrow range of k values around $0.1/a_0$.

In the cases of the defect-assisted Raman scattering cited above, the vibrations were considered to be dispersionless. Taking the A band as resulting from intrinsic c-GaAs vibrations requires that these are acoustic vibrations. $\mathbf{k} = 0$ acoustic vibrations have Γ_5 symmetry in the zincblende crystal structure [Hayes & Loudon, p.98]. Group compatibility tables along symmetry directions [Parmenter] indicate that acoustic vibrations with $\mathbf{k}$ between Γ and X points in the Brillouin zone have Raman tensors consistent with Eq.(6.1). However, the caveat of selection rule breakdown near resonance must be given full consideration [Hayes & Loudon, p.191]. For scattering involving acoustic phonons, frequencies change radically over the Brilloiun zone. The dispersion must therefore be accounted for when scattering by acoustic phonons is considered. This is done in the following using the actual acoustic bands [Waugh & Dolling].

For electron-phonon scattering when the phonons are acoustic the deformation potential (DP) has the (long-wavelength) form

$$H_{DP} = D \left(\frac{\hbar}{2MN\omega(q)} \right)^{1/2} \hat{\xi} \cdot \mathbf{q} \; \rho(q) \; (a_{-q}^{\dagger} + a_{q}) \tag{6.10}$$

[Mahan, Hayes & Loudon] where D is the deformation

"constant," $\hat{\xi}$ is the phonon polarization unit vector, $a_q^\dagger$ (a_q) is the phonon creation (annihilation) operator with wavevector q, and $\rho(q)$ is the k-space electron density operator (between states k and $k + q$). For electron-phonon scattering via the piezoelectric effect (PE)

$$H_{PE} = i \left[\frac{\hbar}{2MN\omega(q)}\right]^{1/2} M(\hat{q})\, \rho(q)\, (a_{-q}^\dagger + a_q) \tag{6.11}$$

[Mahan, Hayes & Loudon] where the geometrical function M describes the strain-induced electric fields; M depends only on the direction of q. GaAs is only weakly piezoelectric. In the present notation the Fröhlich Hamiltonian is

$$H_F = \frac{C}{V} \frac{\hat{\xi}\cdot\hat{q}}{q}\, \rho(q)\, (a_{-q}^\dagger + a_q) \tag{6.12}$$

[Mahan] where C is the Fröhlich constant. The $1/q$ dependence used in Eq.(6.8) for Fröhlich scattering by LO phonons is now evident from Eq.(6.12). The Hamiltonians in Eqs.(6.4 - 6.6) are long-wavelength Hamiltonians. Generalization to any point in the Brillouin zone is not easily obtained. In spite of this constraint we shall

nevertheless attempt to analyze the nature of several resonances under these conditions.

In Eq.(6.5) the different contributions to the scattering cross-section have been squared then integrated over k space, appropriate for intrinsic scattering mechanisms. For extrinsic scattering, integration must be performed first (reconstructing the Fourier contributions for a single scattering event involving components from the entire Brillouin zone), then the result is squared.

As mentioned earlier, in the context of the LO phonon Raman resonance shown in Fig. 6.6, the E_1 and $E_1 + \Delta_1$ crystalline interband transitions merge into a single, broad band in these implanted samples. It is reasonable to expect that a similar situation holds for the E_0 and $E_0 + \Delta_0$ transitions near the Γ point. The critical point energy E_c would be near the average energy with a band width $\eta \approx \Delta_0$.

The electron-impurity interaction responsible for the observed effect, for which it is proposed that the electronic wavefunction wavelength is an important parameter, must be sufficiently general to explain the observation of A in all implants studied. The view taken here is that the defects are the amorphous/crystalline interface regions. Because of the success had in describing the LO lineshape and frequency behavior, the

spatial confinement model is a good starting point for describing the electron-impurity scattering within the crystallites. The k-space confinement function modifies a Bloch wavefunction with wavevector $\mathbf{k}_0$ in the crystal via

$$C(\mathbf{k},\mathbf{k}_0) \sim \frac{\ell}{(2\pi)^{3/2}} \; e^{-|\mathbf{k}-\mathbf{k}_0|^2 \ell^2/8} \tag{6.13}$$

where ℓ is the crystallite "diameter" [Richter]. It is sufficient, in this analysis, to simply impose this elastic scattering, which serves only to alter the electronic wavevector breaking the $\mathbf{k} = 0$ restriction.

In section 6.3 it was discussed how the LO phonon may resonate with a single peak in the electronic DOS, corresponding to the merged E_1 and $E_1 + \Delta_1$ direct transitions near 3 eV, as observed in reflectance measurements. It is reasonable to assume that a similar effect takes place near E_0 and $E_0 + \Delta_0$. Such a feature would be broad, having an energy width of $\approx \Delta_0$. Thus, a single critical point energy is believed to be responsible for the resonance of A at an energy between these two crystalline maxima in the DOS.

In Fig. 6.8 we show a two-band resonance-Raman cross-section calculated from Eq.(6.5). The curve is for the merged E_0 and $E_0 + \Delta_0$ case, with $E_c = 1.65$ eV to fit the data. The electron-impurity scattering is described by

Eq.(6.13) with $\ell = 10a_0$ from the LO phonon [Tiong]. The electron-phonon scattering is via the deformation potential, Eq.(6.10). Equation (6.5) then becomes

$$\sigma(\omega_L) \sim \left| \int_{BZ} q^2 dq \, \frac{q}{\omega(q)^{1/2}} \, C(q,0) \, A_T(q,\omega_L) \right|^2 \qquad (6.14)$$

where integration is carried out first (extrinsic). The resulting σ was insensitive to the order of integration and squaring. Parameters used in evaluating Eq.(6.14) are listed in Table II.

Agreement between the calculated cross-section and the data is only satisfactory. The primary contribution to the scattering comes from $k \approx 0.1\ k_{BZ}$. Similar agreement is found when considering electron-acoustic phonon scattering via the piezoelectric effect, Eq.(6.11). Since GaAs is weakly piezoelectric, the deformation potential is more likely. In any case, we find some consistency between the data and the model.

Many other scattering scenarios were considered, some of which are shown in Fig. 6.12, along with the curve in Fig. 6.8 and the averaged data values. It is important to note that with critical-point energy widths closer to the crystalline values of $\eta \approx 0.1$ eV [Gopalan et al.], Eq.(6.14) results in sharp cross-sections. This is in contrast to the data which is relatively broad, supporting

the merged band picture.

TABLE 6.1: Polarization of Raman spectrum main features.

	$z(x,x)\bar{z}$	$z(x,y)\bar{z}$	$z(x',x')\bar{z}$	$z(x',y')\bar{z}$
LO	vw	s	s	vw
A	vs	w	s	0
a-GaAs	s	m	s	m

TABLE 6.2: Room Temperature GaAs Constants

Lattice constant $a_0 = 5.64$ A [B]

$M_{Ga} = 69.720$ amu $M_{As} = 74.922$ amu [B]

$m_c = 0.063\ m_0$ [B]

$m_{hh} = 0.50\ m_0$ $m_{lh} = 0.088\ m_0$ $m_{soh} = 0.15\ m_0$ [B]

$E_0 = 1.423$ eV $\Delta_0 = 0.341$ eV [B]

$\eta = 0.1$ eV [G]

$E_G = 1.65$ eV

$\omega_{LO} = 292\ cm^{-1}$ $\ell = 10\ a_0$ $k_f = 0.2/a_0$

B - J.S.Blakemore, J. Appl. Phys. 53, R123 (1982).

G - S.Gopalan, P.Lautenschlager, and M.Cardona, Phys. Rev. B 35, 5577 (1987).

FIGURE CAPTIONS

Fig. 6.1 : Unpolarized, room temperature Raman spectra for (100)-oriented GaAs crystals and for crystals implanted with 45-keV Be^+ ions to various fluences, measured in ions/cm^2. Excitation was with 6471 A light. Intensities are all on the same (arbitrary) scale relative to CaF_2. Note the peak labeled A.

Fig. 6.2 : Photon energy dependence of the (R.T.) Raman spectrum of the 5 x 10^{14} cm^{-2} 45-keV Be^+ implanted sample. The (arbitrary) vertical scale is the same for all spectra (CaF_2 reference), except for the 7525 A spectrum which is scaled <u>down</u> by a factor of two.

Fig. 6.3 : Raman spectra (R.T.) for implanted GaAs specimens varying implant species and energies: (a) 5 x 10^{14}-cm^{-2} 180-keV Be^+, (b) 2 x 10^{13}-cm^{-2} 180-keV Si^+, (c) 5 x 10^{14}-cm^{-2} 45-keV Be^+, and (d) 5 x 10^{14}-cm^{-2} 180-keV Si^+. Also (e): amorphous GaAs. The excitation is 6471-A light. Note the strong presence of A in all spectra but the a-GaAs. All intensities are relative to CaF_2.

Fig. 6.4 : Polarization analyses of the full fundamental phonon regime. Excitation is with 6471-A, 1.91-eV red light.

Fig. 6.5 : Intensity measurements (relative to CaF_2) of the a-GaAs component of the Raman spectrum of 5 x 10^{14} cm^{-2} implants for three implant species. The smooth curve is optical penetration depth using Eq.(6.2) for 75% crystalline / 25% amorphous.

Fig. 6.6 : LO scattering intensity measurements (normalized to I_a in Fig. 4) for the same three implanted samples in Fig. 4. The rise for higher photon energies is due to resonance with the E_1 inter-band electronic transition near 3 eV. The curve is from Eq.(6.4). The scattering efficiency is constant below 2 eV.

Fig. 6.7 : Reflectance measurements throughout and above the photon energy range studied, for the crystal and the implants of Figs. 6.5, 6.6, and 6.8.

Fig. 6.8 : Intensity measurements of A (normalized to I_a, the a-GaAs intensities in Fig. 4) for the same implants shown in Figs. 4 and 5. Note the strong resonance near 1.7 eV (not observed in

the LO line) and the rapid drop at high photon energies.

Fig. 6.9 : Comparison of the intensity and frequency of A to the ion fluence for silicon- and beryllium-implanted at 180 keV into GaAs.

Fig. 6.10: Photon-energy dependence of the frequency of the A band for the three implants studied in detail.

Fig. 6.11: Dependence of the intensity of A on the crystallite size.

Fig. 6.12: Various calculated fourth-order scattering cross-sections. The filled-in circles are (average) data points from Fig. 6. The solid curve is for the merged E_0 and $E_0 + \Delta_0$, using the deformation potential (DP) and spatial confinement, Eq.(6.14). $\ell = 10a_0$ is from the LO phonon data. The dense dash curve is from Eq.(6.8), as in [Menéndez & Cardona]. The long and short dashes are for a local mode vibration [Berg & Yu]. The sparse dash curve is obtained as in the solid curve, except for single-crystal electronic band widths. In all curves E_c = 1.65 eV.

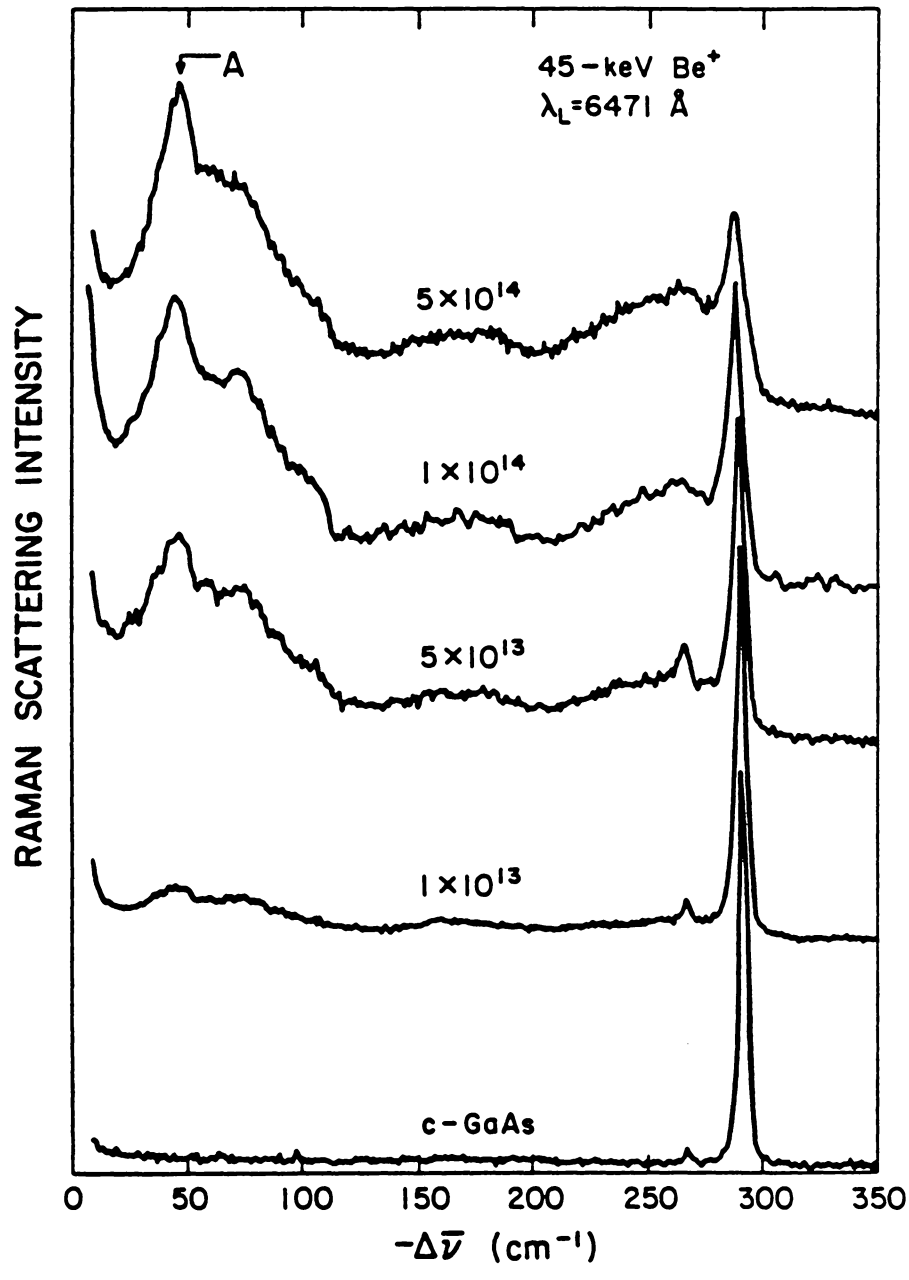

Fig. 6.1 45-keV Be^+ implant sequence ($\hbar\omega_L$ = 1.91 eV).

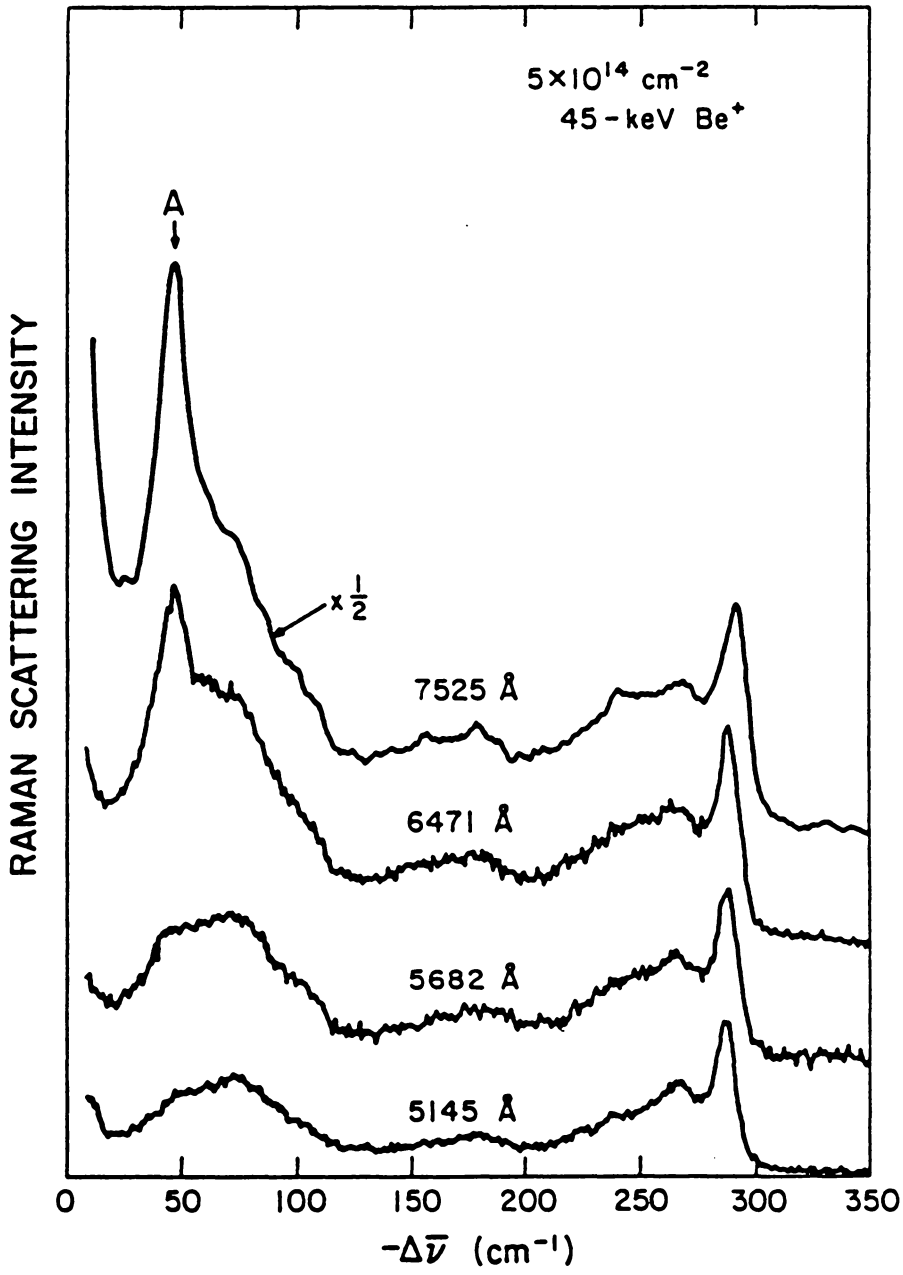

Fig. 6.2 $\hbar\omega_L$ dependence of Raman spectrum.

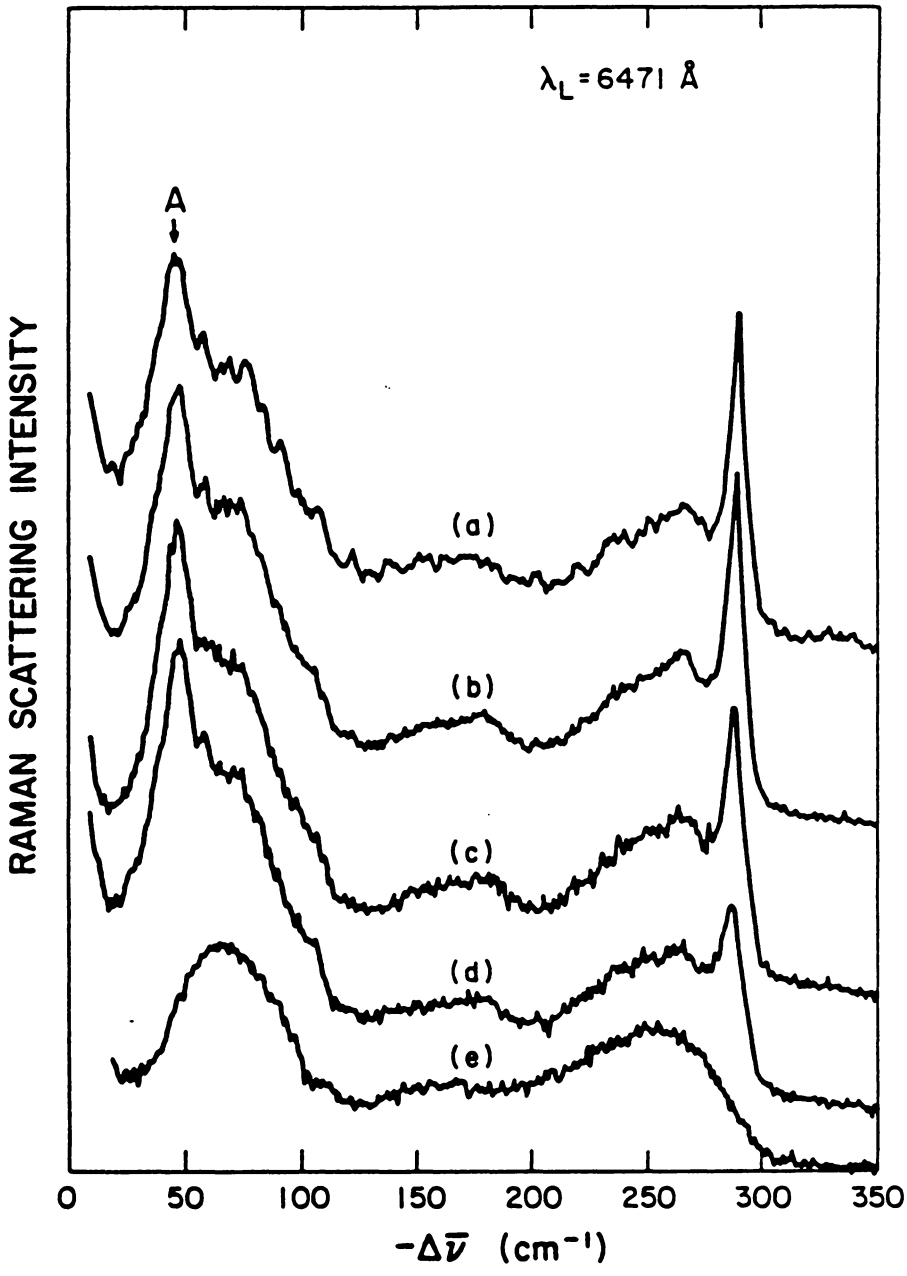

Fig. 6.3 Comparison of different implants and a-GaAs.

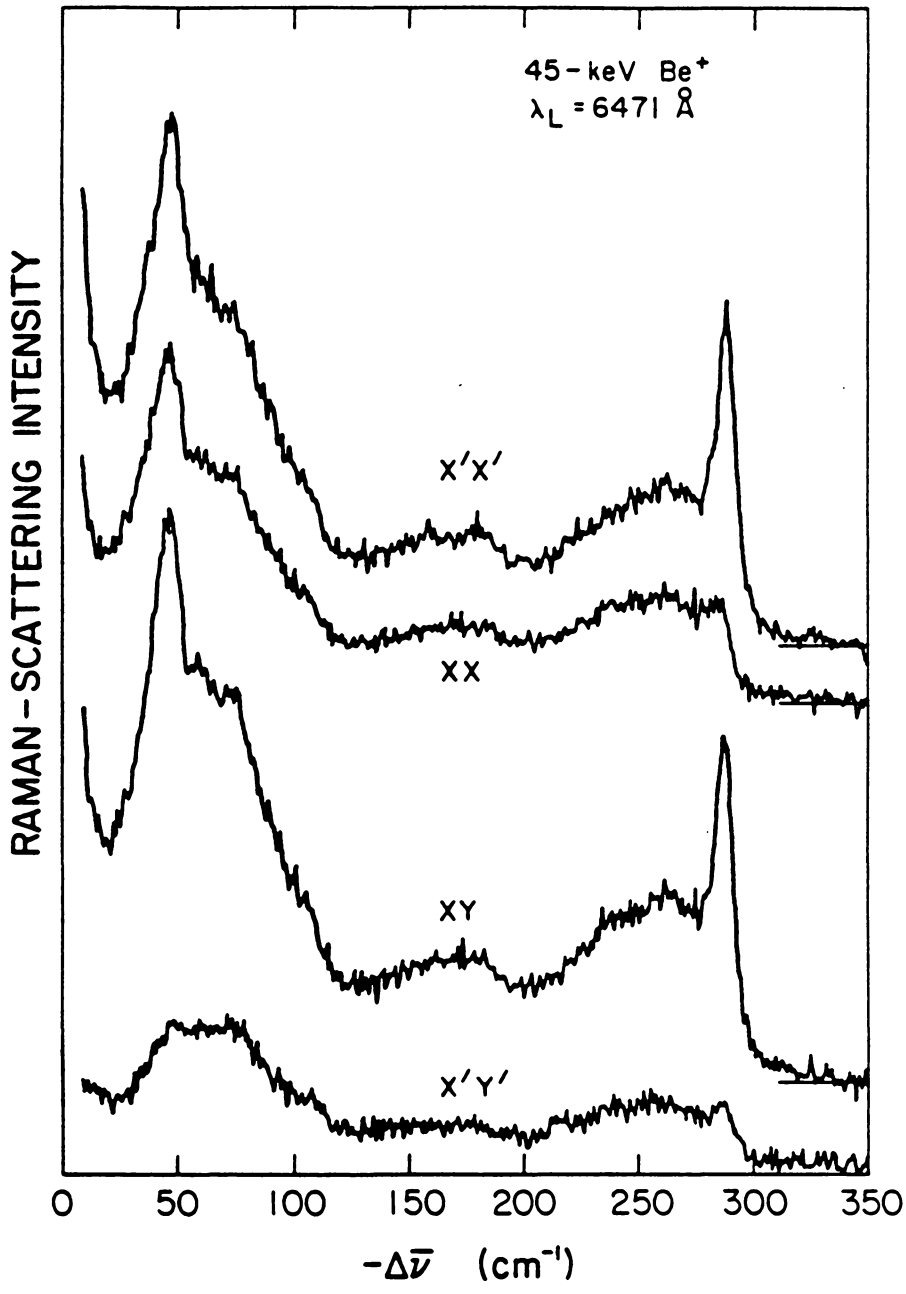

Fig. 6.4 Polarization breakdown with $\hbar\omega_L$ = 1.91 eV.

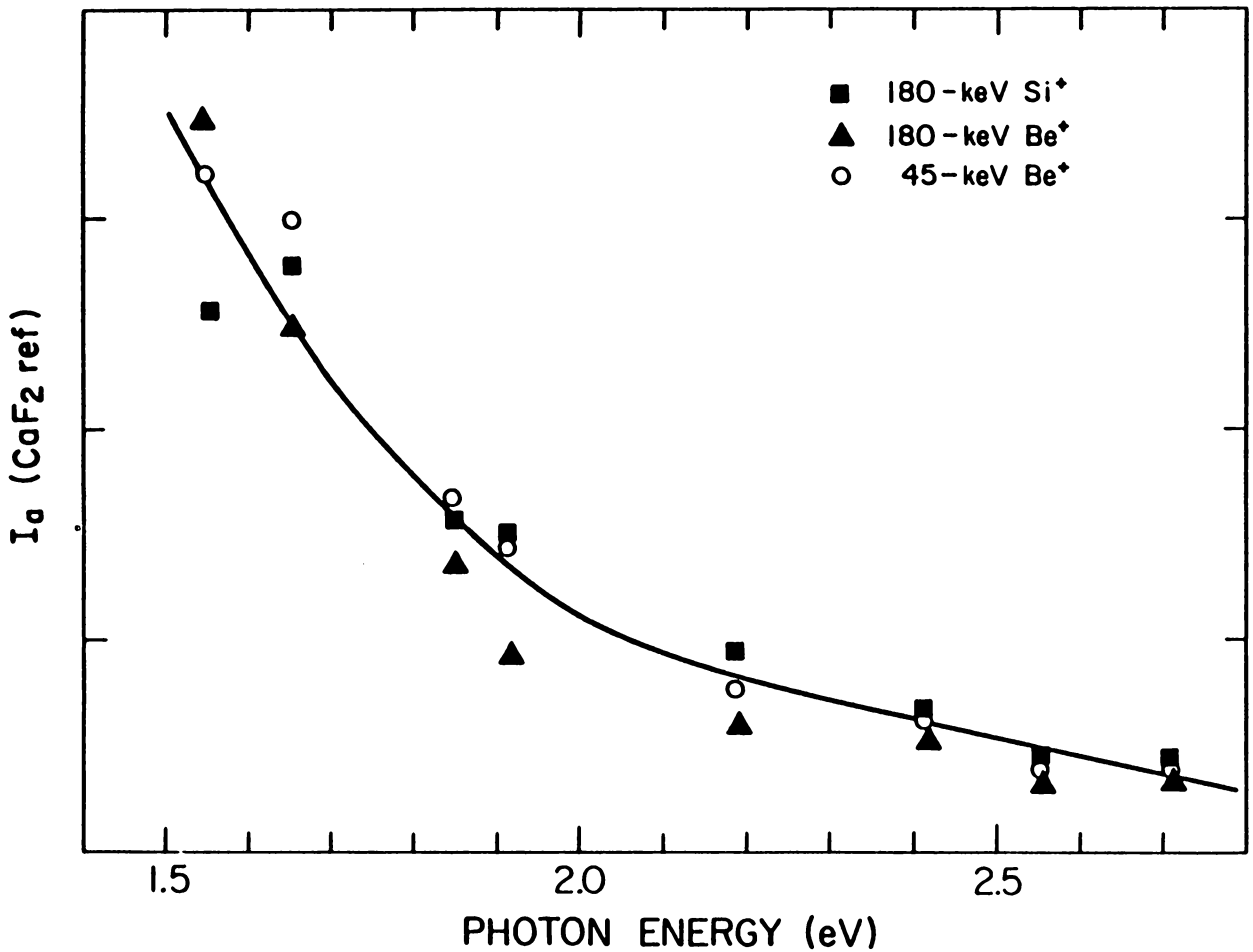

Fig. 6.5 Measured a-GaAs component intensities vs. $\hbar\omega_L$.

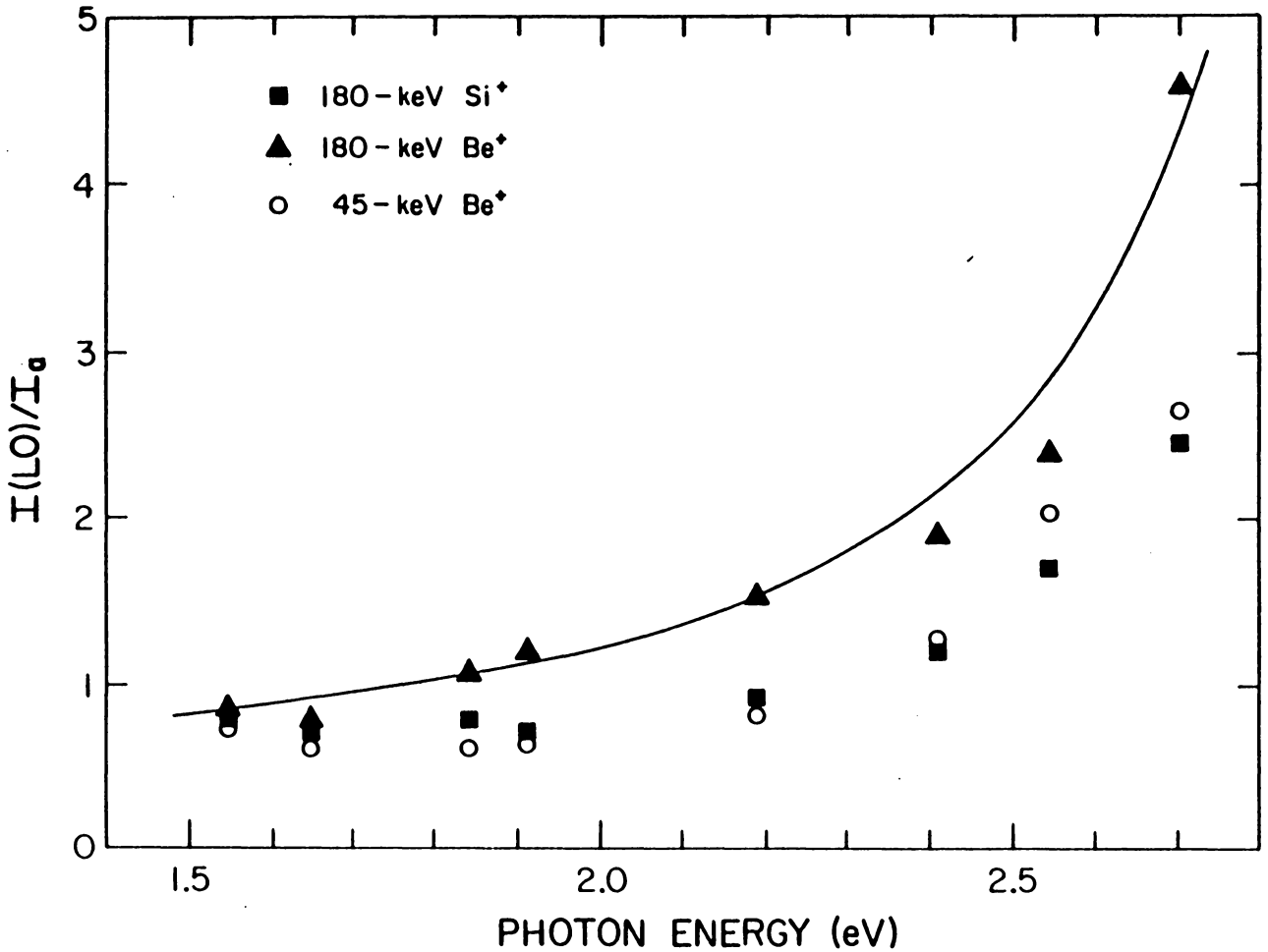

Fig. 6.6 LO line intensities (per unit volume) vs. $\hbar\omega_L$.

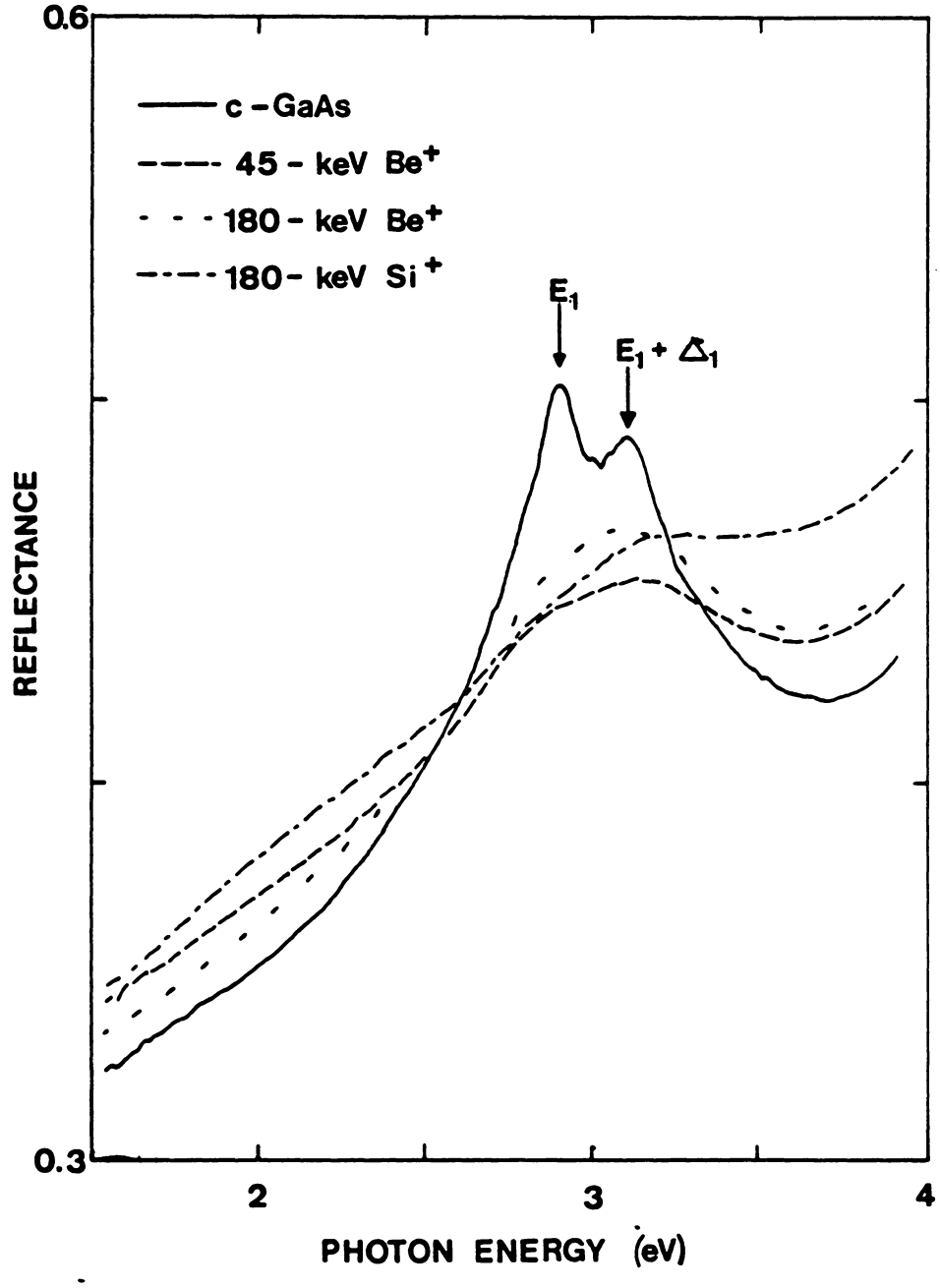

Fig. 6.7 Reflectance spectra for three main implants.

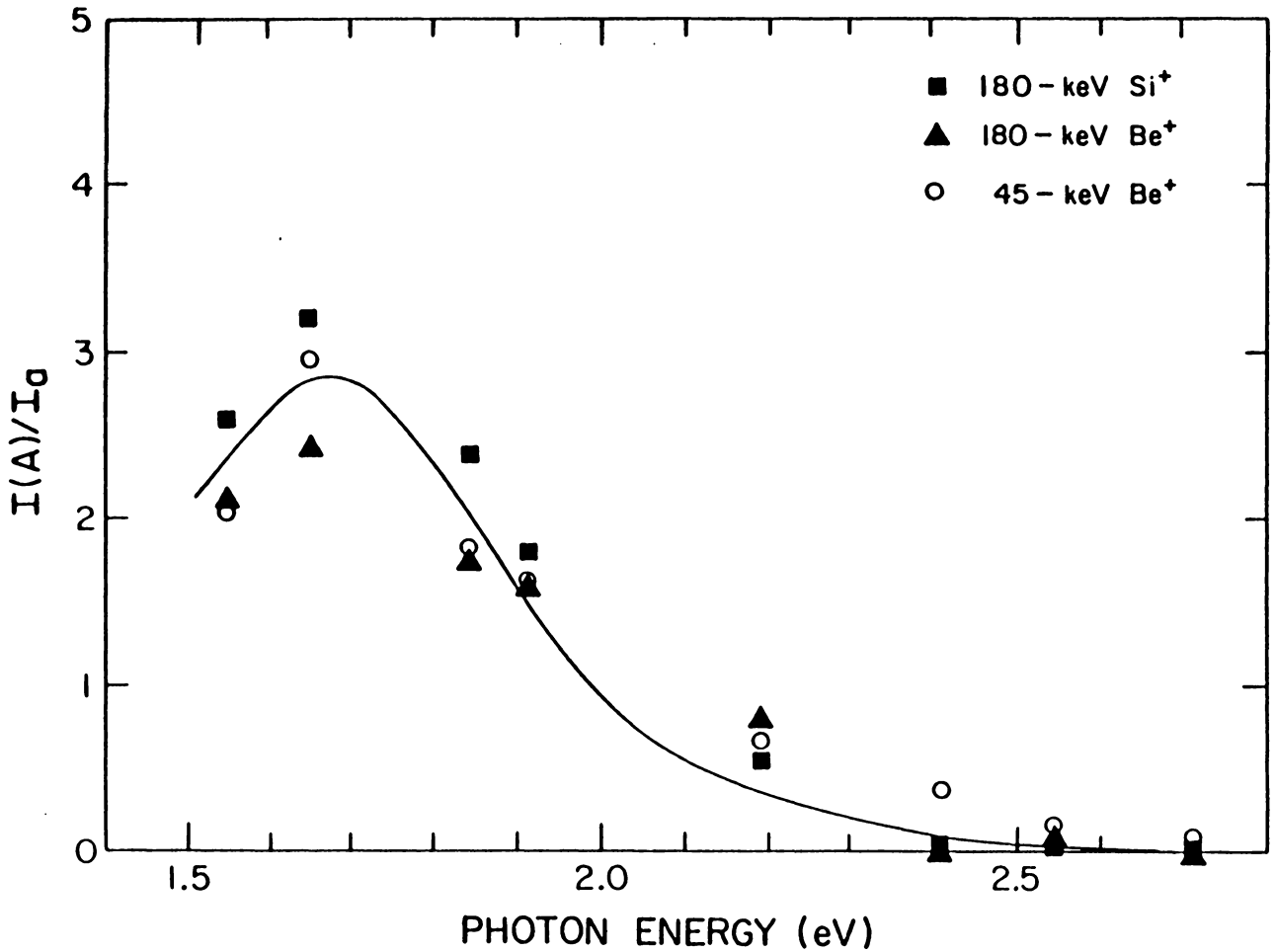

Fig. 6.8 Intensity of A (per unit volume) vs. $\hbar\omega_L$.

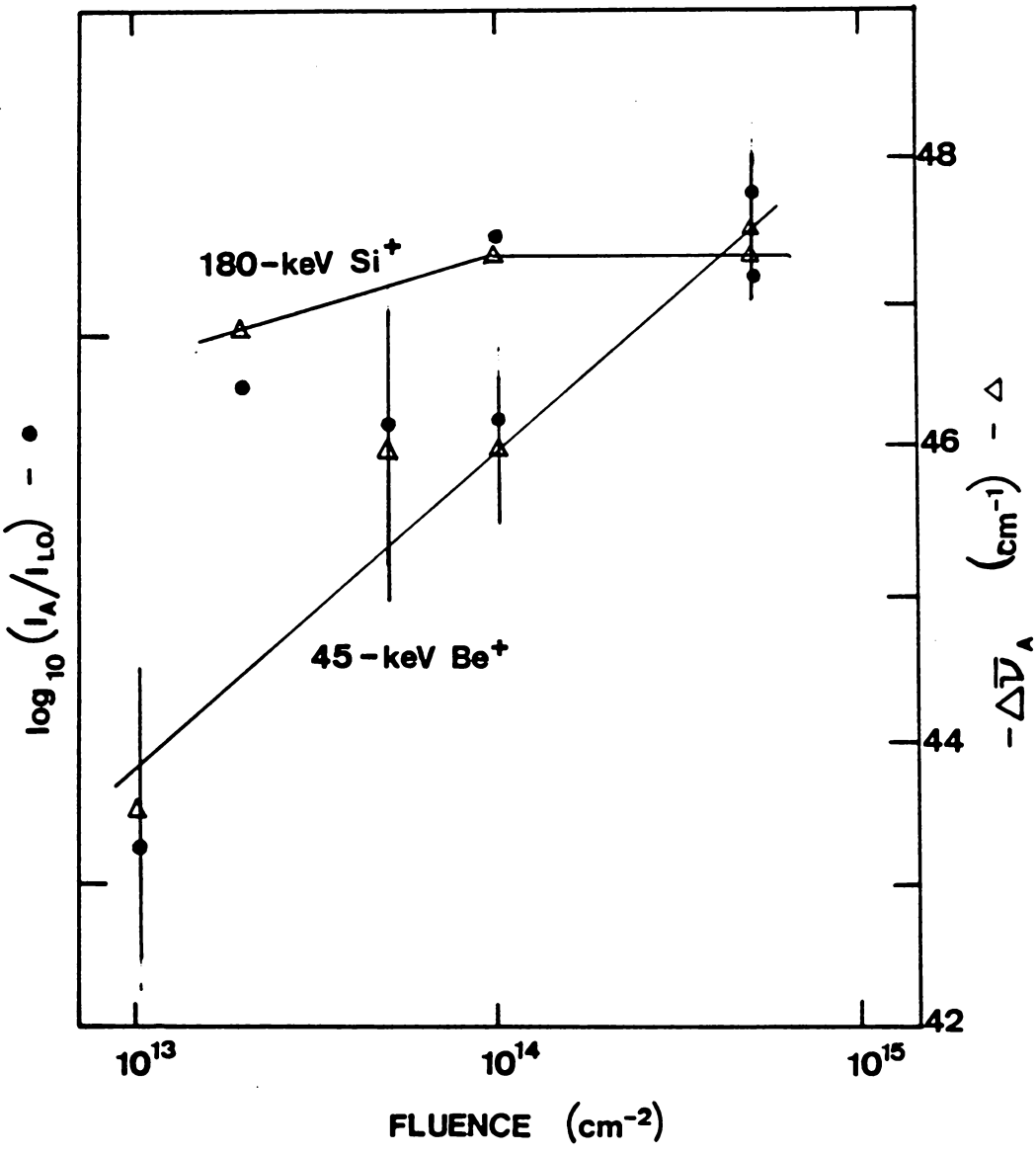

Fig. 6.9 Intensity and frequency of A vs. implant fluence.

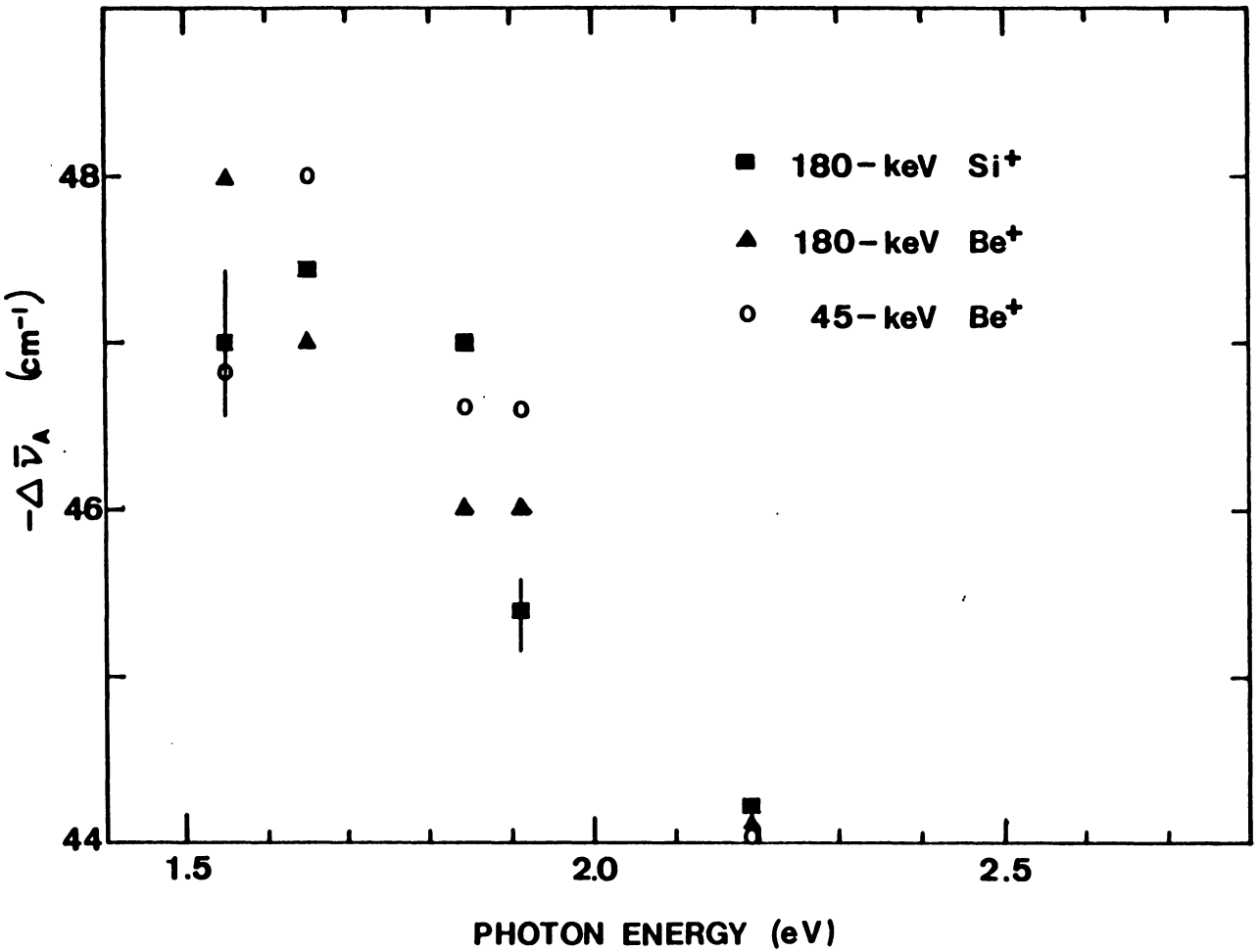

Fig. 6.10 Frequency of A vs. $\hbar\omega_L$.

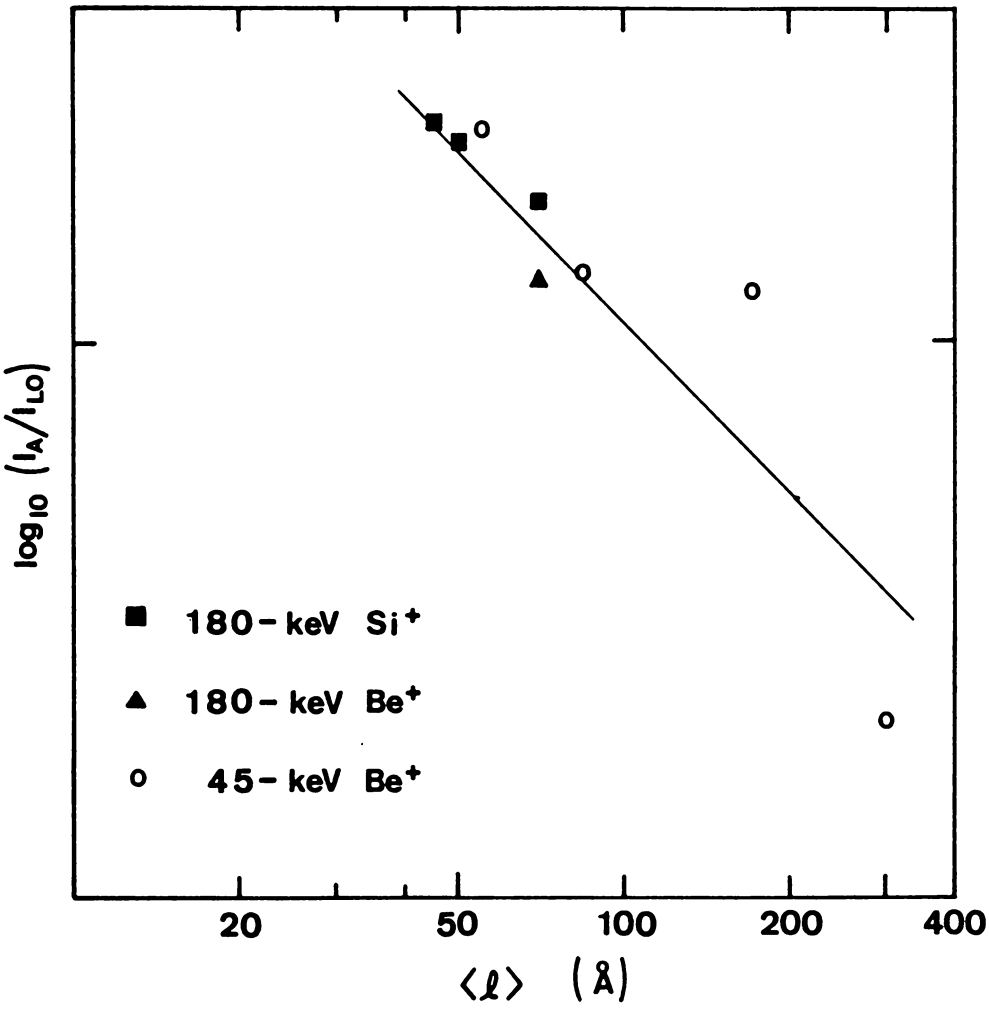

Fig. 6.11 Intensity of A vs. crystallite size.

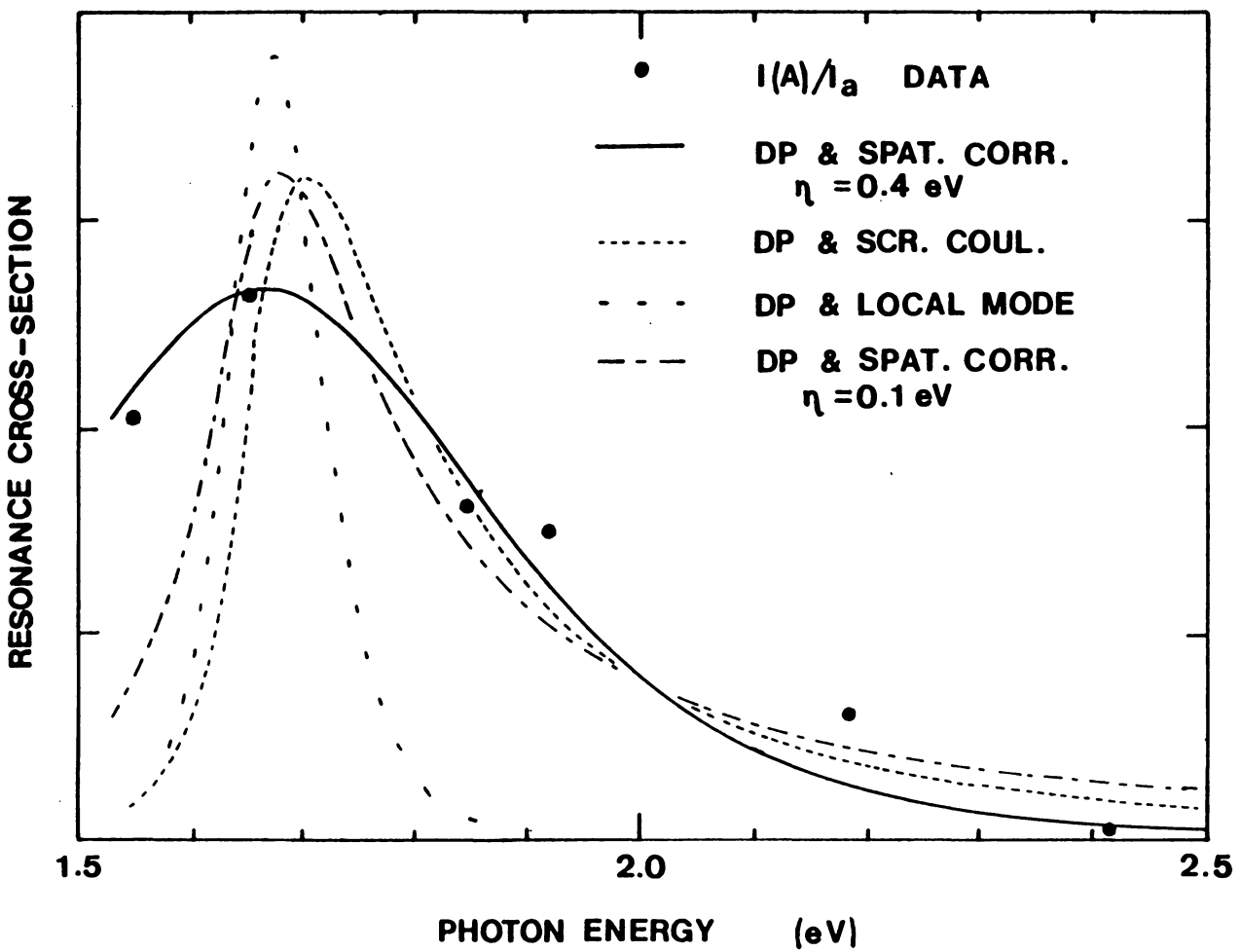

Fig. 6.12 Various defect-assisted cross-sections vs. $\hbar\omega_L$.

CHAPTER 7: SILICON LOCAL MODES IN GaAs: THE ROLE OF AMORPHICITY

7.1 INTRODUCTORY REMARKS

In this chapter studies of the substitutional impurity atoms, introduced by the implanting process, are outlined. These Raman-scattering studies were carried out both prior to and following anneals. Silicon is the primary dopant used to produce n-type GaAs. The silicon is introduced into the GaAs via either Si^+ or SiF_3^+ implantation. The SiF_3^+ species has a much larger flux, so that the implant time for a given fluence is greatly reduced. A 10^{16} cm^{-2} SiF_3^+ implant is achieved in 24 min., while the same fluence is reached with Si^+ in 187 min. As discussed in Ch. 3, the SiF_3^+ ion will result in higher damage levels and shallower ranges than Si^+ ions having the same energy. The implant sequences shown in Figs. 3.3 and 3.6 compare the Raman spectra for the two different implants discussed here.

7.2 AMORPHIZATION AND RECOVERY OF THE GaAs LATTICE

Figure 7.1 compares the effects of implantation with SiF_3^+ and with Si^+, for a fluence of 10^{16} ions/cm^2 with ions of energy 120 keV. Figs. 7.1(c) and 7.1(a) show the spectra of samples implanted with SiF_3^+ and Si^+,

respectively, while Figs. 7.1(d) and 7.1(b) show the corresponding spectra observed after the samples were annealed (12 sec RTA).

The first-order overall conclusion evident from Fig. 7.1 is the qualitative similarity of the results obtained with SiF_3^+ to those obtained with Si^+. Both implanted samples exhibit the broad bands of amorphous GaAs coexisting with the LO line of a microcrystalline component. After annealing, the amorphous bands essentially disappear, the LO line sharpens, and a sharp TO line appears. All four spectra also reveal weak features near 400 cm^{-1} (shown expanded in Figs. 7.2 and 7.3) which, as described in the following section, correspond to silicon local modes. No evidence of fluorine local modes was found in the SiF_3-implanted samples.

Both Fig. 7.1(a) and Fig. 7.1(c) show that self-annealing is evident in our samples at a fluence of 10^{16} cm^{-2}. Comparing Fig. 7.1(a) to the set of curves of Fig. 3.3 yields a closest match to a spectrum intermediate between those of Figs. 3.3(b) and 3.3(c), indicating that this has reduced the degree of amorphicity to a level roughly equivalent to that produced by a Si^+ fluence of 10^{13} cm^{-2}. Similarly, for the SiF_3^+ implant of Fig. 7.1(c), the comparison to Fig. 3.3 suggests a rough correspondence to a damage level equivalent to that

produced by a Si^+ fluence of 10^{14} cm^{-2}.

The previous paragraph, as well as a direct comparison of the two upper curves of Fig. 7.1, show that for the same fluence and ion energy, bombardment with SiF_3^+ produces more structural disorder than does Si^+. This is consistent with the higher ion fluence ($\approx$ 4X) and with the greater mass of SiF_3^+. Since SiF_3^+ is heavier that Si^+ (by about a factor of three), the momentum carried by these ions is greater than that carried by equi-energetic Si^+ ions (by about a factor of $\sqrt{3}$).

The lower curves of Fig. 7.1, with the LO dominant and the amorphous bands absent, show that the annealed samples are indeed crystalline and that the damage layer has "healed." However, there is a very interesting difference between these crystal spectra and the original pre-implant spectrum of Fig. 3.3(a): The amplitude of the "forbidden" TO line has increased substantially. This increase is larger for the SiF_3-implanted material, which is recovering from greater damage than is the Si-implanted material, and which has higher silicon concentration near the surface.

The increase in TO phonon scattering intensity, relative to the LO line, may be interpreted in one of two ways: A possible explanation is that the recrystallization during the anneal has resulted in non-epitaxial regrowth.

The surface layer no longer has (100) orientation, so that the TO line is no longer forbidden. The TO to LO intensity ratio would therefore be a direct indication of the quality of the single crystal. The results in Fig. 7.1 would therefore indicate that the post-anneal GaAs is crystalline (LO and TO phonon line widths are the same as in the single crystal), but the initial crystal orientation is affected by the implant + anneal cycle.

Another plausible explanation lies in the fact that the annealed GaAs is n type. For a doped semiconductor equilibrium of the chemical potential causes carriers to migrate into the material, resulting in a depletion layer [Kittel]. In the depletion layer, the GaAs behaves like the undoped crystal. However, in the space-charge region a pure LO phonon no longer exists. Because of the macroscopic elsectric field associated with the LO mode, it interferes with the free carriers, resulting in two coupled LO phonon-plasmon modes [Mooradian & Wright, Klein]. The coupled modes have frequencies dependent on the charge density. One mode has a frequency between zero (small charge density) and the TO phonon frequency (high density). The second has a low carrier density limit of the LO phonon frequency, and is bounded above due to dopant-ion concentration limits.

Thus, the free-carrier volume does not contribute

to the LO line intensity: it contributes a coupled mode. The TO mode has no macroscopic electric field and does not couple to the charges: the volume containing the plasma still has a pure TO phonon. The TO phonon then has the same intensity as in the undoped crystal, and the LO line intensity is reduced. The ratio of the two intensities is then a measure of the thickness of the depletion layer, and consequently of the dopant concentration [Shen & Pollak].

The Si^+ implant would be expected to have a lower dopant concentration than the SiF_3^+, resulting in a deeper depletion layer and thereby a smaller TO/LO intensity ratio. This is supported by the data in Fig. 7.1. However, the silicon-on-gallium substitutional density is lower for the SiF_3^+ implant, as can be seen in Fig. 7.2. Also, no coupled mode is seen in either of these spectra, very strong evidence, contradictory to the plasmon-phonon analysis.

The solution of this problem may be a combination of the two causes (or something different). However, it is not a simple problem, and incorporates the difficulty of a spatially varying dopant concentration.

7.3 SILICON LOCAL MODES IN IMPLANTED GaAs: THE INFLUENCE OF FLUENCE AND ANNEALING

Figure 7.2 shows detailed scans of the weak

structures seen near 400 cm^{-1} in Fig. 7.1. Three peaks are observed: at 396, 391, and 381 cm^{-1}. All three are seen after annealing; prior to annealing, only the 396 and 381 cm^{-1} lines are discernible. These spectra are considerably better defined than those seen in recent work by Nakamura and Katoda, and our results provide the first Raman observation of the 381 cm^{-1} line in Si-implanted GaAs. This line is quite important because, unlike the others (as discussed below), it is a Raman signature of Si substituting for Ga in GaAs, i.e., a donor site.

Infrared studies of the vibrational local modes introduced by ^{28}Si in GaAs have recently been carefully analyzed by Theis and Spitzer. Their analysis suggests that our lines at 396, 391, and 381 cm^{-1} correspond to localized vibrations of Si_{As}, Si_{Ga}-Si_{As}, and Si_{Ga} defects, respectively (our room temperature peak positions are ~ 2.5 cm^{-1} lower in $\bar{\nu}$ than their 80-K frequencies). Si_{Ga} denotes a silicon atom at a gallium site, Si_{As} denotes a silicon atom at an arsenic site, and Si_{Ga}-Si_{As} denotes a nearest-neighbor <u>pair</u> of substitutional silicons.

Since annealing results in electrical activation of the implanted region, i.e, its conversion into a low-resistivity n-type region, it might be expected that any spectral signature associated with the Si_{Ga} donor would increase after annealing. Thus the fact that the 391 cm^{-1}

line is observed after, but not before, annealing would appear to associate this line with Si_{Gs}, rather than with the Si_{Gs}-Si_{As} pair assignment of Theis and Spitzer.

To resolve the apparent contradiction suggested above, and also to test the fluence dependence of these lines, scans were taken for implanted-and-annealed samples for $^{28}Si^{+}$ fluences F between 10^{16} and 10^{14} cm^{-2}. Results are shown in Fig. 7.3. The intensity of the 396 cm^{-1} line, which could be followed throughout this range of fluence,F, exhibits a systematic sublinear increase with increasing fluence which is approximated well by $I(396) \sim F^{0.7}$, as shown in Fig. 7.4. The weak 381 cm^{-1} line, observable above noise only at high F, appears to behave similarly. However, the behavior of the 391 cm^{-1} line is quite different; its intensity increases <u>much more rapidly</u> with fluence. The superlinear increase corresponds roughly to $I(391) \sim F^{1.3}$. This means that the relationship between the intensities of the lines at 391 and 396 cm^{-1} is, within experimental error, consistent with $I(391) \sim [I(396)]^2$. Precisely such a relation is expected if I(391) is produced by a defect composed of a <u>pair</u> of impurity atoms. Thus our results <u>support</u> the Theis-Spitzer identification of the 391 cm^{-1} line as a local mode of Si_{Gs}-Si_{As}. The explanation of the "appearance" of the 391 cm^{-1} line in the post-annealing spectra of Fig. 7.2 lies

elsewhere. Annealing causes all of the local-mode lines to sharpen significantly. This sharpening exposes the 391 cm^{-1} line by uncovering it from the low-frequency wing of the stronger line at 396 cm^{-1}. Before annealing, the weaker line is not resolvable.

Throughout this study, we observed no marked differences between the two annealing methods used, SFA and RTA. One illustration of this is the close similarity between the lower-left curve of Fig. 3 (observed for an RTA-annealed sample) and the top curve of Fig. 4 (observed for the corresponding SFA-annealed sample).

Electrical sheet-resistance measurements (carried out at ITT) showed a clear division of the samples into two electrically-disparate groups. All of the implanted-and-annealed samples (such as those whose Raman spectra are shown in Fig. 7.3 or the lower half of Fig. 7.2) are n-type and have sheet resistances in the range of 50 to 250 ohms per square. All of the unannealed implanted samples (such as those whose spectra are shown in Fig. 3.3 or the upper half of Fig. 7.2) have much higher resistance, at least as great as 2×10^4 ohms per square, our measurement limit. Thus the dichotomy in electrical behavior, which corresponds to the execution (or omission) of the SFA or RTA annealing step, is quite evident.

The two benefits of annealing, electrical

activation and structural healing, are widely regarded as two separate phenomena. Our experiments strongly suggest that this is not the case. Figure 7.2 reveals no annealing-induced increase in the intensity of the Si_{Ga} donor line at 381 cm^{-1}. It therefore appears that the donors are already present in the implanted material, and that the high pre-annealing resistivity is due only to the amorphicity (and consequent low electron mobility) of the damage layer. Annealing then is not necessarily needed to move and chemically bond Si atoms into Ga sites (they may already be there), but is needed to allow the carriers to move by recovering the high mobility of the crystalline form.

The annealing-induced sharpening of the local-mode lines, evident in a comparison of the upper and lower spectra of Fig. 7.2, can be understood as a narrowing of the distribution of local environments sampled by the four-coordinated silicons. In the amorphous material, there is a spread in nearest-neighbor bond angles in excess of the (dynamic) bond-angle spread of the crystal [Zallen]. This static-disorder contribution to the bond-angle dispersion disappears upon annealing (recrystallization).

The fact that local modes, due to tetrahedral silicon substitution, are observed here prior to annealing

may be a consequence of the self-annealing which was discussed in Ch. 3. This hypothesis requires further investigation, as discussed in Chapter 9.

Another implant sequence was performed to check this. It was first implanted with SiF_3^+ to a fluence of 10^{16} cm^{-2}. Then it was cooled to room temperature and another SiF_3^+ implant was made on the same wafer, but this time to a fluence of 2×10^{14} cm^{-2}. The first implant results in local modes, as shown in Fig. 7.2. The second implant renders the damage layer amorphous. Following the second implant no silicon local modes were observed. Even though the silicon atoms are tetrahedrally bonded in high concentration (it is unreasonable to suppose that the second implant displaces all or most of the silicon atoms), the local modes are not observed in the a-GaAs layer.

This is strong evidence in support of the viewpoint that local modes are not special in amorphous systems. A local mode exists if the atom vibrates at a frequency at which the lattice can not vibrate, (e.g. $\bar{\nu} \geq 300$ cm^{-1}) in GaAs. The atom vibrates, but it has no first-order means of communicating with the lattice, localizing the vibration. In amorphous systems no vibration can transmit its energy coherently to neighborhood atoms, i.e. all vibrations consist of a broad distribution of frequencies. Thus, the silicon vibrations are broad (and weak making

them unobservable) just as the GaAs vibrations are broad in the amorphous phase.

FIGURE CAPTIONS

Fig. 7.1 : The effect of annealing on the Raman spectra of Si-implanted and SiF_3-implanted GaAs. Implantation was for an ion fluence of 10^{16} cm^{-2} and an ion energy of 120 keV; annealing was a rapid thermal anneal (950°C, 12 sec). All spectra in this chapter were colected using 5145-A source.

Fig. 7.2 : Detailed scans of the local-mode region of the samples of Fig. 2.

Fig. 7.3 : The effect of fluence on the local-mode Raman spectra of silicon-implanted GaAs. Fluence (of $^{28}Si^{+}$ ions at 120 keV), in units of ions/cm^2, labels each curve. These samples were given a standard furnace anneal (850° C, 20 min). Each curve corresponds to about 25 hours of data accumulation. The peak of the strongest line, at a fluence of 3 x 10^{15} cm^{-2}, is about 20 counts/sec. The sloping background in these spectra (as well as in the spectra of Fig. 3) is real; it is part of the two-phonon continuum of the host solid.

Fig. 7.4 : Log-log plot of the respective silicon local-mode intensities for Si^+-implanted GaAs. Over this short range, the single-substitutional sites are increasing sublinearly with fluence, while the pair mode is super-linear with a slope approximately twice that of the Si_{As} mode.

Fig. 7.5 : Log-log plot for silicon local-mode intensites in the SiF_3^+-implanted GaAs. Below the 3×10^{15} cm^{-2} fluence, the slopes are roughly the same as the respective curves in Fig. 7.4. Above this fluence, all three curves begin to saturate and all decrease by ~ 30% between fluences 3 and 10 $\times 10^{16}$ cm^{-2}.

Fig. 7.6 : The effect of single, high-fluence implanting on the silicon local modes in GaAs. The low-fluence 2×10^{14} cm^{-2} implant (amorphizes sample) shows no local modes. The high-dose implant shows strong local modes. Another implant to amorphize the sample results in no strong local-mode signature.

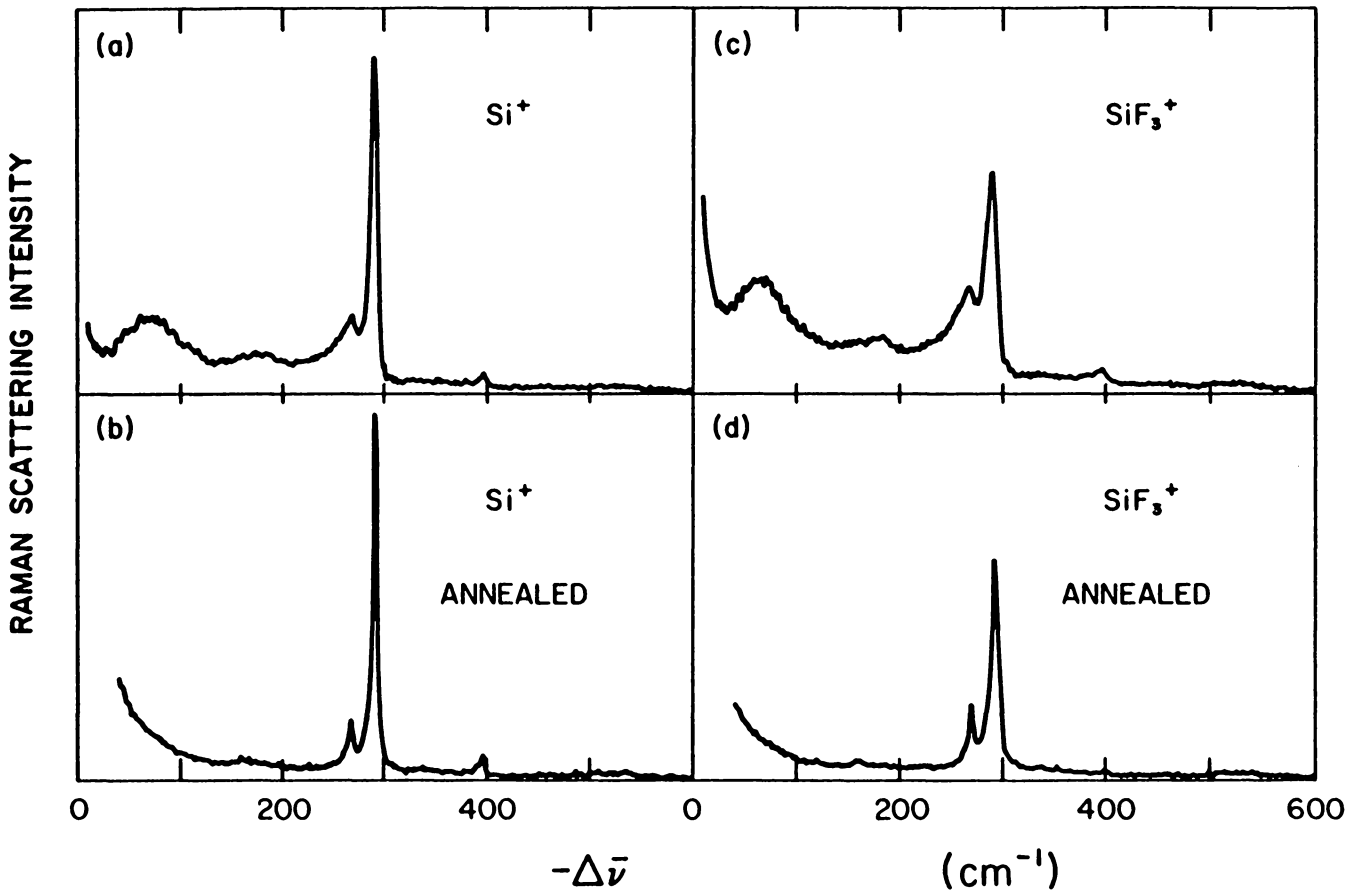

Fig. 7.1 Full Raman spectra before and after annealing.

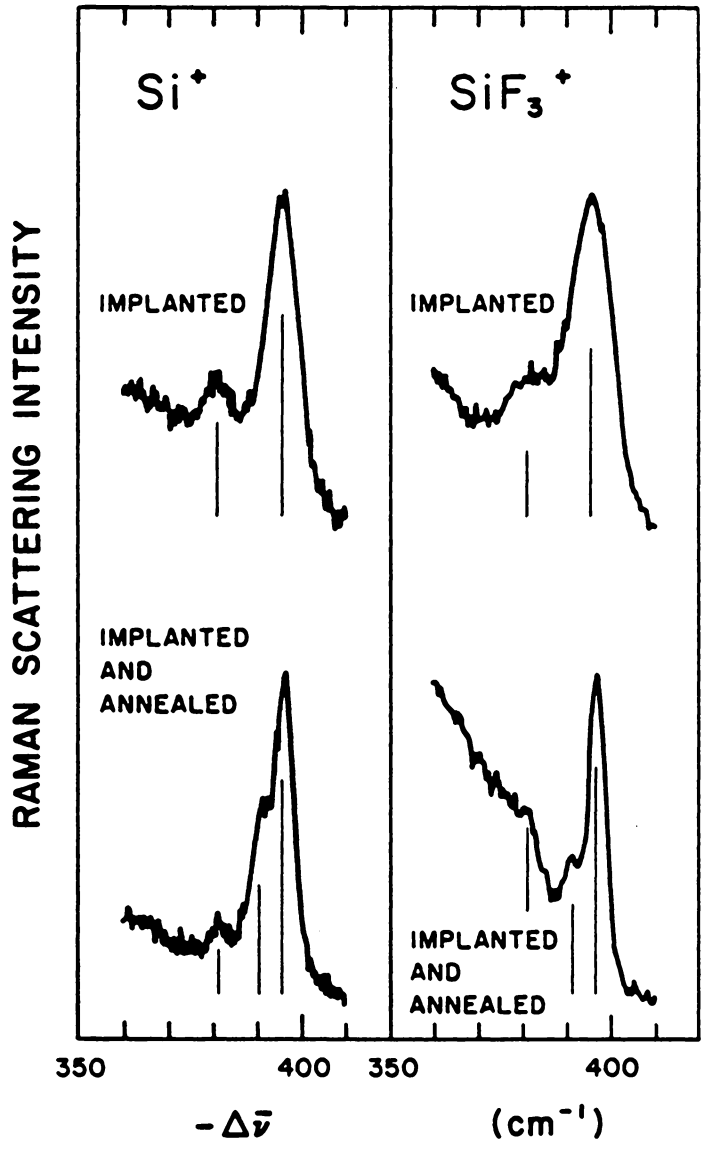

Fig. 7.2 Silicon local modes before and after annealing.

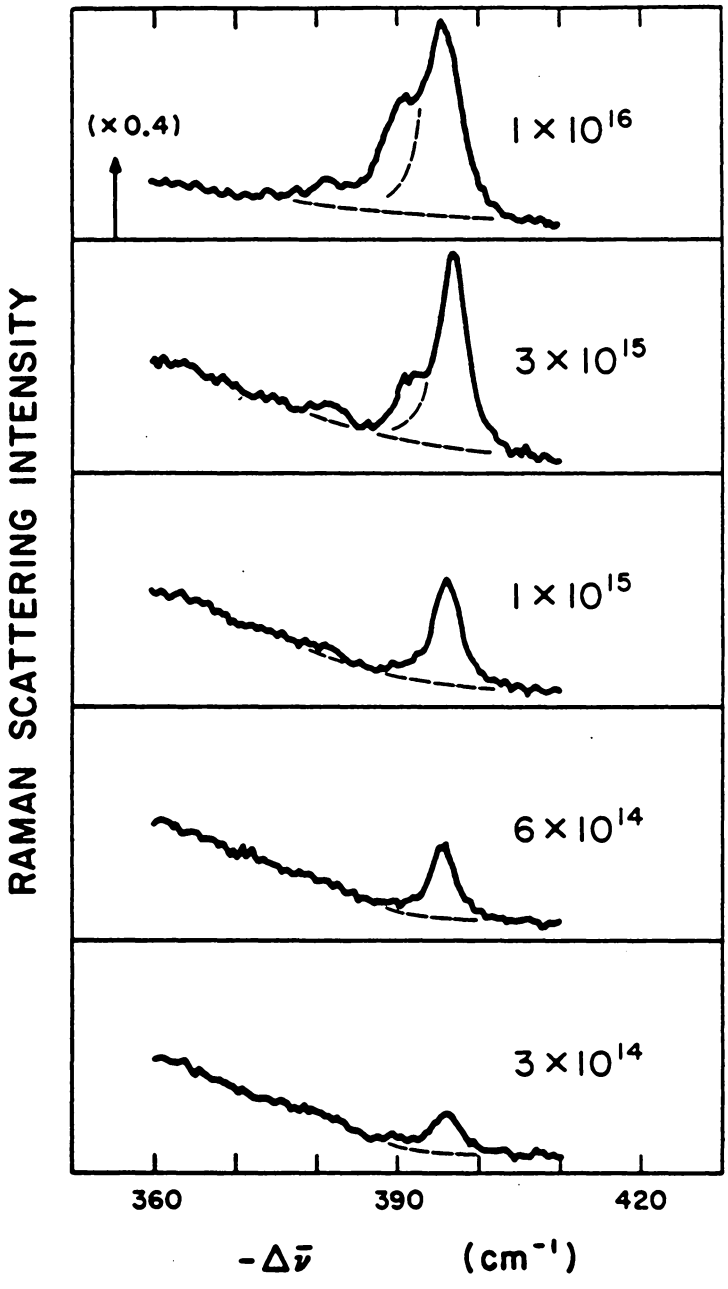

Fig. 7.3 Silicon local modes vs. Si fluence.

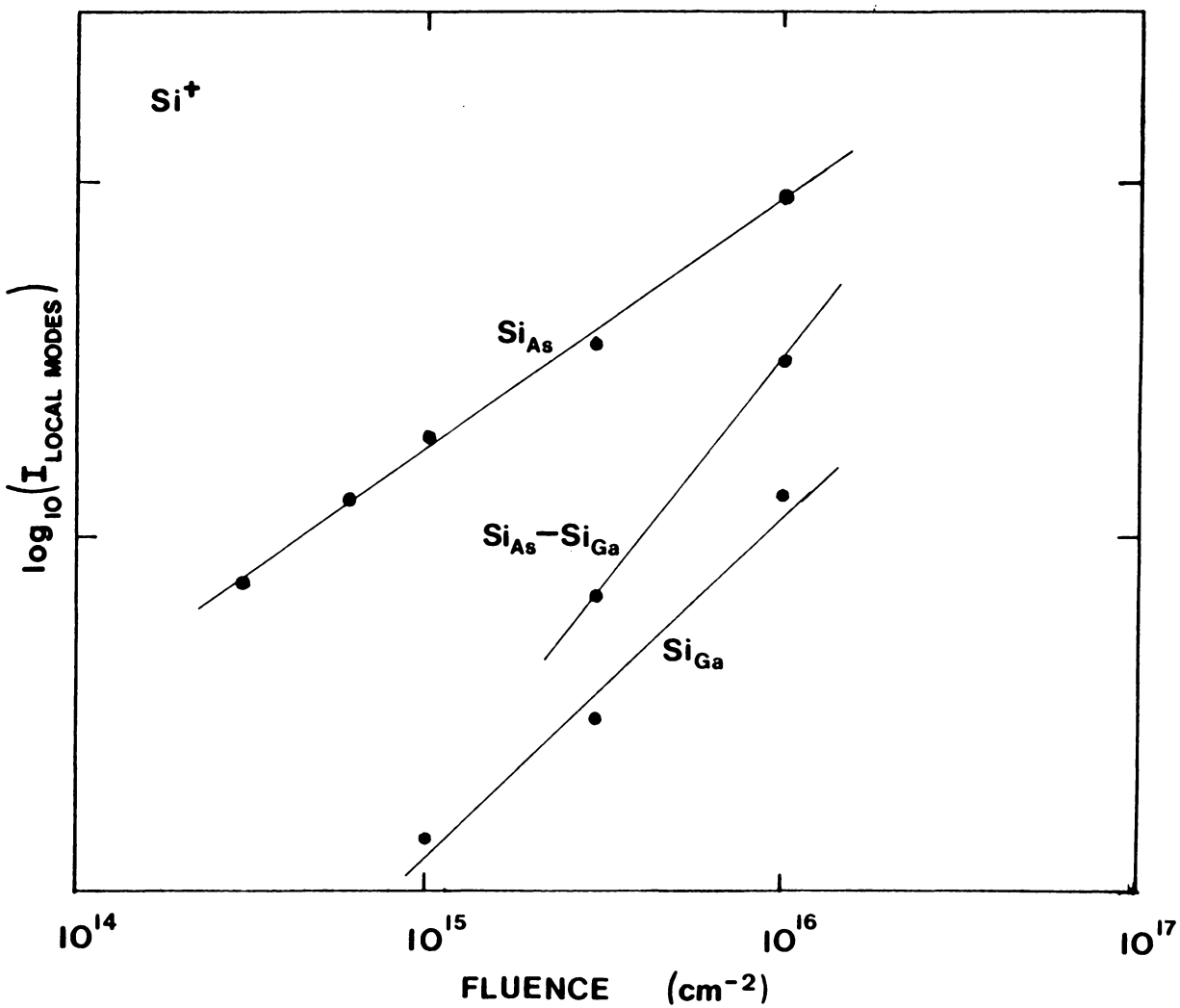

Fig. 7.4 Silicon local mode intensities vs. Si^+ fluence.

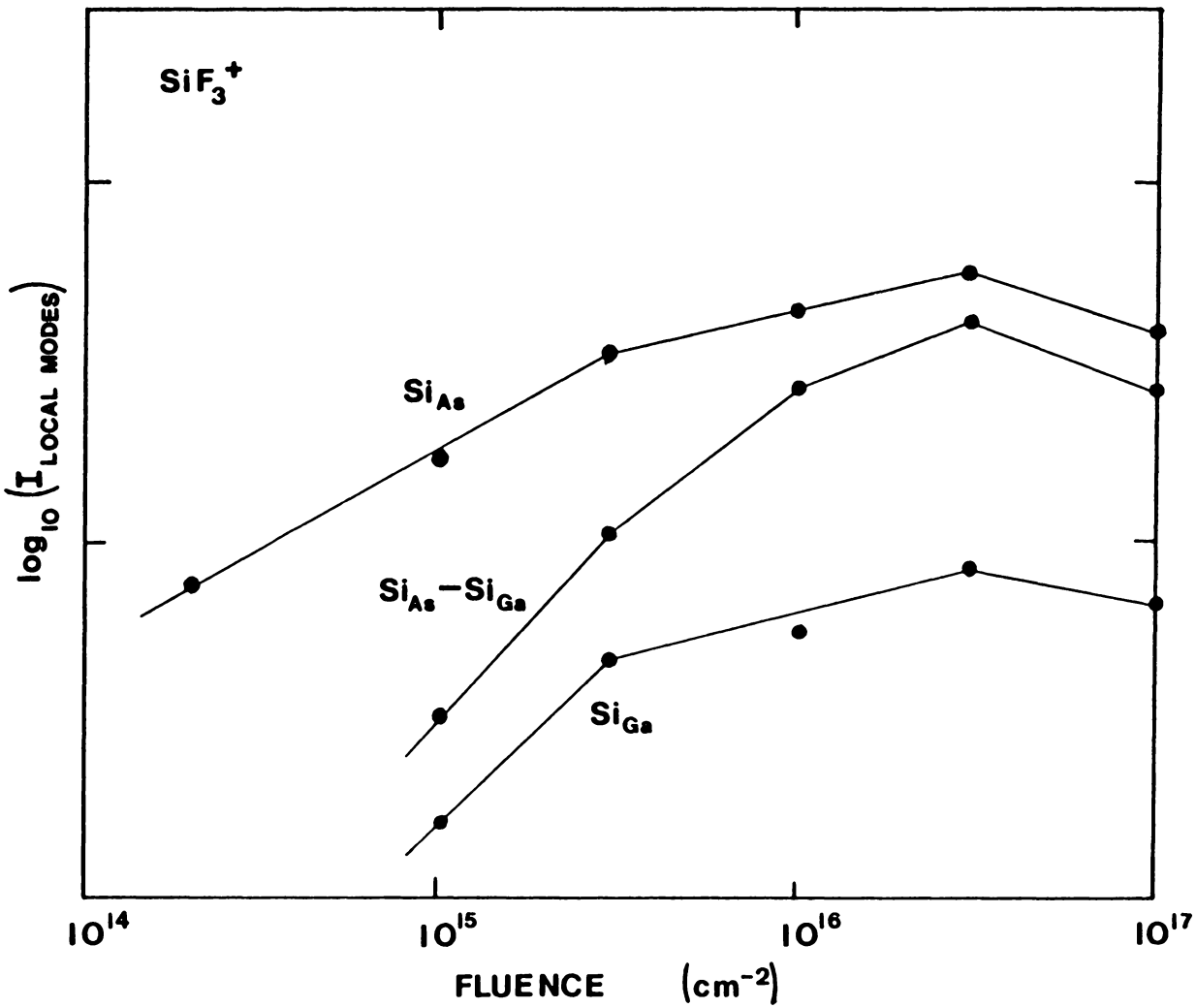

Fig. 7.5 Silicon local mode intensities vs. SiF_3^+ fluence.

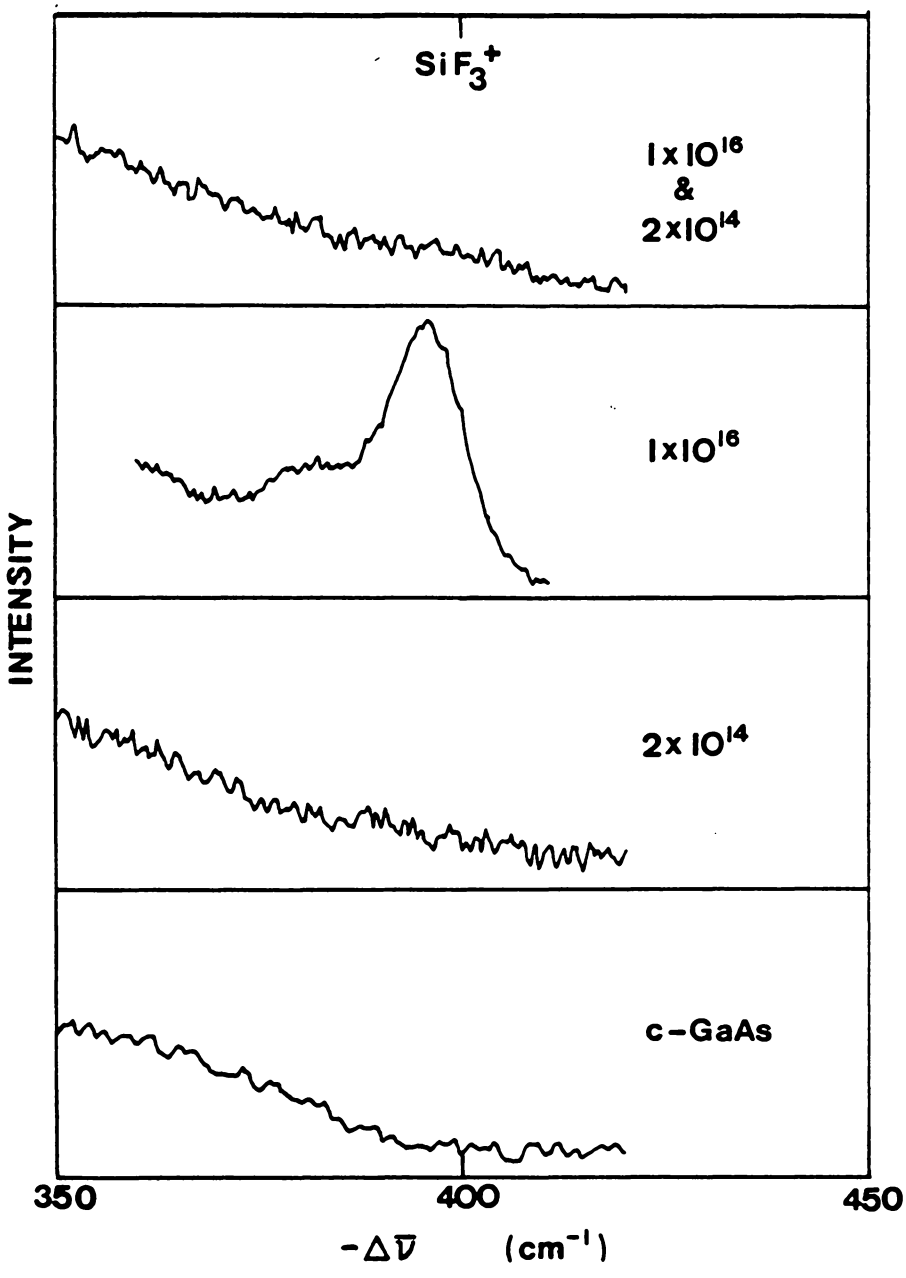

Fig. 7.6 Local modes, no post-implant anneal.

CHAPTER 8: SUMMARY

Extensive Raman-scattering experiments have been performed in order to investigate the nature of GaAs after it has been implanted with various ions. The spectroscopic evidence (Chapter 3) indicates that the near-surface damage layer is composed of microcrystallites of GaAs mixed with regions of amorphous GaAs, created by the incident ions as they collide with the substrate atoms.

A fully amorphous surface layer has been produced by implanting GaAs with heavy SiF_3^+ ions at 120-keV (Fig. 3.6). Comparisons between this a-GaAs ion-implanted surface layer and two a-GaAs films prepared by conventional techniques (Fig. 3.8) show these three means result in identical materials, based upon the characteristics of the Raman spectrum and its polarization properties.

A quantitative depth profile of the structural changes caused by high-fluence 45-keV beryllium implants into GaAs has been obtained in Chapter 4 using Raman scattering in combination with chemical etch. The experimental observations are well accounted for by a structural model consisting of a fine-scale amorphous/ microcrystal mix. Our results for the depth dependence of the amorphous volume fraction and the characteristic crystallite size have been presented in Fig. 4.7. Both

measures present the same depth profile: A high-damage plateau region, in which these measures change little with depth, is followed by a transition region in which they vary smoothly until the bulk-crystal values are reached. There is no sign of a near-surface decrease in disorder, an experimental result which appears to disagree with LSS and TRIM theoretical predictions. Increasing the ion fluence, at constant ion energy, increases the amplitude of the damage (e.g. at 5×10^{14} cm^{-2}, the highest ion fluence studied, the amorphous fraction in the plateau region is 0.25 and the crystallite size is about 60 A) but does not appreciably change the shape of the depth profile (Figs. 4.4, 4.5, and 4.6). An amorphization track diameter of about 4 A is estimated for 45-keV Be^{+} ions incident upon GaAs.

The LO Raman line of the crystalline fraction was studied as a function of excitation photon energy from 1.55 to 2.71 eV. The LO intensity rises rapidly at low photon energies because of the increasing optical penetration depth. We also find, as seen in Fig. 4.9, that there is a real increase in the Raman-scattering efficiency above 2.5 eV, an effect we attribute to resonance with the E_1 interband transition at 2.9 eV. This resonance-Raman effect is quenched by implantation, most probably because of the broadening of the E_1 crystal peak as the crystallite size

decreases with increasing ion bombardment.

In Chapter 5 a non-destructive damage depth profile was obtained by varying the penetration depth of the probe into the implanted GaAs which was fully amorphous near the surface. This was accomplished by varying the excitation photon energy from 2.71 to 1.55 eV (Fig. 5.1). When the optical penetration depth of the light is small, in comparison to the thickness of the a-GaAs surface layer, the Raman spectrum is identical to the spectrum of the a-GaAs films. However, as the penetration depth is increased, LO phonon scattering is observed to come from the less-damaged GaAs beneath the a-GaAs top layer. Using a simple two-layer model, the thickness of the amorphous layer is estimated to be approximately 500 A.

For implanted GaAs which has not been fully amorphized, it was found in Chapter 5 that the Raman LO line characteristics (Figs. 5.3, 5.4) can be used to non-destructively evaluate the uniformity of the damage layer probed. This is done by varying the optical penetration depth (excitation photon energy). It was found that near-surface damage plateau layers are common to these implanted samples: 45-keV Be^+ and 180-keV Be^+ (in both cases via chemical etch and penetration depth), 180-keV Si^+ and 120-keV SiF_3^+ (both by penetration-depth effects).

We have observed a strong, resonant feature (A) in the Raman spectrum of ion-implanted GaAs (see Figs. 6.1-6.3), prior to any anneal. It is observed over a wide range of implant conditions (species, energies, and fluences), but it is not observed in either the crystalline or amorphous phases. The feature is strong for excitation photon energies below 2.2 eV; above 2.2 eV it is weak and is masked by the a-GaAs component of the spectrum. The frequency and line shape vary little for the circumstances studied.

Careful intensity measurements of the a-GaAs component of the Raman spectrum, I_a, relative to CaF_2, indicate that it depends solely upon optical penetration depth (Fig. 6.4). I_a then provides us with an internal standard for optical penetration over the full photon energy range studied (1.55 to 2.71 eV). Thus, scattering volume effects and scattering efficiencies may be separated.

Based upon this, the LO line of the micro-crystalline remnant resonates with the approaching E_1 interband electronic transition at ~ 3 eV, and not with the E_0, $E_0 + \Delta_0$ critical points in the density of states (Fig. 6.5). The resonance is similar to reported allowed-TO measurements on c-GaAs [Grimsditch et al.], as expected for features arising from the crystalline component of the

implanted material.

A resonates somewhere between E_0 and $E_0 + \Delta_0$, but <u>not</u> near E_1 (Fig. 6.6). A is seen strongly for $\hbar\omega_L \lesssim 2.2$ eV. For the highest valence and lowest conduction bands of GaAs this corresponds to $k \lesssim 0.2\ k_{BZ}$ ($\lambda \gtrsim 10\ a_0$). This implies that only electrons with sufficiently large wavelengths, on the scale of the microcrystallite dimensions, are affected by the disorder, and may thereby participate in the scattering process responsible for A. Hence the large-$\mathbf{k}$ electrons primarily responsible for photon absorption near the E_1 transition are not affected strongly by the microcrystallinity, and for this reason do not have a strong scattering cross-section.

We propose that defect-induced Raman scattering by acoustic modes of c-GaAs is responsible for the new feature. The defects are taken to be simply the interface regions between the GaAs crystallites and the amorphous GaAs, in agreement with the observation that $I_A/I_{LO} \sim \mathcal{L}^{-1}$. The extended defects scatter the electron (hole) elastically, resulting in a momentum transfer which breaks the $\mathbf{k} = 0$ selection rule of the infinite crystal. The scattering cross-section is large when the electronic wavefunction and the acoustic phonon have similar wavelengths. A model developed to account for this type of process in the presence of point defects is adapted for

the present case, with moderate success.

Experiments were carried out on a variety of implanted and implanted-and-annealed GaAs samples, using both Si^+ and SiF_3^+ as the implant species, in order to probe the influence of processing on the atomic-scale structure of the implanted region. For given fluence and ion energy, SiF_3^+ ions are more effective than Si^+ ions in damaging the lattice; otherwise, the effects observed with the two types of ions are qualitatively quite similar. The progressive amorphization, with increasing fluence, of a 1000-A-deep portion of the damage layer, was cleanly observed (Fig. 3.3) via the evolution of the broad three-band continuum characteristic of amorphous GaAs. The continuum was measured from its high-frequency cutoff near 300 cm^{-1} down to about 15 cm^{-1}. The crystalline remnant at high fluence is microcrystalline, as revealed by the broadening and downshifting of the crystal LO line. Annealing fully recovers the crystalline form, but the (100) orientation may <u>not</u> fully recover, as revealed (Fig. 7.1) by the appreciable increase of the TO line. This calls into question the widely-made assumption of epitaxial re-growth.

Three lines observed near 400 cm^{-1} in heavily-implanted samples (Fig. 7.2) were identified with silicon local modes by comparison with recent infrared work

and by measurements of their fluence dependence (Fig. 7.3, 7.4). In particular, our fluence-dependence results support a previous assignment of the 391 cm^{-1} line to a defect made up of a neighboring pair of silicon impurities. We also report the first Raman-scattering observation of a line associated with the Si_{Ga} donor site (381 cm^{-1}). The effect of annealing on the silicon-local-mode lines, displayed in Fig. 7.2, is not found to be an intensity increase, but instead is seen to be a pronounced line narrowing which we interpret as reflecting an annealing-induced sharpening of the distribution of local environments encountered by the substitutional silicons. In particular, the Si_{Ga} donor-site line is clearly seen before annealing, even though annealing is necessary to transform the highly-resistive implanted material into semiconducting n-type GaAs. These results strongly suggest that the primary role of annealing in the "electrical activation" of implanted semiconductors is not to shift the impurity atoms into substitutional donor or acceptor sites (they may already occupy such sites), but is instead to recover the high carrier mobility of the crystalline form. In the low-mobility amorphous material which forms the host solid after implantation and before annealing, the carriers are present, but immobile. "Healing" and "activation" thus correspond to the same

structural process: the elimination of amorphicity.

CHAPTER 9: SUGGESTIONS FOR FUTURE RESEARCH

The results of this dissertation are hardly final, and in fact only scratch the "surface" of the scientifically interesting properties of these ion-implanted semiconductors. In this chapter I shall mention several directions of study, in which the present work naturally leads.

The silicon local mode studies leave many questions unanswered. It would be interesting to see if local modes are present in the implants of Chapter 7 due to self annealing, or independent of a substantial temperature rise above 300 K. This work has been started in Chapter 7 (Fig. 7.6), in which it is found that the local modes are quenched by an amorphizing implant. Is this because the atoms are no longer tetrahedrally bonded or because local modes do not exist in amorphous semiconductors (even above the fundamental vibrational regime)?

It would be relevant to find out if many below-threshhold implants, sufficient to reach a total ion fluence of 1×10^{16} cm^{-2}, result in local modes like those observed in the single implant of the same fluence (which showed substantial self annealing, as evident in the LO line characteristics). The SiF_3^+ implants are convenient for this purpose. It would also be interesting to compare

these results (and Fig. 7.6) with a 10^{16} cm^{-2} implant which has been annealed and then implanted with the amorphizing dose. All of these must be compared to the c-GaAs spectrum in Fig. 7.6 and the complementary spectrum for a-GaAs (350-420 cm^{-1}, low power, wide slits, very clean).

It may be necessary to examine these local mode problems at low temperature for the results to be definitive. For the silicon local modes observed in the 10^{16}-cm^{-2} implanted GaAs, for which there was self-annealing, it would be interesting to see if the higher frequency band resolves into two bands (corresponding to Si_{As} and Si_{As}—Si_{Ga} dimer local modes) at 80 K. It would be prudent to first attempt the same feat with the annealed samples, for which it is known that there are two distinct modes.

Some early low-temperature work has been performed on the Be^{+}-implanted GaAs. In Fig. 9.1 the LO peak frequency is shown, between 15 and 300 K, for the c-GaAs and GaAs implanted to fluences of 1 and 5 x 10^{14} cm^{-2}. The straight line (slope = -1.35×10^{-2} cm^{-1}/K) is from Sapriel et al.. Agreement with their results is good. The ion implanted result is new. It is not clear whether or not the slope is increasing (that is, approaching zero) with fluence. Increased damage, and supplemental, careful

measurements are needed to clarify this. The origin of such a shifting slope would be interesting.

The fundamental nature of the new mode in the first-order Raman spectrum of these ion-implanted GaAs systems (Chapter 6) is extremely interesting. The Raman tensor for this mode needs to be completed by considering implanted crystals with (110) and (111) orientation (cleavage planes).

The use of a dye laser would be an excellent addition in order to pinpoint the resonance peak and to look below 1.55 eV (beware of rapidly increasing d_{OPT}). The microcrystalline LO phonon resonance with E_1 should be observed to higher energies. More could then be said about the resonance quenching with decreasing crystallite size. The identification of uniform specimens is extremely relevant to this work, as well as for other spectroscopic studies in the visible range of the light spectrum. I view this as the principal limitation on these systems, and a primary result of my work.

An interesting alternative to the dye laser would be to sit at one $\hbar\omega_L$ and vary the sample temperature (above and below room temperature) to observe the resonance as the energies of the direct transitions vary. This would be interesting for both the LO line and the new feature at 47 cm^{-1} (not with the same laser line, of course). Keeping

track of the frequency, linewidth, and the intensity of the a-GaAs spectral component would be essential. Complementary to this are high-pressure effects.

Of course, the anneal kinetics of the new mode (and the whole spectrum) are important. It is possible that very much could be said about the recrystallization process. Since low-temperature anneals (~ 200°C) are sufficient to recrystallize these implanted systems, this would be a good starting point. At these low temperatures no "cap" is necessary and a simple argon atmosphere is sufficient.

Observing the nature of the 47 cm^{-1} mode as the ion-implanted GaAs is rendered amorphous is very interesting. Self-annealing must be avoided, for this purpose, by using the multiple-implant technique developed here. Since the 45-keV Be^{+} implanted GaAs has been studied extensively in this work, it is the best choice for such a study. Five implants, each to a fluence of 5×10^{14} cm^{-2}, is a good starting point. In view of the scientific significance of a new discovery, this is not an unreasonable request.

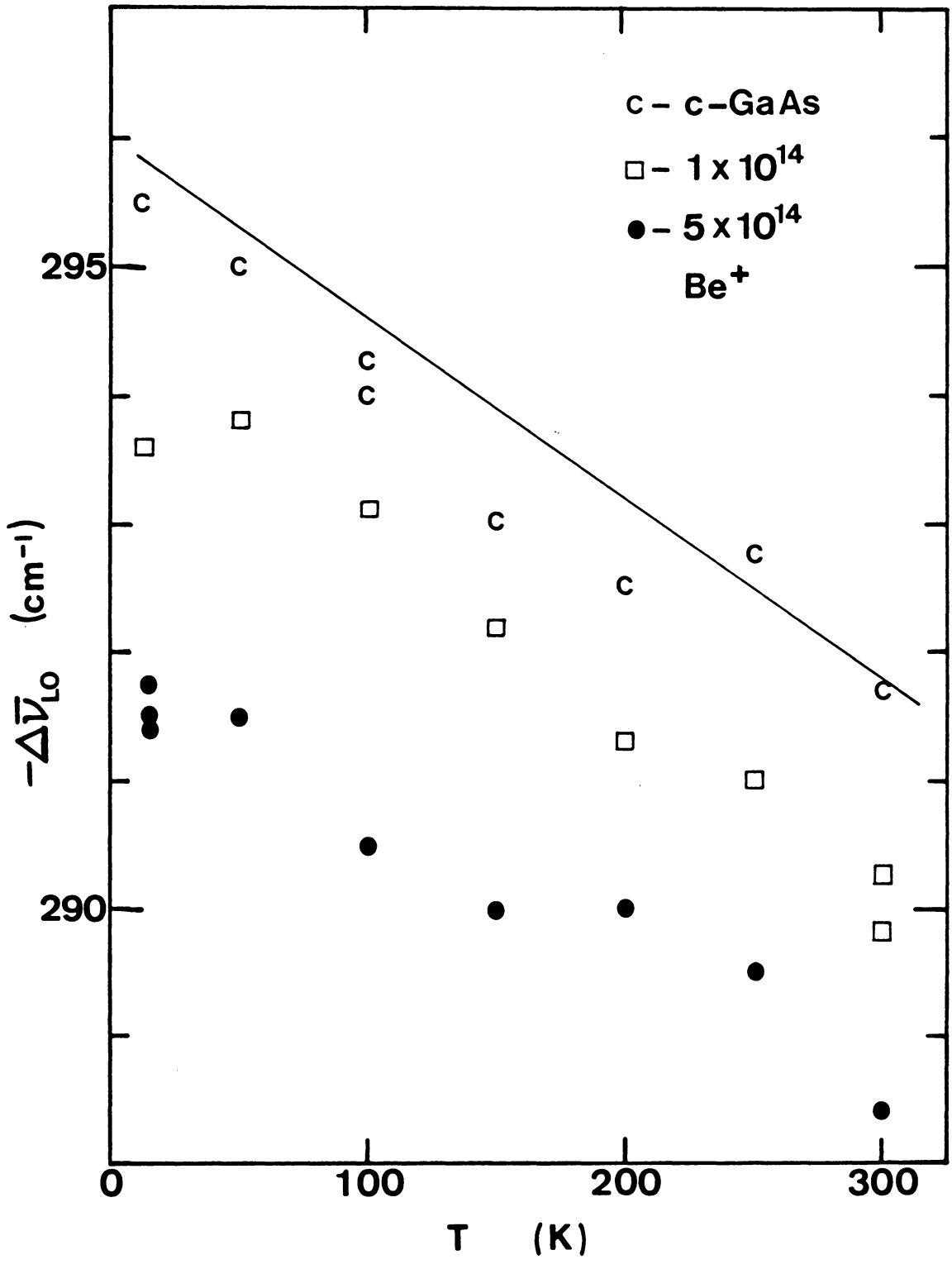

Fig. 9.1 Temperature variation of LO phonon frequencies.

LITERATURE CITED

L.L.Abels, S.Sundaram, R.L.Schmidt, and J.Comas, Appl. Surf. Science 9, 2 (1981).

D.E.Aspnes, S.M.Kelso, C.G.Olson, and D.W.Lynch, Phys. Rev. Lett. 48, 1863 (1982).

D.E.Aspnes and A.A.Studna, Phys. Rev. B 27, 985 (1983).

D.E.Aspnes, Characterization of Materials and Interfaces by Visible/Near UV Optical Spectroscopy, Materials Research Society, Symposium X (Boston, 1984), J.Mater.

M.Balkanski, J.F.Morhange, G.Kanellis, J. Raman Spect. 10, 240 (1981).

A.S.Barker and A.J.Sievers, Rev. Modern Phys. 47, S1(1975).

R.S.Berg, P.Y.Yu, E.R.Weber, Appl.Phys.Lett. 47, 515(1985).

R.S.Berg and P.Y.Yu, Phys. Rev. B 33, 7349(1986).

R.S.Berg and P.Y.Yu, Phys. Rev. B 35,2205 (1987).

R.S.Bhattacharya, A.K.Rai, Y.K.Yeo, P.P.Pronko, S.C.Ling, S.R.Wilson, and Y.S,Park, J.Appl.Phys. 54, 2329 (1983)

J.S.Blakemore, J. Appl. Phys. 53, R123 (1982).

C.E.Bouldin, R.A.Formin, M.I.Bell, Phys. Rev. B 35, 1429

(1987).

M.Cardona in Light Scattering in Solids, Vol.II, M.Cardona and G.Güntherodt, Eds. (Springer-Verlag, Berlin, 1982).

G.Carter and W.A.Grant, Ion Implantation of Semiconductors, (Edward Arnold, London, 1976).

L.A.Christel and J.F.Gibbons, J.Appl.Phys. 52, 5050 (1981).

M.L.Cohen and J.R.Chelikowsky, Handbook on Semiconductors, W.Paul, Ed. (Norht-Holland, Amsterdam, 1982).

Cotton, Chemical Applications of Group Theory (Wiley, New York, 1971).

A.C.deWilton, M.Simard-Normandin, P.T.T.Wong, J. Electrochem Sci. and Tech. 133, 988 (1986).

B.Dorner and D.Strauch, private communication.

W.M.Duncan and G.Westphal in VLSI Electronics: Microstructure Science, N.G.Einspruch and W.R.Wisseman, eds. (Academic Press, New York, 1985).

M.Erman, J.B.Theeten, P.Chambon, S.M.Kelso, and D.E.Aspnes J. Appl. Phys. 56, 2664 (1984).

H.Fröhlich in Polarons and Excitons, C.G.Kuper and G.D.Whitfield, eds.(Oliver and Boyd, Edinburgh, 1963).

A.Geissberger, R.Sadler, M.Holtz, and R.Zallen in Semi-Insulating III-IV Materials, H.Kukimoto and S.Miyazawa, Eds. (Norht-Holland, Amsterdam, 1986).

J.F.Gibbons, Proc. IEEE 55, 295 (1968).

J.F.Gibbons, Proc. IEEE 60, 1062 (1972).

J.F.Gibbons, W.S.Johnson, A.W.Mylroie, Projected Range Statistics (Dowden-Hutchinson-Ross, Exeter, 1985).

A.A.Gogolin and E.I.Rashba, Sol. State Comm. 19, 1177 (1976).

S.Gopalan, P.Lautenschlager, and M.Cardona, Phys. Rev. B 35, 5577 (1987).

M.H.Grimsditch, D.Olego, and M.Cardona, Phys. Rev. B 20, 1758 (1979).

W.Hayes and R.Loudon, Scattering of Light by Crystals, (Wiley, New York, 1978).

K.Huang, Proc. Roy. Soc. (London) A208, 352 (1951).

J.D.Jackson, Classical Electrodynamics, 2nd ed. (Wiley, New York, 1975).

F.A.Jenkins and H.E.White, Fundamentals of Optics, (McGraw-Hill, New York, 1976).

B.Jusserand and J.Sapriel, Phys. Rev. B 24, 7194 (1981).

H.Kawamura, R.Tsu, and L.Esaki, Phys. Rev. Lett. 29, 1397 (1972).

Q.Kim and Y.S.Park, J. Appl. Phys. 51, 2024 (1980).

C.Kittel, Introduction to Solid State Physics, 5th ed. (Wiley, New York, 1976).

M.V.Klein in Light Scattering in Solids II, 2nd ed., M.Cardona, ed. (Springer-Verlag, New York, 1983).

Sook-Il Kwun, M.H.Lee, L.L.Liou, W.G.Spitzer, H.L.Dunlap. and K.Vaidyanathan, J. Appl. Phys. 57, 1022 (1985).

R.Loudon, Adv. in Physics 13, 423 (1964).

G.Mahan, Many Particle Physics, (Plenum, New York, 1981) p.38.

W.McLevige, Ph.D. Dissertation, University of Illinois (1978), p. 17.

J.Menéndez and M.Cardona, Phys. Rev. B 31, 3696 (1985).

A.Mooradian, G.B.Wright, Phys. Rev. Lett. 16, 999 (1966).

T.Nakamura and T.Katoda, J. Appl. Phys. 53, 5870 (1982).

J.F.Nye, Physical Properties of Crystals, (Clarendon, Oxford, 1957).

W.G.Opyd, J.F.Gibbons, J.C.Bravman, M.A.Parker, Appl. Phys. Lett. 49, 974 (1986).

R.H.Parmenter, Phys. Rev. 100, 573 (1955).

R.K.Pathria, Statistical Mechanics (Pergamon, Oxford, 1972), p.487.

A.Pinczuk and E.Burstein in Light Scattering in Solids I, 2nd ed., M.Cardona,Ed. (Springer-Verlag, Berlin, 1982).

F.H. Pollak, SRI Report on Microelectronics Materials (1985, unpublished).

H.Richter, Z.P.Wang, and L.Ley, Sol. State Comm. 39, 625 (1981).

H.Ryssel and I.Ruge, Ion Implantation (Wiley, Chichester, 1986), p. 193.

P.Santos, M.Hundhausen, L.Ley, Phys. Rev. B 33, 1516(1986).

J.Sapriel, J.Chavignon, F.Alexandre, R.Azoulay, Phys. Rev. B 34, 7118 (1986).

L.Schiff, Quantum Mechanics, 2nd ed. (Wiley,New York,1968).

H.Shen, F.H.Pollak, SPIE 524, 145 (1985).

R.Shuker and R.W.Gammon, Phys. Rev. Lett. 25, 222 (1970).

R.S.Singh, S.S.Mitra, Phys. Rev. B 5, 733 (1972).

D.N.Talwar, M.Vandevyver, K.K.Bajaj, W.M.Theis, Phys. Rev. B 33, 8525 (1986).

J.B.Theeten and M.Erman, J. Vac. Sci. Technol. 20, 471 (1982).

W.M.Theis and W.G.Spitzer, J. Appl. Phys. 56, 890 (1984).

M-L. Theye and A. Gheorghiu, Solar Energy Materials 8, 331 (1982).

K.K.Tiong, P.M.Amirtharaj, F.H.Pollak, and D.E.Aspnes, Appl. Phys. Lett. 44, 122 (1984).

S.Tolansky, Multiple-beam Interferometry of Surfaces and Films, (Oxford Univ. Press, London, 1947) p.147.

J.L.T.Waugh and G.Dolling, Phys. Rev. 132, 2410 (1963).

R. Zallen, Phys. Rev. 173, 824 (1968).

R. Zallen, The Physics of Amorphous Solids (Wiley, New York, 1983).

R.Zallen, M.Holtz, R.A.Sadler, A.Geissberger, Bull. Am. Soc. Phys. Soc. 31, 476 (1986).

R.Zeyher, Phys. Rev. B 9, 4439 (1974).

J.F.Ziegler, J.P.Biersack, and U.Littmark, The Stopping and Range of Ions in Solids (Pergamon, London, 1985).

The vita has been removed from the scanned document